

## The relationship between attractive interparticle forces and bulk behaviour in dry and uncharged fine powders

A. CASTELLANOS\*

Dpto. de Electronica y Electromagnetismo, Universidad de Sevilla,  
Avda. Reina Mercedes s/n, 41012 Sevilla, Spain

(Received 2 February 2005; revision received 24 September 2005;  
accepted in revised form 7 October 2005)

*Memento, homo, qui pulvis est et pulverem reverteris.*

*Genesis 3*

*Polvos serán, mas polvo enamorado.*

*Francisco de Quevedo*

The physics of granular materials in ambient gases is governed by interparticle forces, gas–particle interaction, geometry of particle positions and geometry of particle contacts. At low consolidations these are strongly dependent on the external forces, boundary conditions and on the assembling procedure. For dry fine powders of micron and sub-micron particle size interparticle attractive forces are typically much higher than particle weight, and particles tend to aggregate. Because of this, cohesive powders fracture before breaking, flow and avalanche in coherent blocks much larger than the particle size. Similarly the drag force for micron sized particles is large compared to their weight for velocities as low as 1 mm/s. Due to this extreme sensitivity to interstitial gas flow, powders transit directly from plastic dense flows to fluidization without passing through collisional regimes with negligible gas interaction. These two features, strong attractive forces and strong gas interaction make powder behaviour differ qualitatively from the behaviour of large, noncohesive grains. In this paper we investigate the implications of these two features on the bulk powder behaviour. More in particular, the aim of this paper is to examine the relationship between attractive interparticle forces at grain level, with solid bulk properties at low consolidations (solid fraction, stresses), fluidization (aggregation, settling) and flow regime boundaries (plastic flow, inertial flow, fluidization and suspension). Many of the experimental results reported here are for dry and uncharged fine powders made of polymer particles of the order of 10 microns in diameter. However, the basic concepts and methodology are of general applicability.

	PAGE
1. Introduction	265
2. Scope of the paper	267
<b>Part I: Powders at the grain level</b>	<b>270</b>
3. Characterization of single powder particles	270
4. Van der Waals forces between rigid bodies	274

---

\*Email: castella@us.es

4.1. Van der Waals forces between two half-spaces	276
4.1.1. Surface energy	277
4.2. Van der Waals forces between a half-space and a sphere with radius $R$	278
4.3. Van der Waals forces between two rigid spheres	279
4.4. Van der Waals forces between two nonconforming convex bodies: the Derjaguin approximation	279
4.5. The effect of asperities	281
4.6. The effect of retardation	282
4.7. Cohesive–noncohesive particle boundary	282
5. Normal forces between deformable bodies	284
5.1. Elastic contact	285
5.1.1. Nonadhesive elastic contact: Hertz solution	286
5.1.2. Adhesive elastic contact: DMT and JKR solutions	287
5.1.3. Adhesive elastic contact: general solution	288
5.2. Indentation of elastic–ideally plastic materials: elastic–plastic and fully plastic contact	292
5.2.1. Non-adhesive elastic–plastic contact	292
5.2.2. Adhesive elastic–plastic contact	295
5.3. Unloading the adhesive contact of elastic–ideally plastic materials	296
5.3.1. Fully-plastic contact	297
5.4. The effect of asperities	298
6. Normal forces between two powder particles: AFM measurements	299
7. Normal forces: comparison between theory and experiments	305
7.1. Nature of contact	305
7.1.1. Does the contact take place between the base polymer, or through the additives?	306
7.1.2. Is the contact elastic or plastic?	308
7.2. Adhesive contact in the elastic–plastic regime: an approximate model	308
7.3. Results	310
<b>Part II: Powders at the bulk level</b>	<b>312</b>
8. Mechanical properties	312
8.1. Rigid-plastic solid	314
8.2. Elastic–plastic solid	315
8.3. Review of the techniques for measuring powder properties and flowability	318
8.3.1. Empirical techniques	318
8.3.2. Techniques of analysing powder flowability based on fundamental properties	319
8.4. The Sevilla Powder Tester: a new tool to characterize fine cohesive powders at very small consolidations	322
8.5. Experimental results	333
8.5.1. Materials	333
8.5.2. Viscosity effects in interparticle contacts	333
8.5.3. Effect of particle properties and flow additives on the cohesive properties of bulk powder	334
9. Interparticle forces versus bulk stresses: a semiquantitative approach	337
9.1. The structure of fluidized beds of fine cohesive powders	338
9.1.1. Homogeneous fluidized bed: solid-like or fluid-like?	338
9.1.2. Fluid-like domain as a function of particle size and cohesiveness	343
9.2. Aggregation in the fluid-like regime of homogeneously fluidized beds of fine cohesive powders	344

9.2.1. The settling experiments	344
9.2.2. The fluidized bed as a suspension	345
9.2.3. Estimation of average number of particles and average size of aggregates	346
9.2.4. Scaling laws for aggregates	349
9.3. Compaction of the sedimented layer	350
9.3.1. Compaction under consolidations below the sample weight	352
9.3.2. Compaction of powders subjected to consolidations above the sample weight	355
9.4. Micromechanics of granular materials	360
9.5. Correlation between the AFM and SPT measurements	362
9.6. Contact forces in the bulk: qualitative comparison with theory	365
10. Flow regime boundaries in cohesive powders	365
11. Conclusion	370
Acknowledgements	372
References	372

## 1. Introduction

A granular material is a multiphase medium consisting of an assembly of solid particles in contact with a gas and/or a liquid. A typical example is dry sand (solid–air), wet sand (solid–air–water) or saturated sand (solid–water) as shown in figure 1. It is well known that wet sand behaves quite differently to dry or saturated sand. Wet sand may present vertical slopes, and fracture before breaking. On the contrary dry sand may easily flow, with collisions between individual grains playing a fundamental role. In these collisions gas interaction is in most cases negligible. In wet sand these collisional regimes, also called inertial regimes, are absent as particles always aggregate, and flows are dominated by friction and cohesion. This qualitative



Figure 1. Sandcastle.

difference in behaviour between dry and wet sand is ascribed to the presence in the latter of liquid bridges that give rise to strong interparticle capillary forces acting between particles [1]. These forces may be one thousand times the weight of a sand grain. We should expect then that, independently of the physical origin of interparticle forces, and in the absence of gas interaction, granular materials will behave similarly to dry or wet sand if these forces are much smaller or much larger than the weight of a single particle. Therefore, the ratio between the attractive interparticle force,  $F_a$ , to particle weight,  $mg$ , called the *cohesive granular Bond number*,  $Bo_g = F_a/mg$ , serves to divide granular materials in two large groups: cohesive (non-cohesive) granular materials are characterized by large (small) cohesive granular Bond numbers. Since the interparticle force depends on the local radius of curvature at contact [2], and its strength decreases with decreasing local asperity radius, it follows that irregularly shaped fine particles flow better than round particles. For this reason fine particles are coated with hard nanoparticles, called flow control additives, in order to decrease the local radius of curvature at contact, and in this way to reduce cohesion. Similarly, if interparticle forces are kept constant (same material and roughness), an increase in the size of the particles decreases powder cohesion.

Flowability and interparticle forces are closely related. We may say that *powders that pack well flow well*. In effect if grains have a weight much larger than the attractive interparticle forces they may easily roll over one another and, as a consequence, they pack in tighter structures, and flow easily. Everyone knows that coffee or rice (noncohesive grains) may be poured directly from the container as if it were a liquid, but no one will pour flour (cohesive powder) from the container in the same way. It is also well known that disordered structures of noncohesive spherical grains subject to their own weight have a solid volume fraction between 0.64 (random close packing, RCP) [3, 4] and 0.56 (random loose packing, RLP) [5, 6]. On the contrary fine powders may pack with a solid fraction as low as 0.18 (ballistic deposition of infinitely cohesive particles) [7], and micron-size particles based on polymers typically pack between 0.3 and 0.5, as shown in this review. Therefore, cohesion affects in a fundamental way the packing properties as well as the breaking and flow, and they are crucially important in the design of industrial storage and delivery devices for these fine powders.

However, fine powders differ from wet sand in respect to gas interaction. The behaviour of wet sand is rather insensitive to interstitial air, contrary to fine powders which are extremely sensitive to ambient gas. For a grain of sand of diameter,  $d_p = 1\text{ mm}$ , made of quartz (density  $2.6 \times 10^3\text{ kg/m}^3$ ) its terminal fall velocity in air (density  $1.23\text{ kg/m}^3$ , viscosity  $1.73 \times 10^{-5}\text{ Ns/m}^2$ ) is  $v_t = mg/3\pi\eta d_p = 82\text{ m/s}$ , while for a ten micron sized particle of polymer (density  $1.2 \times 10^3\text{ kg/m}^3$ ) the terminal velocity is of the order of  $4\text{ mm/s}$ . Powders made from the latter particles may get fluidized without difficulty as any one can easily verify shaking a bottle of toner, or by pouring toner in a bottle or on a table. In the former case the toner forms a horizontal surface as liquids do, while in the latter case the toner spreads like a liquid surrounded by a cloud of particles in suspension. Because of this, industrial devices for handling loosely consolidated samples of fine particles must be designed taking this effect into account. We will show that quasi-elastic collisional regimes with negligible particle–gas interaction,

also called inertial regimes, are absent in fine powders, since powders transit directly from plastic flows to fluidization. This strong gas–particle interaction is always present whenever there is a flow of interstitial gas. This gas flow may be imposed from outside as in fluidized beds, or may arise because of entrapped air in avalanches or flows. It may cause flooding while discharging a silo, but it may also be beneficial as this interaction enables new technologies to facilitate transport, and mixing of powders through partial or complete fluidization. Everyone concerned with handling of powders is aware that these processes are of great industrial importance, and need a fundamental understanding.

## **2. Scope of the paper**

The paper will address the physics of dry cohesive granular materials, and in particular of dry fine neutral powders. Ultrafine powders (nanopowders) are not covered in this review, since contact theories based on continuum mechanics are of doubtful validity for such small particles [8]. In addition the interparticle forces in nanoparticles can vary widely, ranging from long range (compared to particle size), relatively weak van der Waals interactions, to short range chemically mediated repulsive or attractive interactions, or they may be due to strong solid-state necking because of molecular diffusion between particles [9, 10]. Nevertheless, as mentioned in the introduction, we need to consider the effect that coating by nanoparticles has on the adhesion of fine particles. These nanoparticles, called flow additives, are hydrophobic hard particles of 7–9 nm diameter made of silica or titanium dioxide. We follow the common assumption that in this case nanoparticle–nanoparticle interaction is given by van der Waals force [11], as at ambient temperature sintering is negligible for these materials. Also, these materials are specifically treated to avoid humidity and H-bond or other chemical bond effects (more details about these particles will be given in section 6). The behaviour of noncohesive grains will be shown only to demonstrate the difference in qualitative behaviour between them.

We begin with the description of isolated grains. We continue with a discussion of the nature of interparticle forces between two powder grains, restricting our attention to normal attractive interparticle forces as they are the hallmark of cohesive powders, and because from preliminary numerical simulations for small soft particle systems, the bulk behaviour is dominated by normal forces [12] (for a comprehensive review on the forces between small particles, both normal and tangential, see [13]). These attractive forces may be of electrostatic, dispersion or van der Waals, magnetic, and of capillary origin. Here we restrict our attention to the case of van der Waals forces, which are typically dominant in uncharged fine dry powders [14, 15] (the reader interested in wet powders and grains may see the recent review by Herminghaus [16]). Most of the experimental results reported here are for a particular class of fine powders, i.e. xerographic toners. However, we believe that the arguments and physical ideas discussed here are of much greater generality, since many fundamental features of cohesive granular materials do not depend specifically on the nature of interparticle forces, but on the value of the cohesive granular Bond number.

Under the action of attractive forces, and independently of its nature, the particles deform elastically and they may flow plastically in short contact times or visco-elastically/visco-plastically in longer times. As a result the force needed to separate two grains (pull-off force) is a function of the compressive force (pull-on force) and a set of physical parameters of the grain, i.e. Young's modulus, coefficient of Poisson, surface hardness, interfacial energy, radius of the particle, and local curvature at the area of contact. For longer times the pull-off force is, in addition, a function of viscosity, or softening/hardening rules. These forces are measured by the Atomic Force Microscope (AFM) for short contact times to avoid viscosity effects, and they are analysed in detail for polymer-based particles coated with flow-control additives.

In the next step we investigate powders at the bulk level neglecting gas interaction. As is the case for all granular media, their bulk properties depend on the geometry of particle positions, the geometry of contacts and the strength and direction of interparticle forces at each contact. The essential difficulty we have to face at low consolidations is the extreme sensitivity of the geometry of particles and the geometry of contacts to weak external forces and boundary conditions. Because of this, fine powders suffer structure transitions quite easily, and after each change we have a 'new material'. This is why for any powder sample its mechanical properties depend on its past history. The most important problem then is to go beyond a qualitative measure of flowability and to obtain quantitative reproducible measurements.

We describe a powder bed technique which enables us to produce initial states "microscopically" different but macroscopically equivalent. This technique yields reproducible measurements of density and a specific kind of tensile stress, called oedometric or uniaxial tensile stress. In this technique the powder is first fluidized beyond the bubbling point by imposing a gas flow as high as necessary, in order to erase as much as possible the memory of the initial state. Then the powder is allowed to settle under its own weight, cutting off the gas. Once the powder settled, the gas flows upwards until the powder layer breaks. Measuring the over-pressure, i.e. the excess of pressure above the powder weight per unit cross-sectional area, allows us to determine the tensile stress of the powder. We present extensive measurements of the packing solid fraction, and tensile stress as a function of compressive load, and particle properties (Young's modulus, radius of the particle, average size of the asperities, surface energy, and surface area coverage, hardness and size of the flow control additives).

Next we want to link the tensile stress to interparticles forces. Because of the use of gas in the powder tester we need to consider the influence of interstitial gas in the dynamics of powders. It is well-known that interparticle forces affect crucially the fluidization of particles [17]. Gas-particle interaction may be rationalized in terms of three dimensionless parameters: Reynolds number, Froude number, and cohesive granular Bond number. The Reynolds number, which is the ratio of the convective to the viscous term in the Navier-Stokes equation, is based on the typical radius of the tortuous channels along which the gas flows (which are of the order of the particle's radius  $r_p = d_p/2$ ), and it is defined as  $Re = \rho_f v_i d_p / 2\eta$ , with  $\rho_f$  the gas density,  $v_i$  the free fall velocity of an isolated particle in an unbounded gas ( $v_i = mg/3\pi\eta d_p$ ), and  $\eta$  gas viscosity. This number is quite small for fine powders, thus indicating that inertial terms in the fluid flow may be neglected. The other characteristic number is the Froude number  $Fr = v_i^2/d_p g$  (proportional to Stokes number  $St = m_p v_i / 6\pi\eta r_p^2$ ).

This Froude number is also small, a characteristic associated empirically with the possibility of homogeneous fluidization [18]. In addition, we have to consider the cohesive granular Bond number,  $Bo_g = F_a/mg$ , with  $F_a$  the attractive force between two grains. For large values of this number the particles tends to aggregate. We find that a useful combination of the two former dimensionless numbers is the number  $C = \rho_p v_i^2 d_p^2 / F_a$  as shown in [19].

Particles are rarely spherical, but it is possible to define an equivalent volume diameter (section 3). Unless they are needle-like or plate-like, the estimations based on this diameter are quite reasonable as confirmed by numerous experimental investigations. From these dimensionless numbers it is clear than the size and density of the particles are central quantities in their description. If the particles break during powder processing these numbers change and we must take into account their evolution in time. Here we consider that the particles keep their integrity.

In the Geldart classification for fluidization of granular materials [20] fine powders may be of A type (aeratable or homogeneously fluidizable) and of C type (non-fluidizable). The fuzzy boundary between both types of powders (see figure 2) may be shifted towards A type by the adequate use of flow control additives in order to reduce cohesion. We show that fine particles are strongly agglomerated and we determine through collapse experiments the average size and average number of particles of aggregates as a function of the cohesive granular Bond number. This is needed to understand the stability and fluctuations in the fluidized state. An old controversy about the relation between stability and bubbling will be

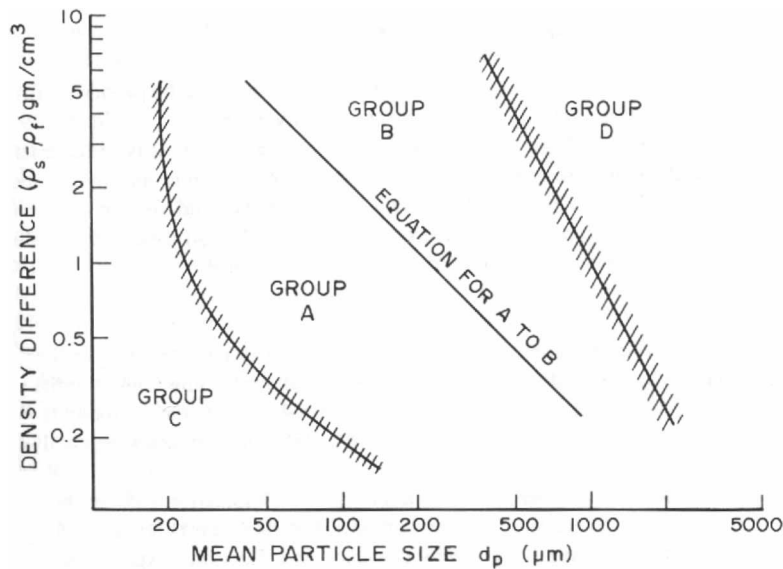


Figure 2. Geldart's diagram: Materials C are fine, very cohesive powders, and they are difficult to fluidize; materials A are easily fluidizable and they show a regime of homogeneous fluidization with an important bed expansion; materials B are made of coarse grains between 100 and 500 microns in diameter; they bubble, and bed expansion is quite small; materials D are made of large and/or very dense particles, and they tend to make spoutable beds.

discussed, and recent experiments will be reported to clarify this issue. However, our principal aim is to determine the packing structure of the settled powder layer in the fluidized bed technique. This is because, using concepts from micromechanics, it is possible to estimate from these measurements the interparticle forces, and to correlate them to the direct AFM measurements of interparticle forces. In this way we establish a relationship between the attractive interparticle forces and powder bulk behaviour.

Granular materials may have plastic flow, more or less rapid inertial flow, fluidization and suspension as a limit case of the latter. In each one of these regimes transfer of momentum between particles is governed by different physical phenomena; by friction and cohesive forces (if the latter are present) in the plastic flow, through collisions in the inertial flow, and by drag forces and collisions in the fluidization and suspension regimes. Using scaling laws we will show that *fine powders never present the inertial regime; on the contrary they go from the plastic flow to a state of gas-fluidization*. We determine the boundary between both regimes as a function of the cohesive Bond number and the imposed interstitial gas velocity.

Cohesion not only suppresses the inertial regime in fine powders, but it also governs the dynamics of plastic flow. However, due to limitations in space this topic will not be discussed here. Let us only mention that models based on the dynamics of single grains are not applicable, and we must resort to the method of wedges, of slices or other models (elastic–plastic, hypoplastic, etc.) of widespread use in soil mechanics in order to analyse the experimental results.

After a summary we finish the paper with a discussion of open problems. Among them we may cite the problem of developing a continuum theory describing the complex powder behaviour, the problem of relating more precisely the microscopic and the macroscopic forces and stresses, the transition from a discrete to a continuous description of the powders and the problem of the relation between the average stresses, motions and their fluctuations, both in the ‘solid’ state, in plastic flows and in fluidization.

We have chosen to cite recent reviews and books on the different topics in order to save space. However some important research will not be properly represented in this review, and we would like to apologize to all colleagues whose works have not been cited. This is only because of our ignorance; the vast and rapidly expanding literature both on contact forces and bulk properties of cohesive powders has made it quite difficult for us to follow all the developments in these two fields of research. Our hope is that the reader will find useful for her/his own research the way in which we have tried to clarify the relationship between attractive forces at the grain level and bulk properties.

## **Part I: Powders at the grain level**

### **3. Characterization of single powder particles**

Powders are made of assemblies of particles in an interstitial fluid. Therefore, the description of any powder should start with the properties of single particles,

such as volume, surface and shape, mass density, Young's modulus, Poisson's coefficient, hardness, surface energy, electrical, magnetic and chemical properties.

**Shape and size:** Shapes are quite different and can vary from needle-like or plate-like to spherical-like. There are several definitions of shape factors. One of the most frequently used is *sphericity*,  $\psi$ , which is defined as the ratio of the surface area of a sphere having the same volume as the particle to the actual particle surface area; the reciprocal is the coefficient of rugosity or angularity. Sphericities may have values close to one for near-spherical particles, or as low as 0.3 for platelets like mica. Another two useful parameters are the equivalent diameters that may refer to volume or surface area: the *equivalent volume diameter* is the diameter of a sphere of the same volume, and similarly the *equivalent surface diameter* is the diameter of a sphere with the same surface. Another important quantity of a particle is its specific surface area, which is defined as its real surface over its real volume. It is expressed through the sphericity,  $\psi$ , and the equivalent volume diameter,  $d_p$ , by  $S_p = 6\psi/d_p$ .

Since many shape characterizations use the images of powder particles obtained in the Scanning Electron Microscope (SEM) there are some shape factors associated to the projected area of the particle. One is *circularity* which is the ratio of the perimeter of a circle having the same area as the projected area of the particle. Another one is *chunkiness* which is the ratio of the smallest to the largest side of the rectangle that exscribe the projected area. If the height is also available then we define the *aspect ratio* as the ratio of the largest side to the height. Compactness is defined as the ratio of the inscribed circle to the exscribed one. More sophisticated characterizations using several coefficients of Fourier expansion of the shape as a function of angle may be found in the literature.

Despite the large research effort to characterize the shape properties of powder particles, there is a wide gap between the sophisticated shape descriptions that can be found in the literature and the bulk behaviour of the powder. In practice the shape factor is dictated by the process in which we are interested [21]. For example, if we are interested in sedimentation or fluidization the important number is the gyration radius or Stokes radius, which is the radius of the sphere that falls with the same velocity as the particle. In sieving we are interested in the sieve diameter, which is the minimum mesh side that allows the powder to pass after vigorous vibration and shaking. If our interest is in chemical reactions a good parameter is the ratio of surface to volume of the particle, and it is common to use it to characterize the equivalent volume diameter, also called the Sauter diameter, based on the specific area of the particle, and defined by  $d_p = 6\psi/S_p$ . The numbers we obtain depend on the way we measured them, and though all of them give useful information it is not always evident to deduce one from the other. Finally, let us mention that the particles of an assembly will seldom be of uniform size. There is a particle size distribution that characterizes the powder assembly, and this distribution function will vary depending on the shape parameter we use. The mean or average size and the standard deviation of particle sizes are the quantities typically used to characterize these distributions.

**Surface topography:** The interparticle forces between particles depend strongly on the detailed shape of their surface. Its importance was soon recognized and a large research effort was dedicated to the characterization of the surface topography.

Different statistical distributions have been used for this purpose, paying special attention to the average size of the protuberances, called asperities, as well as their distribution [2]. In another approach the surface is characterized by its fractal dimension, or more usually on the fractal dimension of its projected profile [22]. Unless the particle surface or profile are quite irregular their fractal dimension for the projected profile will be close to 2 or 1, respectively.

**Density:** In most cases the density of the particle,  $\rho_p$ , is the density of the bulk material of which the particle is made. However, when the volume measured includes closed pores within the particle, or the particle itself is produced by agglomeration or coagulation of smaller particles, the density is

$$\rho_p = (1 - e_i)\rho_s + e_i\rho_f = \phi_i\rho_s + (1 - \phi_i)\rho_f \quad (1)$$

where  $e_i$ , the internal porosity, is the ratio of the volume of internal pores to the external particle volume,  $\phi_i$  is the solid volume fraction,  $\rho_s$  the density of the solid material, and  $\rho_f$  the density of the fluid present in the pores. When the fluid is a gas, its contribution to the density is small and it can be usually neglected. In practical measurements a given amount of dry powder is weighed and we determine its volume by the volume of fluid it displaces. If the fluid is a liquid or a gas this displacement technique is called liquid or gas pycnometry [21].

The particles used here to illustrate the physics of fine cohesive powders are mostly particles utilized in the xerographic and printing industries. For comparison, we have tested either sand or glass beads of different sizes. For more specific studies we have used model particles as sold by various companies. The xerographic particles are called toners, carriers and developers. *Toners* are obtained from polymer-based solids by attrition (see figure 3a), or by aggregation of polymer chains in liquids (see figure 4). The latter are called emulsion aggregation toners or more briefly EA toners. They can have more or less convex irregular shapes in the case of attrition, and almost spherical shapes for EA particles. Toners are usually coated with nanometre size particles, called flow control additives, because they are used to decrease the interparticle attractive forces and, in that way, to increase their flowability (see figure 12b). *Carriers* are dense, larger particles made from steel or ferrite, usually coated with a polymer. *Developers* are carriers to which toners are adhered by tribocharging (see figure 3b). Here, for the sake of simplicity, we characterize the particle shape by the equivalent volume diameter. The equivalent volume diameter takes values of a few microns for toners up to 100 microns for carriers and developers. In relation to the description of surface topography we will limit ourselves to the knowledge of the local radii of curvature, that for attrition made powders are typically of the order of 0.1 microns [2], and for EA toners is the radius of the particle. This is sufficient for our purposes, because in most practical situations the contact between particles is controlled by the additives for reasons that will become clear as we proceed. The information that is crucial then is the size of these additive particles and the surface area coverage of the large powder particle. In order to minimize contact forces these additives are made of hard particles, often  $\text{SiO}_2$  or  $\text{TiO}_2$ , and the typical sizes of these additives range from 7 to 50 nanometres. The control of the force between powder particles is mainly made through variation of the size of the additives, and of its surface area coverage (*SAC*).

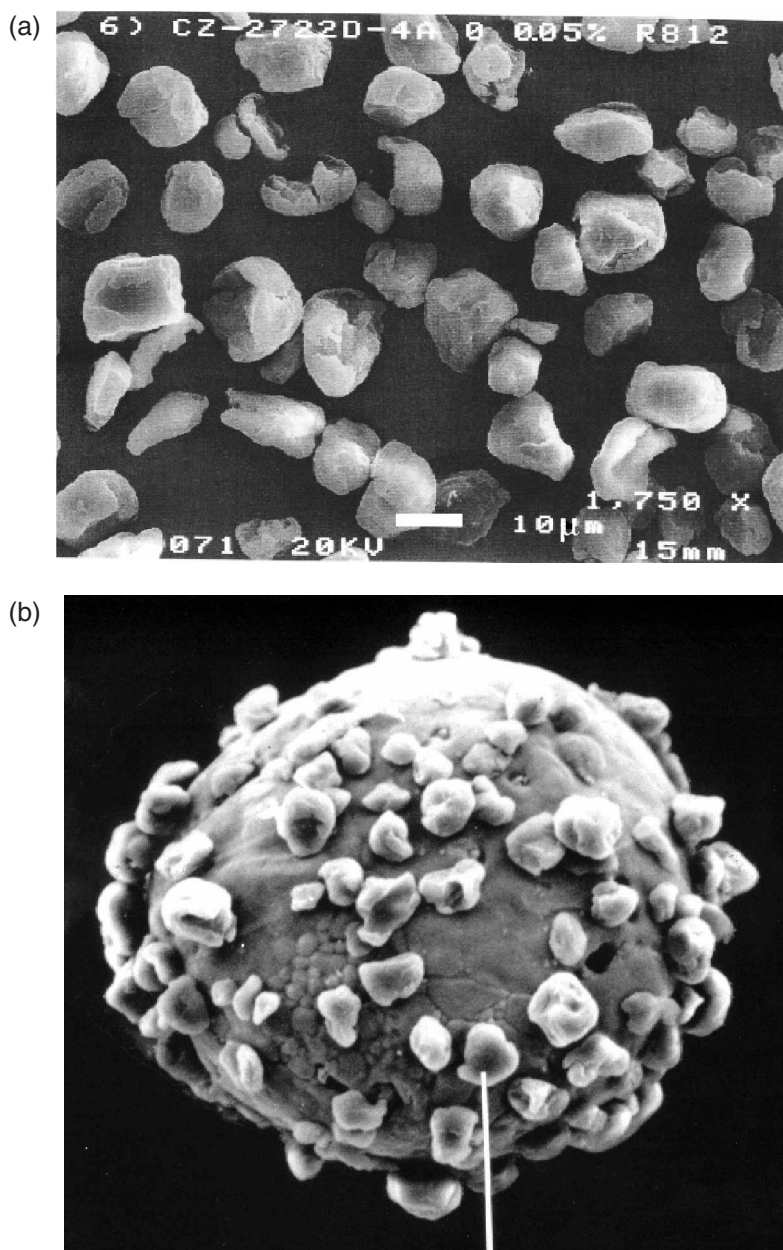


Figure 3. (a) Toners made by attrition (average size  $12\mu\text{m}$  in diameter). (b) Developer particle made by coating a ferrite particle (average size  $100\mu\text{m}$ ), called the carrier, with polymer. The particles on the surface are toner particles attached to the polymer by tribocharging.

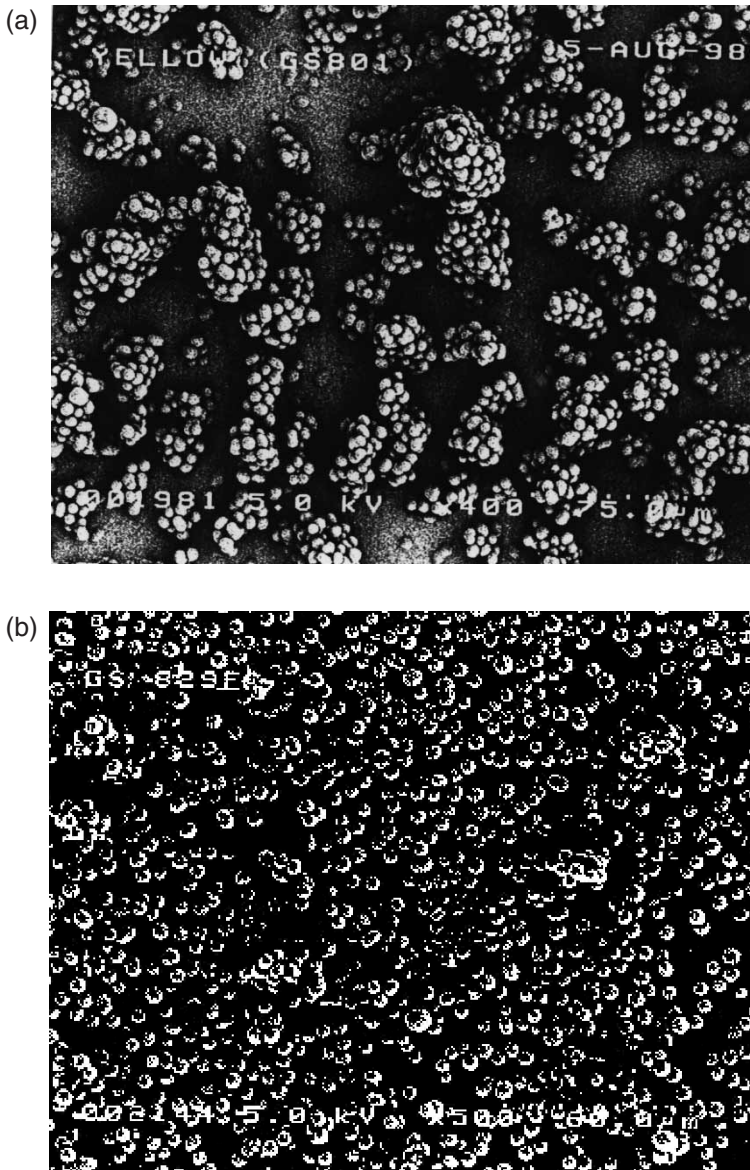


Figure 4. Emulsion aggregated toner made from polyester (average size  $4\mu\text{m}$  in diameter): (a) as obtained from the solution; (b) after fluorination.

#### 4. Van der Waals forces between rigid bodies

We begin by discussing briefly the forces between grains concentrating our attention first in rigid grains subjected to van der Waals forces. This will allow us to show the fundamental role played by surface properties and the geometry of particles.

When two particles are brought into contact they are subjected to capillary, electrostatic and van der Waals forces. Capillary forces are caused by condensed moisture on the surface of the particle. For dry granular materials these forces may be negligible compared to the other two, though in some circumstances special precautions need to be taken to avoid ambient humidity if we want to minimize the action of capillary forces. Electrostatic forces depend on the charges present in the particles. Because particles of dissimilar materials interchange charges when in contact (triboelectricity), and the charges become trapped in non-conducting particles, these contacts cause the insulating particles to be charged. In a powder that is neutral on the average there is a distribution of charges of both signs, with individual particles positive and negatively charged. Since particles tend to reorient among themselves in order to minimize the electrostatic energy there is always an attractive electrostatic interaction between particles. We need to measure in each situation this charge number distribution to estimate this force. It is admitted that, for dry fine neutral powders, the electrostatic force is negligible compared to van der Waals force [14, 15, 23].

Van der Waals forces between particles have their origin in the forces between their constituent molecules, and it is well known that molecules attract each other even if they are totally neutral. Their origin can be understood as follows: in any molecule, the instantaneous positions of the electrons around the nuclear protons give rise to a finite electric dipole, which in turn originates an electric field that polarizes a nearby molecule inducing a dipole on it. The two dipoles give rise to an attractive force between both molecules with a finite time average. When the time that the electric field takes to reach the other molecule is comparable to the period of the fluctuating dipole the two dipoles are no longer aligned in the most favourable position and the attraction forces decrease. This effect is called the retardation effect. A third molecule will modify the resulting fluctuating dipoles of the first two molecules and consequently these molecular forces are not pairwise additive. These forces are quantum mechanical in origin and a rigorous treatment needs quantum electrodynamics. However, these forces are amenable to a simplified treatment assuming that the interaction potential between two molecules  $a$  and  $b$ , separated by a distance  $r_{ab}$ , is the Lennard–Jones potential

$$V = -\frac{C_{ab}}{r_{ab}^6} + \frac{D_{ab}}{r_{ab}^{12}} \quad (2)$$

where the first term of the right-hand side, the attractive part, is the van der Waals interaction potential, with  $C_{ab}$  the London constant, and the second term is the Born repulsive term.

If we neglect retardation effects and we assume that the interaction between the molecules is pairwise it is possible to integrate analytically these potentials to obtain the interaction between particles of simple geometrical forms. We recall results from this simplified treatment because as we will see the indeterminacy due to the irregular shape of the particle and the lack of knowledge about the exact physico-chemical properties of the surface of the particle precludes any precise analytical computation of the attraction force between two grains. The information provided by this simple approximation allows us to gain a fundamental understanding of two important

parameters that determine the adhesive properties of particles, i.e. the surface energy, and the local radius of curvature of the particle at the contact.

#### 4.1. Van der Waals forces between two half-spaces

Consider the interaction between two half-spaces separated by a distance  $z$ . Integration of the Lennard–Jones potential is elementary and provides us with the potential of interaction per unit area between both half-spaces [24]:

$$U(z) = -\frac{A_{ab}}{12z^2} + \frac{B_{ab}}{z^8} \quad (3)$$

with  $A_{ab} = \pi C_{ab}\rho_a\rho_b$  the Hamaker constant and  $B_{ab} = \pi D_{ab}\rho_a\rho_b/360$ , where  $\rho_a$  and  $\rho_b$  are the molecular number densities of bodies  $a$  and  $b$ . The force is

$$F(z) = -\frac{dU}{dz} = -\frac{A_{ab}}{6z^3} + \frac{8B_{ab}}{z^9} \quad (4)$$

Rewriting the constant  $B_{ab}$  as a function of the equilibrium distance of both bodies subjected to this force per unit area we have

$$F(z) = -\frac{A_{ab}}{6z_0^3} \left[ \left( \frac{z_0}{z} \right)^3 - \left( \frac{z_0}{z} \right)^9 \right] \quad (5)$$

with  $z_0$  the equilibrium distance. This distance is estimated to be between 1 and 5 Å [14, 23–25]. The adhesive force, also called the pull-off force, is the maximum force per unit area needed to separate the bodies, and it is given by the maximum of  $F(z)$ , which is at a distance  $1.2z_0$ ,

$$F_a = \frac{A_{ab}}{9\sqrt{3}z_0^3} \quad (6)$$

The energy of adhesion is the work expended per unit area to move the bodies from  $z_0$  to infinity

$$w_{ab} = -\int_{z_0}^{\infty} F(z)dz = -U(z_0) = \frac{A_{ab}}{16z_0^2} \quad (7)$$

Therefore, it is

$$F_a = 1.03 \frac{w_{ab}}{z_0} \simeq \frac{w_{ab}}{z_0} \quad (8)$$

Because in the Lennard–Jones potential the attractive force is the van der Waals force, in most books and articles the adhesive force is calculated using only this attractive term. This amounts to replacing the Born term by an infinitely repulsive force (hard sphere potential) at  $z = z_0$ . The result is that the attractive force and work of adhesion are given by

$$F_{vdW} = \frac{A_{ab}}{6z_0^3}, \quad w_{ab} = -\int_{z_0}^{\infty} F_{vdW}(z)dz = \frac{A_{ab}}{12z_0^2} \quad (9)$$

and so  $F_{vdW} = 2w_{ab}/z_0$ . As a consequence,  $w_{ab}$  can be underestimated if we use these expressions to adjust the experimental values, though it is possible to have correct values maintaining the hard sphere potential if we shift away from the wall the

minimum of the attractive potential of the total Lennard–Jones potential [26]. Another shortcoming of the purely attractive plus hard sphere repulsive potential is that molecular dynamics to simulate these forces is not so straightforward.

However, from the practical point of view, Hamaker constants are determined through equation (9). Typical values for the Hamaker constants are about  $10^{-19}$  J for interactions across a vacuum [27]. Therefore, from equation (9), with  $z_0 = 4 \text{ \AA}$  we have  $w_{ab} \sim 0.05 \text{ J/m}^2$ . The pressure needed to separate two bodies in contact through molecularly smooth surfaces will be  $p \simeq w_{ab}/z_0 \sim 1200 \text{ atm}$ . We never observe such high values of pressures to separate solid bodies. The reason is that surfaces of ordinary bodies are rough and they contact through asperities of sizes that may be considerably larger than the effective range of the van der Waals forces, but much smaller than the bodies, thus reducing in several orders of magnitude the real area of contact between them.

**4.1.1. Surface energy.** Closely related to the work of adhesion is the concept of surface energy  $\gamma_a$ . Imagine that an imaginary plane divides an infinite body into two half-spaces. The work needed to separate the two half-spaces to infinity, in an isothermal and reversible way, is the work of adhesion and must be equal to the energy stored in these two surfaces. Therefore,  $w_{aa} = 2\gamma_a$ . If two dissimilar materials are in contact through this plane, the energy of adhesion plus the energy stored in this surface (the interfacial energy) must be equal to the surface energy of the two newly created surfaces

$$w_{ab} + \gamma_{ab} = \gamma_a + \gamma_b \quad (10)$$

and consequently  $w_{ab} = \gamma_a + \gamma_b - \gamma_{ab}$ . For the same material  $a = b$  and  $\gamma_{aa} = 0$  and we recover  $w_{aa} = 2\gamma_{aa}$ .

In terms of  $w_{ab} = A_{ab}/16z_0^2$  (equation (7)), the force per unit area is given by

$$F(z) = -\frac{8w_{ab}}{3z_0} \left[ \left( \frac{z_0}{z} \right)^3 - \left( \frac{z_0}{z} \right)^9 \right] \quad (11)$$

The use of  $w_{aa}$  to predict the surface energy of materials gives the correct order of magnitude for many ordinary solids and liquids (for a discussion see [24, 25]). However, in metals this expression seriously underestimates the surface energy. In addition, the presence of minute traces of foreign substances greatly affects its value. In general, the surface energy is quite sensitive to the presence of the highly polar H-bonds or other chemical bonds. Therefore, the work of adhesion depends on the chemical and physical state of the surface [28]. Contamination of the surface, impurities, fractures, and chemical bonds may change the surface energy in a substantial way. For example, we show in figure 4 powder grains made from the same material by an emulsion aggregated process. The only difference is that the surface of the powder particles in figure 4b has been fluorinated, and this has reduced their surface energy compared to the same untreated material. Because of this, these particles do not agglomerate as untreated particles do. For more examples of surface energy modification, including organic coated surfaces, cell adhesion and toxin–receptor interactions, see the book by Kendall [29].

#### 4.2. Van der Waals forces between a half-space and a sphere with radius $R$

The interaction potential is given by [24]

$$U(z) = -\frac{A_{ab}}{6} \left[ \frac{2R(R+z)}{(2R+z)z} + \ln \frac{z}{2R+z} \right] + \frac{B_{ab}}{6} \left[ \frac{6R-z}{z^7} + \frac{8R+z}{(2R+z)^7} \right] \quad (12)$$

and the force is

$$F(z) = -\frac{2R^3 A_{ab}}{3z^2(2R+z)^2} + B_{ab} \left[ \frac{7R-z}{z^8} + \frac{9R+z}{(2R+z)^8} \right] \quad (13)$$

with  $A_{ab} = \pi^2 C_{ab} \rho_a \rho_b$  and  $B_{ab} = \pi^2 D_{ab} \rho_a \rho_b / 1260$ . For spheres with radius large compared to the separation distance is

$$U(z) = -\frac{A_{ab}R}{6} \frac{R}{z} + B_{ab} \frac{R}{z^7} \quad (14)$$

The force can be approximated with enough accuracy by

$$F(z) = -\frac{A_{ab}R}{6z^2} + B_{ab} \frac{7R}{z^8} \quad (15)$$

We may rewrite  $B_{ab}$  in terms of  $z_0$ , the equilibrium distance.  $B_{ab} = A_{ab}z_0^6/42$ , and therefore it is

$$F(z) = -\frac{A_{ab}R}{6z_0^2} \left[ \left( \frac{z_0}{z} \right)^2 - \left( \frac{z_0}{z} \right)^8 \right] \quad (16)$$

The pull-off force is given by the maximum of the force that happens to be at  $z_m = 2^{1/3}z_0$ ,

$$F_a = \frac{A_{ab}R}{2^{10/3}z_0^2} \simeq \frac{A_{ab}R}{10z_0^2} \quad (17)$$

The surface energy is  $w_{ab} = -U(z_0) = 9A_{ab}R/710^{10/3}z_0$ , and therefore

$$F_a = \frac{7w_{ab}}{9} \approx \frac{w_{ab}}{z_0} \quad (18)$$

Clearly, as the force given by equation (13) decreases faster than the expression given by equation (16), the value of  $U(z_0)$  is overestimated, and the ratio of  $F_a$  to the work of adhesion  $w_{ab}$  is smaller. Also, if we look at equations (8) and (18) we may get the wrong impression that the pull-force is the same. However, we must substitute in each expression the value of  $z_0$ , which is smaller for the plane–plane configuration than for the plane–sphere one ( $z_0^{p-p} = 0.85z_0^{s-p}$ ). Because the value of  $z_0$  is not known with enough precision to distinguish between both values we disregard these differences and we use the corresponding expressions and, in what follows, we will take  $z_0 = 4 \text{ \AA}$  as previously stated.

### 4.3. Van der Waals forces between two rigid spheres

The interaction potential is

$$\begin{aligned}
 U(z) = & -\frac{A_{ab}}{6} \left[ \frac{2R_a R_b}{z^2 + 2(R_a + R_b)z} + \frac{2R_a R_b}{z^2 + 2(R_a + R_b)z + 4R_a R_b} \right. \\
 & \left. + \ln \frac{z^2 + 2(R_a + R_b)z}{z^2 + 2(R_a + R_b)z + 4R_a R_b} \right] \\
 & + \frac{B_{ab}}{30(R_a + R_b + z)} \left[ \frac{30R_a R_b - 5(R_a + R_b) + z^2}{z^7} \right. \\
 & + \frac{R_a(40R_a - 14R_b) + (5R_a - 9R_b) - z^2}{(2R_a + z)^7} \\
 & + \frac{R_b(40R_b - 14R_a) + (5R_b - 9R_a) - z^2}{(2R_b + z)^7} \\
 & \left. + \frac{14(R_a^2 + R_b^2) + 58R_a R_b + 9(R_a + R_b)z + z^2}{(2R_a + 2R_b + z)^7} \right], \quad (19)
 \end{aligned}$$

where  $R_a$ ,  $R_b$  are the radii of the spheres and  $z$  their separation. The solution for the attractive part may be found in [27]. It is straightforward to verify that this expression reduces to expression (13) in the limit  $R_i \rightarrow \infty$ , with  $i=1, 2$ . For radii much larger than the separation  $z$  the expression reduces to (14) with  $1/R = 1/R_a + 1/R_b$ , and the force is half of the pull-off force between a sphere and a plane.

### 4.4. Van der Waals forces between two nonconforming convex bodies: the Derjaguin approximation

Because of all the uncertainties associated with the value of  $z_0$ , and the limitations of the molecular approach or the continuum approach of van der Waals forces, it has been common practice to follow the Derjaguin approximation for the interaction energy between convex solids that may be curved and slightly inclined to each other. This approximation is based on assuming a law of force density between surfaces equal to the force per unit area between two half-spaces. This expression is assumed to be valid for the local separation between the two bodies.

Consider two non-conforming bodies that touch each other at a single point  $O$  as depicted in figure 5. Draw the  $z$ -axis in the direction of the common normal. If we count distances to the tangent plane (the plane passing through  $O$  and perpendicular to the  $z$ -axis) as positive for each body, we have  $z = z_a + z_b = f_a(x_a, y_a) + f_b(x_b, y_b)$ . Then the profile of each body close to the origin may be expressed as

$$z_i = \frac{x_i^2}{2R_{1i}} + \frac{y_i^2}{2R_{2i}} \quad (20)$$

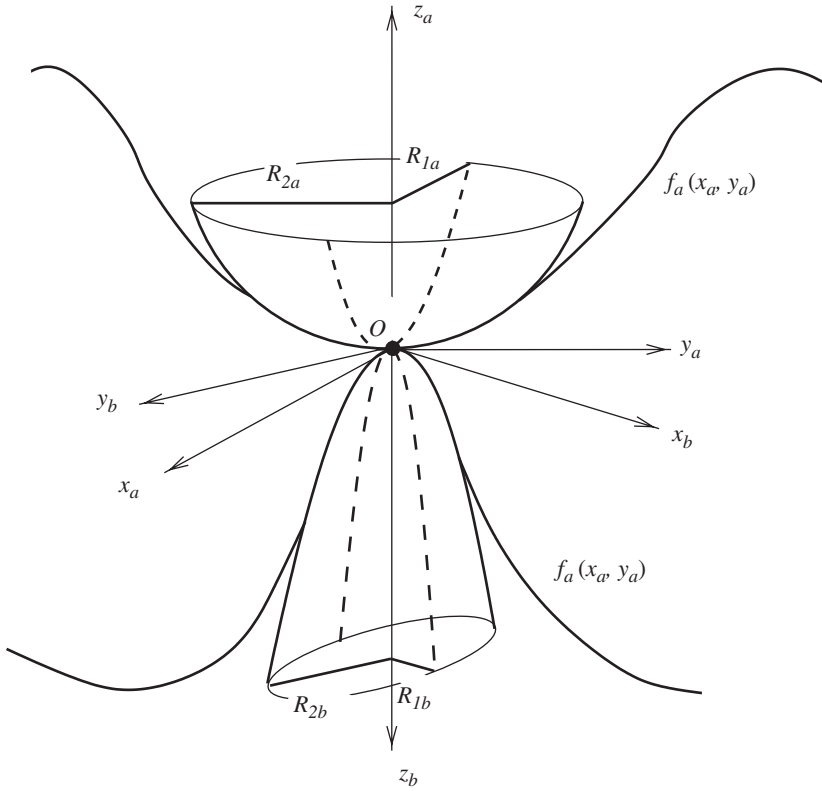


Figure 5. Contact between two non-conforming bodies; local approximation.

with  $x_i$  and  $y_i$  the horizontal axes along the local radii of curvature  $R_{1i}$  and  $R_{2i} \times (i = a, b)$ . The two set of axes are not the same in general, but it is possible to transform the coordinates to a common set of axis  $x, y$  where the gap between the surfaces can be written, up to second order terms, as [30]

$$z = Ax^2 + By^2 \tag{21}$$

with

$$A + B = \left( \frac{1}{R_{1a}} + \frac{1}{R_{2a}} + \frac{1}{R_{1b}} + \frac{1}{R_{2b}} \right) \tag{22}$$

and

$$4|A - B|^2 = \left( \frac{1}{R_{1a}} - \frac{1}{R_{2a}} \right)^2 + \left( \frac{1}{R_{1b}} - \frac{1}{R_{2b}} \right)^2 + 2 \left( \frac{1}{R_{1a}} - \frac{1}{R_{2a}} \right) \left( \frac{1}{R_{1b}} - \frac{1}{R_{2b}} \right) \cos 2\alpha_{ab}$$

Here  $\alpha_{ab}$  denotes the angle between the  $x_a$  and  $x_b$  axes.

In the case of two axisymmetric bodies touching each other at the axis of revolution is  $A = B$ . The local separation between both is given by  $z = r^2/2R$ , with  $r$  the radial coordinate in the tangent plane, and  $1/R = 1/R_a + 1/R_b$  the reduced radius of the sphere. This amounts to replacing each body by a paraboloid with the local radius of curvature at the tip. Under this approximation we have

$$F_a = \int_{z_0}^{\infty} 2\pi r F_{vdW}(z) dr = 2\pi R \int_{z_0}^{\infty} f(z) dz = 2\pi R w_{ab} = 2\pi R (\gamma_a + \gamma_b - \gamma_{ab}) \quad (23)$$

with  $F_{vdW}(z)$  the van der Waals force per unit area of two half spaces separated by a distance  $z$ . It is expected that the error introduced by putting the upper limit to  $\infty$  will be small as molecular forces decrease very rapidly as a function of distance. This expression is accurate enough for all kinds of interactions, so long as the range of interaction and the separation of the bodies is much less than the local radii of curvature (a refinement of the Derjaguin approximation has been done in [31]).

For the case of two spheres the reduced radius of curvature is given by  $R = R_a R_b / (R_a + R_b)$ . For two equal spheres  $R$  is half the radius of the sphere, while for a sphere touching a plane  $R$  is equal to the radius of the sphere. Thus, both  $F_a$  and  $F_a$  between two spheres is half of the pull-off force between a sphere and a plane.

#### 4.5. The effect of asperities

The roughness of the surface has a large effect on the adhesion force, and changing roughness can change the van der Waals interaction by up to several orders of magnitude, as shown below. Most theoretical models model the surface with hemispheres of randomly selected size placed at random locations on a simulated surface until the model surface has the same mean roughness height, the same standard deviation about the mean height, and the same fractional surface coverage by asperities as the real surface [32]. For grains of the order of ten microns, produced by attrition, the typical size (diameter) of the asperities is of the order of  $0.2 \mu\text{m}$  [2, 33]. Given the short range of surface forces compared to the typical sizes of these asperities we may see that, in general, the force is given by the typical radius of these asperities. If we denote the reduced diameter of the asperity by  $d_{asp}$  the force of adhesion of two grains of radius  $R$  in contact at a common point of two asperities is  $F_a = \pi d_{asp} w$ . The effective contact area is determined by one, two or at most three asperities. Consequently, the adhesion force can be grossly overestimated if we use the radii of the particles. However, if the size of the asperity is less than or of the order of the range of van der Waals forces, we need a more precise calculation. This has been done by Forsyth and Rhodes [34] for a sphere of radius  $R$  with spherical asperities that protrude from the sphere. For an asperity in the form of a hemispherical cap of radius  $r_{asp}$ , they found that when the asperity touches a rigid half-space without deformation, the force due only to the asperity is given by

$$F_{vdW}^{asp} = \frac{2Ar_{asp}^3}{3z_0^2(2r_{asp} + z_0)^2} \quad (24)$$

while the force due to the sphere is

$$F_{vdW}^{sph} = \frac{2AR^3}{3(z_0 + r_{asp})^2(z_0 + r_{asp} + 2R)^2} \quad (25)$$

with  $z_0$  a few Å. Therefore, for  $z_0 \ll r_{asp} \ll R$  we have

$$\frac{F_{vdW}^{sph}}{F_{vdW}^{asp}} \simeq \frac{Rz_0^2}{r_{asp}^3} \quad (26)$$

and the particle contributes for values of  $r_{asp} \sim (Rz_0^2)^{1/3}$  or less. For concreteness let us take  $z_0 = 4 \text{ Å}$ , and  $R = 10 \text{ μm}$ ; then only for asperities of the order of 10 nm, or smaller, must we take into account the particle radius. Obviously, if the asperity radii are much smaller we may neglect their contribution.

#### 4.6. The effect of retardation

When the time that the electric field takes to reach the other molecule is comparable to the period of the fluctuating dipole, the dipole–dipole interaction is reduced as the distances between molecules increase. Based on the results obtained by Casimir and Polder [35] for this retardation effect, Overbeck [36] corrected the attractive part of the Lennard–Jones potential, equation (2), for two molecules as

$$V = -\frac{C_{ab}}{r_{ab}^6} f(p) \quad (27)$$

The correction factor  $f(p)$  is given by  $f(p) = 1.1 - 0.14p$  for  $0 < p < 3$ , and  $f(p) = 2.45/p - 2.04/p^2$  for  $p > 3$ , with  $p = 2\pi r/\lambda$  where  $\lambda = 0.1 \text{ μm}$  is the characteristic wavelength of the interaction. Integrating this potential Overbeck calculated the force of attraction between two half-spaces separated by a distance  $z$ . Using the Derjaguin approximation, and the expression found by Overbeck for two half-spaces, Gregory obtained the attractive part of the Lennard–Jones potential between two spheres as

$$U(z) = -\frac{A_{ab}}{6} \left( \frac{2R_a R_b}{z^2 + 2(R_a + R_b)z} \right) \left[ 1 - \frac{5.32z}{\lambda} \ln \left( 1 + \frac{\lambda}{5.32z} \right) \right] \quad (28)$$

This expression is valid only for distances  $z \ll R_a, R_b$ . This restriction is imposed by the Derjaguin approximation and has no relation to retardation, but it is not a serious limitation in practice, since it agrees fairly well with more “exact” computations. The reader is referred to Gregory [37] where she/he can find several other approximate expressions for the interaction between flat plates, sphere and plate, and two spheres.

#### 4.7. Cohesive–noncohesive particle boundary

The force needed to separate two particles in contact is given by

$$F_a = \frac{AR}{2^{10/3} z_0^2} \simeq \frac{AD}{20z_0^2} \quad (29)$$

with  $D=2R$ , and  $R$  the reduced local radius of curvature. If particles are perfect spheres of diameter  $d_p$ , is  $D = d_p/2$ . The cohesive granular Bond number is

$$Bo_g = \frac{3A}{20\pi\rho g d_p^2 z_0^2} \tag{30}$$

For irregular particles with asperities of typical size  $d_{asp}$ ,  $D = d_{asp}/2$ , and consequently the attractive force may be greatly reduced. The cohesive granular Bond number is then

$$Bo_g = \frac{3A d_{asp}}{20\pi\rho g d_p^2 z_0^2} \tag{31}$$

We assume that the transition between cohesive and noncohesive particles is given by  $Bo_g = 1$ . Polymers have densities of  $1.1 \times 10^3 \text{ kg/m}^3$ , and Hamaker constants of the order of  $0.5 \times 10^{-19} \text{ J}$ , therefore the boundary for smooth spheres is for 2 mm. For non-smooth spheres with asperity reduced diameter of the order of  $0.1\mu\text{m}$  the boundary is for particles of volume equivalent diameter of  $75\mu\text{m}$ . Of course this boundary is not defined very precisely, but nevertheless give us a fairly good estimation to discriminate between fine and coarse grains. As is apparent from figure 6 irregular fine particles are less cohesive than smooth fine particles, i.e. for the same size the cohesive granular Bond number for the rough particle is  $d_{asp}/d_p$  smaller than for smooth particles. Consequently irregular particles flow better than perfect spheres. This is contrary to the case of large particles for which spheres roll better than irregular particles, a fact that seems obvious and intuitive to us, simply because it is the result of our daily experience. Another important consequence is that departure from the spherical shape is not crucial to estimate the interparticle forces between two grains.

In industry it is common practice to coat the particles with small, hard nanoparticles to reduce cohesion. Living beings have developed different sophisticated approaches to reduce cohesion between small particles such as pollen or spores. Some kinds of pollen get charged, after drying in the flower, to facilitate their dispersion. The spores of the puff-ball, on the other hand, show a nice example of the role of asperities to reduce the interparticle forces, as can be seen from figure 7. Because of this they are easily dispersed in air when we accidentally step on the fungus.

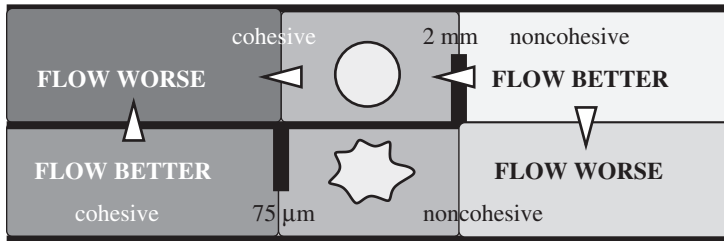


Figure 6. Fine-coarse boundary for smooth and non-smooth particles, in terms of their volume equivalent diameter. The arrows indicate the direct comparison between contiguous domains. The obvious fact that large cohesive particles flow better than fine cohesive ones is not explicitly indicated in the diagram.

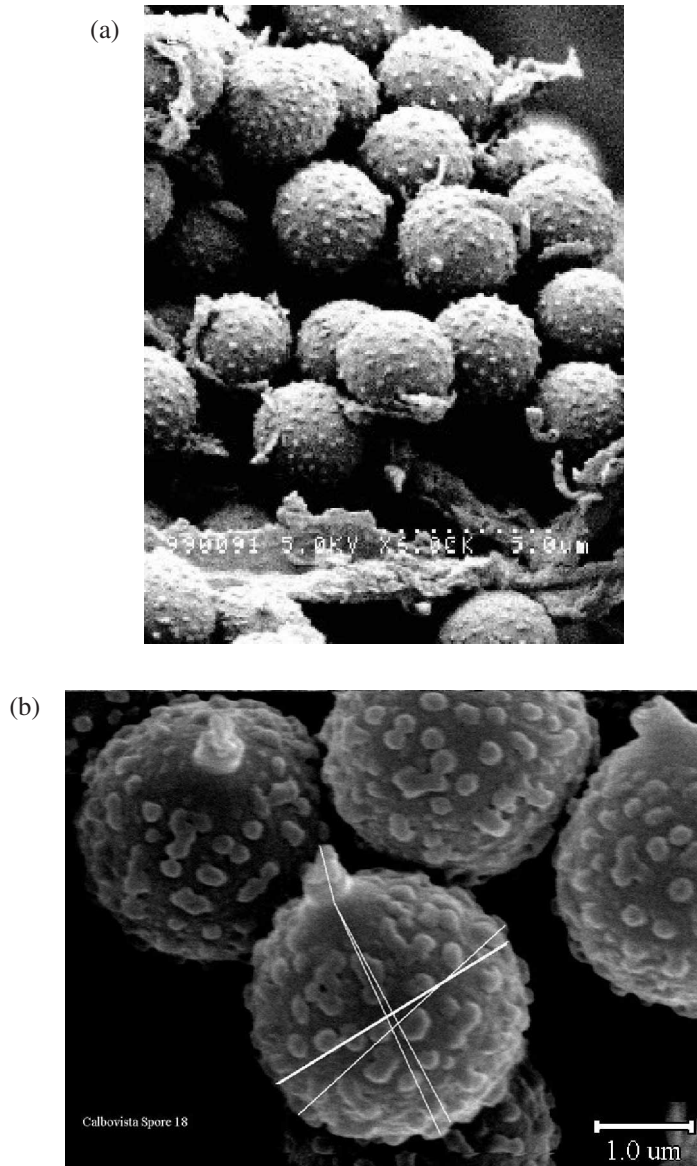


Figure 7. (a) Puff-ball spores; (b) a closer view of their surfaces. We may clearly appreciate the protuberances on the surface that decrease adhesion between particles.

### 5. Normal forces between deformable bodies

It is a universal characteristic of powders that their tensile strength, i.e. the force per unit area needed to break them apart in the absence of shear, depends on the isotropic compressive pressure to which they have been previously subjected. As we increase the confining pressure the tensile strength also increases. In general,

this increase in the tensile strength can be attributed, on one hand, to the increase in the number of contacts as we increase the confining pressure and, on the other, to the presence of plasticity at contact. In the latter case, the force needed to separate two particles at a single contact, i.e. the pull-off force, depends on the previous load force applied to both particles, the so-called pull-on force, contrary to the case of a purely elastic contact.

The determination of the pull-off force, as a function of the confining load plus the attractive forces, acting between two bodies comprises two steps. First we must determine how the bodies deform under the compressive forces as they come from infinity until they reach the final equilibrium, and secondly, we must solve the subsequent evolution of their profiles as we unload the external forces and we overcome the attractive forces so that they separate again to large distances. The first problem, called the indentation problem, is quite complex as the bodies begin to deform even before they touch due to the attractive forces among their molecules. When in contact they continue to deform under the combined action of the external load and the molecular attractive forces, the latter increasing during the indentation process as more and more molecules accumulate in the neighbourhood of the contact area. This process is stopped by the repulsive elastic stresses that develop in the bodies. However, if the attractive forces (alone or combined with the external load) are high enough, parts of the body may overcome the elastic limit and a plastic flow will develop on short time scales and a viscoplastic flow on larger time scales. The inverse problem of unloading is also of great complexity, as we have to calculate the profile of each body under the presence of partial plastic flow, relaxation of elastic stresses and decreasing attractive forces. Therefore, it is not a surprise that this problem has so far defied complete solution, and only in some limiting situations there exist analytical solutions. Though it is obvious that for purely elastic deformations, and therefore perfectly reversible, the pull-off force will depend on the attractive adhesive forces, and not on the external load, even the solution for this problem is not known in general.

The aim of this section is to understand the physical parameters that determine the pull-off between particles in order to design the cohesive properties of powders. As a result of these discussions, the crucial role played by the Young's modulus and yield strength of the constituent material of the grains will become evident. An important conclusion is that the dependence of the pull-off force on the pull-on force implies that either we have an increasing number of asperities in contact as we increase the load, or, if the contact is through one asperity only, there must always be present a certain degree of plasticity at the contact region, or both.

### **5.1. Elastic contact**

We briefly review the results known for the case of indentation of two smooth, non-conforming axi-symmetric bodies, discarding viscosity effects, that is, we are interested in contacts that last a short time, but long enough to consider the loading and unloading as a quasistatic process. The known analytical or semi-analytical solution for these contact problems have been derived under the following assumptions: (a) the radius of the contact area is much smaller than the local

radii of curvature); (b) each body is approximated by an elastic half-space loaded over the contact area; (c) the strains are sufficiently small for linear elasticity to be valid; and (d) the contact is frictionless or the solids have identical Young's moduli and Poisson ratios, so that only a normal pressure is transmitted. Under these conditions the sum of the vertical displacements of the elastic particles,  $u(r) = u_1(r) + u_2(r)$ , is given by [38]

$$u(r) = \frac{1}{\pi E} \int \frac{p(r') dS'}{|\mathbf{r} - \mathbf{r}'|} = \frac{4}{\pi E} \int_0^\infty \frac{r' p(r')}{r + r'} K\left(\frac{2\sqrt{rr'}}{r + r'}\right) dr' \quad (32)$$

where  $p(r')$  is the normal pressure acting at point  $\mathbf{r}'$  on the tangent plane (considered as positive if compressive),

$$\frac{1}{E} = \frac{1 - \nu_a^2}{E_a} + \frac{1 - \nu_b^2}{E_b} \quad (33)$$

with  $E_i$  and  $\nu_i$  ( $i = a, b$ ) the Young's modulus and Poisson's coefficient of each body, and  $K(k)$  the complete elliptic integral of the first kind of modulus  $k$ . Since the gap between both bodies may be expressed as

$$h(r) = -\delta + z_0 + \frac{r^2}{2R} + u(r) \quad (34)$$

where  $z_0$  stands for the equilibrium distance between two flat surfaces at which the pressure due to molecular forces vanishes, and

$$\frac{1}{R} = \frac{1}{R_a} + \frac{1}{R_b}, \quad \delta = \delta_a + \delta_b \quad (35)$$

with  $\delta_i$  the displacement of the undisturbed distant parts of each body, equation (32) may be written in terms of the gap between the two bodies.

**5.1.1. Nonadhesive elastic contact: Hertz solution.** In the absence of molecular forces the contact area is a circle of radius  $a$ , and  $z_0 = 0$ . Hertz proposed a pressure distribution

$$p(r) = p_0 \left(1 - \frac{r^2}{a^2}\right)^{1/2} \quad (36)$$

and he obtained  $a$  as a function of the load  $P$ , now called the Hertz solution,

$$a = \left( \frac{3RP}{4E} \right)^{1/3} \quad (37)$$

$$\delta = \frac{a^2}{R} = \left( \frac{9P^2}{16RE^2} \right)^{1/3} \quad (38)$$

$$p_0 = \frac{2Ea}{\pi R} = \frac{3P}{2\pi a^2} = \left( \frac{6E^2P}{\pi^3 R^2} \right)^{1/3} \quad (39)$$

$$u_i(r) = \delta_i - \frac{r^2}{2R_i}, \quad \text{for } r < a \quad (40)$$

$$u_i(r) = \frac{a^2}{\pi R_i} \left[ \sqrt{\frac{r^2}{a^2} - 1} + \left( 2 - \frac{r^2}{a^2} \right) \arcsin\left(\frac{a}{r}\right) \right], \quad \text{for } r > a \quad (41)$$

with the gap between the bodies outside the circle of radius  $a$  given by

$$h^H(r) = -\frac{a^2}{R} + \frac{r^2}{2R} + \frac{1}{\pi R} \left[ a\sqrt{r^2 - a^2} + (2a^2 - r^2) \arcsin\left(\frac{a}{r}\right) \right] \quad (42)$$

Hard materials loaded within their elastic limit satisfy this condition, but soft materials with a low bulk modulus may easily have deformations that exceed the restriction to small strains, and the Hertz solution might not be applicable.

**5.1.2. Adhesive elastic contact: DMT and JKR solutions.** In the case of adhesive contact we must solve self-consistently the deformation and the stress, as the interaction between the two bodies depends on their actual profiles.

In a first approximation, Derjaguin *et al.* [39] calculated the effect of molecular forces in the Derjaguin approximation *under the assumption that the deformed profiles of the bodies were given by the Hertz theory*. They showed that the adhesion energy in the contact area is equal to the adhesion energy between the non-contacting parts of the surface, and that the maximum of the attractive force, i.e. the pull-off force, happens when the contact area reduces to a point. In this approximation the deformation of the sphere when the contact area reduces to a point (both in approaching or receding from the plane) is neglected, and therefore the result of Bradley [40] is re-obtained,

$$F_a = 2\pi R w \quad (43)$$

where, from now on,  $w$  stands for  $w_{ab}$ .

In parallel, another approach based on contact mechanics was developed by K.L. Johnson *et al.* [41]. In this approach the attractive molecular forces are introduced in an indirect way. It is postulated that the contact is able to sustain a tensile pressure distribution at the contact area without breaking. *They neglected the molecular forces outside the contact circle*. They proposed this negative pressure to be of the form  $p'(r) = -p'_0[1 - (r^2/a^2)]^{-(1/2)}$  [30] corresponding to the pressure distribution

of a rigid flat punch. This term is added to the  $p(r)$  given by Hertz theory. They obtained

$$a^3 = \frac{3R}{4E} \left[ P + 3\pi R w + \sqrt{6\pi R w P + (3\pi R w)^2} \right] \quad (44)$$

$$p'_0 = -\left(\frac{2wE}{\pi a}\right)^{1/2}, \quad p_0 = \frac{2Ea}{\pi R} \quad (45)$$

$$\delta = \frac{\pi a}{2E} (p_0 + 2p'_0) = \frac{a^2}{R} - \left(\frac{2\pi w a}{E}\right)^{1/2} \quad (46)$$

$$P = \int_0^a 2\pi r p(r) dr + \int_0^a 2\pi r p'(r) dr \quad (47)$$

$$= \left(\frac{2}{3} p_0^2 + 2p'_0\right) \pi a^2 = \frac{4Ea^3}{3R} - 2(2\pi w E)^{1/2} a^{3/2} \quad (48)$$

$$h^{JKR}(r) = h^H(r) + \left(\frac{2\pi w a}{E}\right)^{1/2} - \left(\frac{8w a}{\pi E}\right)^{1/2} \arcsin\left(\frac{a}{r}\right) \quad (49)$$

For  $a$  to be real in equation (44), the term inside the square root has to be positive. Then the least admissible value for  $P$  is  $P = -3\pi w R/2$ . This value is also the minimum value of  $P$  as a function of  $a$  and gives the pull-off force necessary to detach the bodies.

$$F_a = \frac{3}{2} \pi w R \quad (50)$$

For this value of  $P$  the radius of detachment is finite and given by

$$a_{po} = \left(\frac{9\pi w R^2}{8E}\right)^{1/3} \quad (51)$$

If we control the relative displacement, equation (46), instead of controlling the load, the adhesive contact breaks at

$$F_a = \frac{5}{6} \pi w R \quad a_{po} = \left(\frac{\pi w R^2}{8E}\right)^{1/3} \quad (52)$$

**5.1.3. Adhesive elastic contact: general solution.** The pull-off force given by equation (50) is independent of the Young's moduli and the Poisson ratios of the contacting particles, and it differs from the pull-off force given by the DMT theory (43). This discrepancy is due to the different deformed profiles. In DMT the deformed profile is assumed to be given by the Hertzian solution. In the JKR theory the tensile stresses go to infinity, and inevitably a region of plasticity will develop near the contact circle, implying the existence of a neck of finite height, as shown in the inset of figure 8b.

Tabor was the first to notice these features, and to predict, on dimensional considerations, the existence of this neck in the JKR model [42]. Assuming that

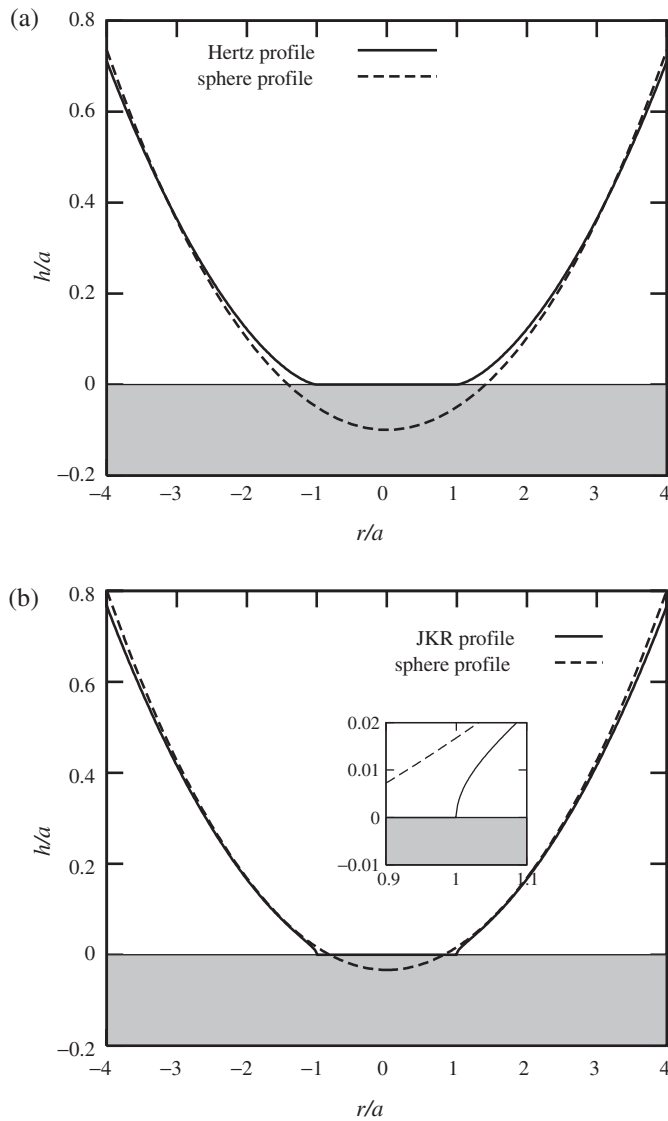


Figure 8. Profile of a deformable sphere pressed against a rigid flat: (a) Hertz profile; (b) JKR profile. The inset is a zoom of the profile of the body at the border of the contact circle.

outside the contacting area the sphere is almost undeformed, the height of the neck,  $h$ , will be of order  $h \sim a^2/R$  and from equation (51) we have

$$h \sim \left( \frac{w^2 R}{E^2} \right)^{1/3} \quad (53)$$

When this height exceeds the range of action of molecular forces, i.e.  $h \gg z_0$  the JKR theory applies; if on the contrary the neck is of negligible height the

DMT theory applies. Therefore, the non-dimensional parameter,

$$\mu = \left( \frac{w^2 R}{E^2 z_0^3} \right)^{1/3}$$

called the Tabor parameter [42], governs this transition.

This parameter  $\mu$  appears naturally in the problem when we assume that the Lennard–Jones potential defines the interaction between the atoms or molecules of the two bodies. In the Derjaguin approximation this pressure is assumed to be equal to the pressure between two half-spaces separated by the same distance as the sphere and the plane. Taking pressure as positive if compressive, then  $p(r) = -F(z(r))$ , with  $F(z)$  given by equation (11). Expressing the displacement as a function of the gap, and using dimensionless variables in equation (32) we have to solve the integral equation

$$\hat{h}(\hat{r}) + \hat{\delta} - \frac{1}{2}\hat{r}^2 = \frac{32\mu^{3/2}}{3\pi} \int_0^\infty \left( \frac{1}{[\hat{h}(\hat{r}') + 1]^9} - \frac{1}{[\hat{h}(\hat{r}') + 1]^3} \right) \frac{\hat{r}'}{\hat{r}' + \hat{r}} K \left( \frac{2\sqrt{\hat{r}\hat{r}'}}{\hat{r}' + \hat{r}} \right) d\hat{r}' \quad (54)$$

with  $\hat{h} = h/z_0 - 1$ ,  $\hat{\delta} = \delta/z_0$ ,  $\hat{r} = r/\sqrt{z_0 R}$ ,  $\hat{r}' = r'/\sqrt{z_0 R}$  and  $\mu = [Rw^2/E^2 z_0^3]^{1/3}$ , the Tabor parameter.

Given  $\delta$  it is possible to solve numerically for  $h(r)$ . For those values of  $h$  less than  $z_0$  the pressure is compressive and it is tensile for  $h(r) > z_0$ . Once  $h(r)$  is known we can calculate “*a posteriori*” the external load, which is given by

$$\hat{P} = \frac{8}{3} \int_0^\infty \left( \frac{1}{[\hat{h}(\hat{r}) + 1]^9} - \frac{1}{[\hat{h}(\hat{r}) + 1]^3} \right) \hat{r} d\hat{r} \quad (55)$$

with  $\hat{P} = P/2\pi R w$ . In this way it is possible to relate the load to vertical displacement. However, it is not obvious how to define the area of the contact region as the gap between bodies is always different from zero. If we define the contact area as where there is a compressive pressure, i.e. all points for which is  $h(r) < z_0$ , the area we obtain is not consistent with the contact area given by the JKR model for large  $\mu$ . An alternative definition will be to define the edge of the contact area as the circle at which the tensile stress takes the maximum value to be in accordance with the JKR model. It is clear that a rigorous definition of the contact area will always be disputable.

Muller *et al.* [43] were the first to perform a numerical solution using the Lennard–Jones potential and showed that the Tabor parameter governed this transition, thereafter called the MYD transition. After that several papers have dealt with this transition, often resorting to numerical solutions [44, 45].

On the theoretical side, Maugis [46] extended the analytical solutions of DMT and JKR to include a constant adhesion potential between both particles outside their contact area. More precisely he states that there exists an attractive constant force of magnitude  $p'_0$  for separations  $z_0 \leq h(r) \leq h_0$ . The parameter  $h_0$  determines an outer circle of radius  $c$ , and the adhesive forces are constant in the annulus  $a < r < c$ .

In the Derjaguin approximation the work of adhesion is given by

$$w = \int_{z_0}^{\infty} p'(h)dh = p'_0 h_0$$

and we are left with an adjustable parameter. These solutions were generalized by Barthel [26] to several attractive interaction potentials excluding the repulsive part.

In Maugis models and their generalizations the profile outside the contact zone is given by elliptic integrals, and the problem needs a numerical solution. Greenwood and Johnson [47] introduced a quite simple model, which they called the “double-Hertz model”, which allowed them to obtain analytical expressions. Their idea was to assume that we have a compressive pressure acting in the contact area given by Hertz theory,  $p(r) = (2E/\pi R)(a^2 - r^2)^{1/2}$ , and that the tensile stresses are given by the difference of two Hertzian pressure distributions,

$$p'(r) = -k \frac{2E}{\pi R} [(c^2 - r^2)^{1/2} H(c - r) - (a^2 - r^2)^{1/2} H(a - r)] \tag{56}$$

with  $H(x)$  the Heaviside function ( $H(x) = 0$  if  $x < 0$ , and  $H(x) = 1$  if  $x > 0$ ).

For  $a \leq r \leq c$ , only the first term of equation (56) is defined, and it represents the tensile stresses outside the contact area is

$$w = \int_a^c p'(r) \frac{dh}{dr} dr = k(k + 1) \frac{2E}{3\pi R^2} (c - a)^2 (c + 2a) \tag{57}$$

The maximum of adhesive stresses,  $p'_0 = (2kE/\pi R)(c^2 - a^2)^{0.5}$ , takes place at  $r = a$ , where also  $p'_0 = 1.02w/z_0 \simeq w/z_0$ . Therefore, the Tabor parameter is expressed by

$$\mu = p'_0 \left( \frac{R}{wE^2} \right)^{1/3} \tag{58}$$

Putting  $c = \beta c^*$ ,  $a = \beta a^*$ ,  $\delta = (\beta^2/R)\delta^*$ , and  $P = 2\pi R w P^*$  with  $\beta^3 = R^2 w/E$ , equations for the load, the indentation, and equations (57), (58) become, in non-dimensionless form

$$P^* = \frac{2}{3\pi} [a^{*3} - k(c^{*2} - a^{*2})] \quad \delta^* = a^{*2} - k(c^{*2} - a^{*2}) \tag{59}$$

$$1 = \frac{2}{3\pi} k(k + 1)(c^* - a^*)^2 (c^* + 2a^*) \tag{60}$$

$$\mu = \frac{2}{\pi} k(c^{*2} - a^{*2})^{(1/2)} \tag{61}$$

Eliminating  $k$  between the last two equations we have

$$\mu \left[ (c^{*2} - a^{*2})^{(1/2)} + \pi\mu/2 \right] (c^* - a^*)^2 (c^* + 2a^*) = 3(c^* + a^*) \tag{62}$$

For given values of  $\mu$  and  $a^*$  we determine  $c^*$  from the last equation. Then  $k$  is determined from equation (61), which allows us in turn to determine  $W^*$  and  $\delta^*$  from equations (60). In this way we may compute the whole curve  $P = P(a)$  and  $\delta = \delta(a)$ , which enables us to determine the pull-off force for fixed loads or at fixed grips, as shown in figure 9.

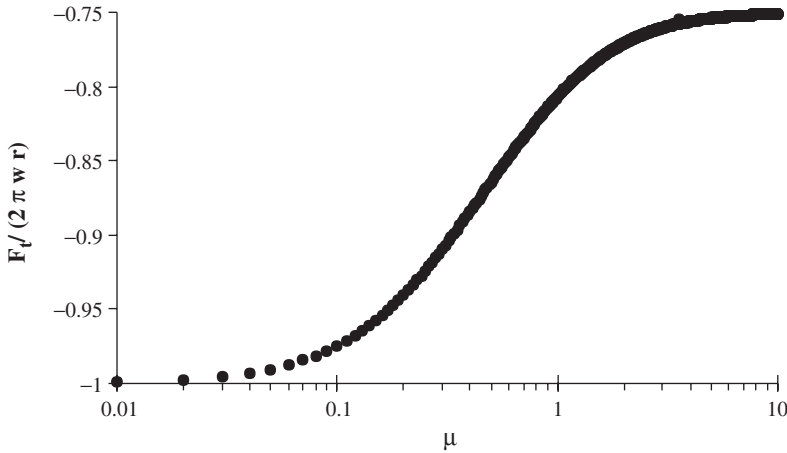


Figure 9. Adhesion force between a spherical particle and a plane as a function of the Tabor parameter (Greenwood–Johnson model).

**5.2. Indentation of elastic–ideally plastic materials: elastic–plastic and fully plastic contact**

Elastic solutions remain valid until the applied load is sufficiently large so as to initiate plastic deformation. The von Mises criterion states that yielding occurs at a point of the body at which

$$J_2 = \frac{1}{6}[(\sigma_1 - \sigma_2)^2 + (\sigma_2 - \sigma_3)^2 + (\sigma_3 - \sigma_1)^2] = k^2 = \frac{Y^2}{3} \tag{63}$$

where  $\sigma_1, \sigma_2, \sigma_3$  are the principal stresses and  $k, Y$  denote the yield stress in simple shear and simple compression (in tension the yield stress may be slightly different).

Another criterion, the Tresca criterion, states that the plastic deformation begins when the maximum shear stress reaches the yield stress  $Y$ , i.e.

$$\max[|\sigma_1 - \sigma_2|, |\sigma_2 - \sigma_3|, |\sigma_3 - \sigma_1|] = 2k = Y \tag{64}$$

For pure shear the von Mises criterion predicts yielding at a stress 15.5 per cent higher than that does the Tresca criterion.

A third criterion, called the maximum reduced stress criterion, is expressed as

$$\max[|\sigma_1 - \sigma|, |\sigma_2 - \sigma|, |\sigma_3 - \sigma|] = k = \frac{Y}{3} \tag{65}$$

where  $\sigma = (\sigma_1 + \sigma_2 + \sigma_3)/3$ .

The difference in the predicted values of yielding is hardly significant when we take into account the variance in the value of  $Y$ . Therefore, and in what follows, we take for our materials the von Mises criterion to define the onset of yielding.

**5.2.1. Non-adhesive elastic–plastic contact.** Let us consider the non-adhesive contact outside the linear elastic regime.

**Onset of plasticity:** For elastic solids in Hertzian contact the stresses in the volume are known [30]. The maximum shear stress,  $\max |\sigma_r - \sigma_z|$ , occurs at a point beneath

the surface on the axis of symmetry. Substituting the stresses in the  $z$ -axis in equation (63) we obtain

$$Y = p_0 F_H(\nu, u)$$

$$F_H(\nu, u) = -(1 + \nu) \left[ 1 - u \arctan\left(\frac{1}{u}\right) \right] + \frac{3}{2(1 + u^2)} \quad (66)$$

with  $u = z/a$ . The function  $F_H(\nu, u)$  has a maximum that depends slowly on the Poisson ratio. It follows that the load necessary to initiate plastic flow is [48, 49]

$$P_Y = \frac{\pi^3 K^3(\nu) R^2 Y^3}{6E^2} \quad (67)$$

with  $K(\nu) = 1.271 + 1.148\nu$  and  $Y$  the lowest yield stress of the two spheres. We see that a material with high yield strength and low Young's modulus can carry a high load without yielding. Substituting this value in the Hertz solution we have

$$\delta_Y = \left( \frac{\pi K(\nu) Y}{2E} \right)^2 R, \quad a_Y = \frac{\pi K(\nu) R Y}{2E} \quad (68)$$

The resulting average pressure at the onset of yield is

$$\bar{p}_Y = \frac{P_Y}{\pi a_Y^2} = \frac{4E}{3\pi R} a_Y = \frac{2}{3} K(\nu) Y \quad (69)$$

**Elastic–plastic regime:** As we increase the pressure the plastic zone grows in size. In the first steps it is fully contained within the elastic zone, and the plastic strains are of the same order as the elastic strains in the surrounding elastic material. Eventually the plastic zone reaches the free surface. This is the elastic–plastic regime. A simple model assumes that below the contact area there is a core with a hydrostatic pressure, and outside it the elastic and plastic stresses and strains have radial symmetry and are the same as those existing in a infinite elastic–plastic body which contains a spherical cavity under uniform pressure [30]. This model predicts that the pressure in the elastic–plastic regime increases linearly with  $\ln(Ea/YR)$ , in agreement with the experiments. According to the Johnson model (see [50]) we assume that the average pressure in the elastic–plastic regime follows the law

$$\frac{\bar{p}}{\bar{p}_Y} = 1 + \frac{2Y}{3\bar{p}_Y} \ln \frac{a}{a_Y} = 1 + \frac{1}{K(\nu)} \ln \frac{a}{a_Y} \quad (70)$$

**Fully plastic regime:** When the plastic zone on the surface comprises the whole contact area we are in the fully plastic regime. At the onset of fully plastic indentation is  $\bar{p}_m = H \simeq 2.8Y$ , and consequently  $a_p/a_Y = \exp[(3H/2Y) - K]$ . For  $\nu = 1/3$ ,  $a_p/a_Y = 12.76$ . According to Stronge [50] the indentation during the elastic–plastic regime is given approximately by  $\delta/\delta_Y = 0.5[(a/a_Y)^2 + 1]$ . This gives  $\delta_p/\delta_Y = 81.9$  at the onset of full plasticity. The formula given by Stronge is obtained by using linear interpolation from the value of indentation at the onset of yielding, and the value of indentation at fully plastic contact. The latter is assumed to be given by  $a_p^2/2R$  neglecting the change in geometry due to plastic flow.

**Finite element computations:** According to finite element computations [51–55] when the plastically deformed zone reaches the circle of the contact area, the

mean pressure becomes a maximum (onset of full plasticity). For the indentation of an elastic sphere in a rigid plane the onset is comprised between 30 and 110 in units of  $YR/E$ , with  $H/Y$  varying between 2.7 and 3.

The plastic indentation can, however, be more complex [52] depending on the value of  $E/Y$ . If the material has a high value of  $E/Y$ , once the onset of full plasticity is reached, the contact area increases in size with the material confined in this zone. The average pressure,  $p_m = P/\pi a^2$ , is independent of the parameter  $(Ea/YR)$ , and is approximately equal to the hardness  $H = 2.8Y$ . This is the fully plastic similarity regime. However, if we continue to increase the load, and therefore the area of contact, it happens that at a given radius the plastic material overflows outside the contact zone and the pressure decreases. We have entered into the finite deformation mode. In this regime the approximations of contact mechanics cease to be valid and we must consider each separate case. Now  $E/Y$  and  $a/R$  are both needed to describe the elastic–plastic indentation, and the radius varies depending on  $E/Y$ .

For lower values of the parameter  $E/Y$  the similarity zone decreases, until it disappears, entering into the finite deformation regime. For even lower values the maximum pressure is below  $H$ , and the finite deformation regime follows the elastic–plastic regime directly. In general, the area of contact and the value of  $p_m/Y$  depends on the geometry of the bodies at contact, and on the value of  $E/Y$ , and it can be determined exactly only after extensive numerical computations. Therefore, the hardness is not a material constant. Nevertheless, in the linear fit between  $\bar{p}_m/\bar{p}_Y$  and the logarithm of  $(Ea/YR)$ , the slope is almost independent of the value of  $E/Y$ .

For the case of indentation of an elastic sphere in a rigid flat, Kogut and Etsion [55] give analytical relations for the variation of pressure, load, area of contact, indentation and evolution of the plastic zone in the elastic and elastic–plastic regime of the deformed sphere by fitting the results of extensive numerical calculations. They consider that the fully plastic regime is attained for an indentation of 110 times the critical indentation for plastic yield.

We must bear in mind that in these computations the assumptions of contact mechanics do not necessarily always hold.

**Thornton approximate model for the non-adhesive elastic–plastic regime:** The numerical results for the elastic–plastic indentation show that in the contact radius the pressure is  $H$  in the plastic zone and goes from this value to zero in the elastic zone. Following a suggestion by Thornton and Ning [56] it is convenient to approximate the pressure in the elastic zone by the Hertz solution. Under this approximation it is quite simple to calculate the relation  $a = a(P)$  for loading. We obtain this relation in the following way.

Given a contact area of radius  $a$ , then  $p(r) = p_0(a^2 - r^2)^{1/2}$  with  $p_0 = 2E/\pi R$ . If  $p_0 a \leq H$  the contact is elastic and the relation between  $a$  and  $P$  is given by the Hertz solution. If, on the contrary,  $p_0 a > H$ , we define  $a_p$  by  $p(a_p) = H$ . This gives  $a_p^2 = a^2 - H/p_0$ . Then the new load  $P$  is

$$P = \pi a_p^2 H + p_0 \int_{a_p}^a 2\pi r \sqrt{a^2 - r^2} dr \quad (71)$$

which gives us  $P = P(a)$ . This simple model agrees fairly well with the numerical computations.

An improved semi-analytical model that takes into account the transition region for  $p_m$  between  $p_m = 1.1 Y$  (onset of plastic yield) and  $p_m = 2.8 Y$  is described in [57].

**5.2.2. Adhesive elastic–plastic contact.** We now review the results from the onset of plasticity to the fully plastic contact.

**Onset of plasticity:** Barquins *et al.* [58] have shown that the stress tensor for adhesive contacts can be obtained by superposition of a Hertzian stress tensor and the stress tensor of a rigid flat punch (Boussinesq solution). The onset of plastic deformation is determined by solving numerically for the von Mises criterion, which is given by

$$Y = p_0 F_{JKR}(u, \nu) = p_0 F_H(u, \nu) - p'_0 F_B(u, \nu)$$

$$F_B(u, \nu) = \frac{1}{1 + u^2} \left[ \frac{9}{2} \frac{u^2}{1 + u^2} \left( 1 + \frac{1}{3u^2} \right) - (1 + \nu) \right] \tag{72}$$

The values of  $p_0$  (equation (39)) and  $p'_0$  (equation (45)) depend on the contact area  $a$  (equation (44)) and consequently on the load  $P$  and work of adhesion  $w$ . For this reason the onset of plastic deformation, given by the maximum value of the function  $F_{JKR}$  for fixed  $\nu$ , depends not only on Poisson’s coefficient but also on the load and work of adhesion.

For  $P = 0$  is

$$a = \left( \frac{9\pi w R^2}{2E} \right)^{1/3}, \tag{73}$$

then  $p'_0 = (1/3)p_0$ , and

$$Y = p_0 \left( F_H - \frac{1}{3} F_B \right) \tag{74}$$

Plastic deformation at zero load will take place for spheres satisfying that

$$R_Y^{JKR} \leq \frac{36 M_0^3}{\pi^2} \left( \frac{w E^2}{Y^3} \right) \tag{75}$$

with  $M_0$  the maximum of the function  $F_H - (1/3)F_B$ . For  $\nu = 1/3$ ,  $M_0 = 0.432$  (with  $u = 0.348$ ), and for  $\nu = 1/4$ ,  $M_0 = 0.455$  (width  $u = 0.33$ ).

In the case of arbitrary loads,  $P$ , Maugis and Pollock [8] give the following approximate equation for the determination of the onset of plastic flow for  $\nu = 1/3$ ,

$$P + \frac{3}{2} \sqrt{2\pi w E a_Y^3} = 1.1 \pi a_Y^2 Y \tag{76}$$

which allows us to determine the onset within 12 per cent error. Here  $P$  is the applied load, and  $a_Y$  is the radius of contact at onset.

To estimate the onset of plastic flow for arbitrary values of  $\mu$  we might use the stresses in the body given by the Greenwood and Johnson model [47]. In the DMT case, for which  $\mu \ll 1$ , it may be reasonable to assume that stresses are

approximately given by the Hertz stresses. In this case the onset of plasticity will be take place if  $2\pi wR \geq P_Y$  as given by (67), that is

$$R_Y^{DMT} \leq \frac{12wE^2}{\pi^2 K^3 Y^3} \quad (77)$$

**Fully plastic contact:** In the case of full plasticity Roy Chowdhury *et al.* [59] used a simple argument to determine the role played by the attractive surface forces, which we reproduce here given its simplicity and interest. Let  $\delta_p$  be the flattening of a perfectly plastic sphere pressed against a rigid plane under load  $P$ . Then, the work done by the load is

$$U_P = -P\delta_p \quad (78)$$

If we neglect the change in contact geometry due to plastic flow, the radius of the area of contact  $a_p$  is related to the deformation  $\delta_p$  by  $a_p^2 \simeq 2R\delta_p$  (this estimation was also used by Stronge [50] for the elastic–plastic and fully plastic regime). Therefore, the energy irreversibly absorbed in the deformation is

$$U_D = \int_0^{\delta_p} \pi a_p^2 H d\delta_p = \pi R H \delta_p^2 \quad (79)$$

Neglecting the contribution of attractive forces outside the contact area, the work of adhesion is

$$U_S = -\pi a_p^2 w \quad (80)$$

which gives a total energy  $U_T = U_P + U_D + U_S$ . From the equilibrium condition  $\partial U_T / \partial \delta_p = 0$  we obtain

$$P + 2\pi R w = \pi a_p^2 H \quad (81)$$

**Elastic–plastic regime:** Based on these considerations Maugis *et al.* [8] proposed to substitute for the adhesive contact the load  $P$  in the Hertzian contact by  $P + 2\pi R w$ . Thus, relation (70) should be replaced by

$$\frac{\bar{p}_m}{\bar{p}_Y} = \frac{P + 2\pi w R}{\pi a^2 \bar{p}_Y} = 1 + \frac{2Y}{3\bar{p}_Y} \ln \frac{a}{a_Y} \quad (82)$$

They proposed a slightly different expression for the constant affecting the logarithm, as they assumed full plasticity is reached at a critical radius of  $a_p \simeq 60(RY/E)$ .

Kogut and Etsion [60] have extended the numerical analysis of the DMT model to the elastic–plastic regime. They give expressions for the adhesive force, the profile, radius and indentation for nanocontacts and microcontacts as a function of  $z_0/\delta_c$  and  $\delta/\delta_c$  with  $\delta_c$  the value at the onset of indentation given by Hertz theory.

### 5.3. Unloading the adhesive contact of elastic–ideally plastic materials

To find the pull-off force as a function of the load it is assumed that: (a) on unloading the deformation is predominantly elastic; (b) the radius of contact is small enough for the approximations of contact mechanics to be valid; and (c) the net pressure and net load is the sum of compressive and adhesive forces. Let us consider first the case of fully plastic contact.

**5.3.1. Fully-plastic contact.** The compressive pressure is approximated by a uniform pressure over the contact area, and therefore the evolving pressure on unloading is given by the elastic recovery of a circular area subject to a constant pressure. If  $a_0$  is the final contact area after indentation the solution is known and it is given by [61],

$$\frac{P_1}{p_0\pi a_0^2} = \frac{2}{\pi} \left[ \arcsin\left(\frac{a}{a_0}\right) - \frac{a}{a_0} \sqrt{1 - \left(\frac{a}{a_0}\right)^2} \right] \quad (83)$$

where  $p_0$  is the constant pressure in the initial contact area  $a_0$  on unloading, and  $a$  is the actual contact area. For a fully plastic indentation,  $p_0 = H$ . If the adhesive forces act only in the area of contact the adhesive traction is the same as the traction in the JKR model [62]. Therefore, we have

$$P = P_1 + P_2 = 2p_0 a_0^2 \left[ \arcsin\left(\frac{a}{a_0}\right) - \frac{a}{a_0} \sqrt{1 - \left(\frac{a}{a_0}\right)^2} \right] - \sqrt{8\pi w E a^3} \quad (84)$$

Differentiating this expression and equating it to zero, will give us the pull-off force and the radius of contact at breaking.

For the limiting case,  $a_{p0} \ll a_0$ , the value of the pull-off force is given by

$$F_a = \left( \frac{9\pi}{4H^3} \right)^{1/2} w E \sqrt{P} \quad (85)$$

Johnson has given an approximate solution to this problem of fully plastic contact with elastic recovery, under two very simple assumptions. First, he estimated the radius of the recovered sphere from the Hertz relation  $R' = 4E/3Pa_0^3$ , and eliminating  $a_0$  from the relation  $H\pi a_0^2 = P$ , he obtained  $R' = 4EP^{1/2}/3(\pi H)^{3/2}$ . Secondly, putting this value of  $R'$  in the JKR solution for the pull-off force, he obtained  $F_a = 2wEP^{1/2}/(\pi H^3)^{1/2}$  which is  $4/3\pi$  times smaller than the asymptotic expression given above.

When the adhesive forces also act outside the contact, Johnson *et al.* used the Maugis model [46] to compute the pull-off force. They deduced that in this case the ratio of the pull-off force to the one given by equation (85) lies between 0.84 and 1.14. Therefore, it is reasonable to use equation (85) to estimate the pull-off force as a function of the load.

This expression has been obtained neglecting the contribution of molecular forces to the indentation, and it will be applicable whenever the external load is much larger than the equivalent Hertzian load of attractive forces. Since, as noticed by Maugis *et al.* [8], we may have fully plastic contact at zero load, as explained above, they suggested replacing  $P$  by  $P + 2\pi R w$  in formula (85), with the result that now is

$$F_a = \left( \frac{9\pi}{4H^3} \right)^{1/2} w E \sqrt{P + 2\pi w R} \quad (86)$$

The numerical factor in this formula does not coincide with the formula given by Maugis and Pollock in [8] which was taken there from the Johnson simplified model discussed above. We call this corrected formula the modified Maugis–Pollock

formula. We may have partial plastic flow with partial elastic recovery, and in this case we are in between ductile and brittle breaking (unloading purely elastic). Mesarovic *et al.* [62] and Maugis *et al.* [8] discuss the adhesion map for various cases.

#### 5.4. The effect of asperities

It is well known that asperities affect in an essential way the forces between particles, due to modification of the true area of contact [32, 63]. Measurements of forces between particles of different sizes and similar topographies give similar pull-off forces [2, 33, 64–66]. Because of that, great experimental effort has been directed to determine the surface topography of particles. The magnitude that is directly available using the scanning electron microscope (SFM) is the profile. From the profile we obtain the roughness parameters:  $R_a$ , the arithmetic mean of the departures of the rough profile from the mean line;  $R_{rms}$ , the root mean square deviation of the asperity height distribution;  $R_{pv}$ , the average peak-to-valley ratio, and  $\xi$ , the distance at which two heights become uncorrelated.

In order to determine the most relevant profile magnitudes that govern interparticle forces a model of the profile is needed. In the pioneering work of Greenwood and Williamson [67], the surface is modelled as consisting of spherical caps with the same radius  $R$  but with different heights. The distribution of heights could be either Gaussian or exponential. The stress field in each spherical cap is assumed to be unaffected by the stress field of neighbours caps (non-interacting asperities). Application of this model to particle adhesion proved to be difficult as there was no definite cut-off for the scale of roughness below which the asperities would be flattened plastically [30]. This model was later generalized to a statistical distribution of radii of curvature and heights, and to different probability distributions.

More recently, models based on fractal surface geometries with interacting and non-interacting asperities have been developed. An important consequence of these studies is that purely elastic multiasperity contacts give rise to a dependence of pull-off force on the load as several asperities may enter in contact as we increase the load (though the contribution of each asperity is independent of the load). For a review on both stochastic and fractal models and its application to interparticle forces we refer the reader to [68]. In a recent book Goryacheva [69] examines in depth the role of simultaneous contact at several interacting asperities in the adhesive elastic contact, both in the DMT and JKR limits, and for van der Waals and capillary forces. Clearly, the rigorous study of the contact problem for particles with rough surfaces is of great complexity, and there is a need for simpler asperity contact models.

A model with contact through only one smooth asperity of given size was developed by Rumpf [70]. This size has to be determined assuming that asperities have a local radius of curvature at the contacting point, and through averaging of these radii like in [2]. Recently Chow [71] deduced an average radius of curvature from the general properties of fractal surfaces. Cooper [72] extended the Rumpf model to include the possibility of multiple smooth asperity contacts. Rabinovich [73, 74] in another extension considered the Rumpf model to include a second level of asperities on the larger asperities. In addition, fractal models recognize that the surfaces may be self-similar to all scales from Å up to the size of the particle.

Instead of a continuous hierarchy with all length scales as in fractal models, we may consider (in the spirit of the simpler models discussed above) a grouping of scales from the molecular level to 1 nm, 10 nm, 100 nm, 1  $\mu$ m, up to the size of the particle. As a further simplification we may assume that asperities are locally spherical of radius  $R_1$  and separation between maxima  $l_1$ , which have asperities of a smaller radius  $R_2 = R_1/10$  with separation distance  $l_2 = l_1/10$ , which in turn have smaller asperities of radius of radius  $R_3/ = R_2/10$  and separation distance  $l_3 = l_2/10$ , and so on up to the molecular level. These models are oversimplified but they may work for particles that have no cusps, ridges or other singularities. From the experimental measurements of surface topography for particles with diameters of the order of 10 microns [2], and the connection between roughness with radii of curvature and the correlation length, we assume that the relevant radius for our asperities is of the order of 0.1  $\mu$ m with typical separation between two nearest summits of 0.4  $\mu$ m. The second level of asperities, which is of the order of 10 nm, is likely to be flattened plastically as will be shown in the next section. Because van der Waals forces have an effective range less than 10 nm [24], when an asperity of radius 0.1  $\mu$ m touches the other particle asperity the interaction takes place solely between the asperities. Therefore, and in what follows, the interparticle force between particles is in our case postulated to be governed by asperities with radius 0.1  $\mu$ m. A further simplification is to assume that stresses do not extend beyond the asperity and that contact takes place through only one asperity. Consequently, to estimate the contact forces between our toner particles we take a reduced radius  $R = 0.05 \mu\text{m}$  for all formulae of this section. Because surface roughness can have such a large effect on the adhesion force, errors introduced by modelling surface roughness in this way imply that our adhesion force predictions will be inaccurate to some extent and will have a large statistical dispersion. However, they allow for a physical interpretation of the measurements. More importantly, we can understand the relevant physical parameters that govern particle–particle interaction, i.e. surface energy, particle size, surface roughness, Young’s modulus, and hardness, which are crucial in the design of fine cohesive powders.

## 6. Normal forces between two powder particles: AFM measurements

The atomic force microscope (AFM) allows us to measure directly forces between two particles or between a particle and a substrate. Since its invention [75] in 1986, it has become the standard tool to measure surface topographies and particle interactions [76]. A sketch of the AFM used for measuring the adhesion force between two individual grains is shown in figure 10.

The probe particle is attached at the end of a V shaped cantilever according to the following procedure. Several particles are spread over a flat substrate. With the aid of an optical microscope we choose an isolated particle and the cantilever is brought slowly close to it. At a certain small separation, the particle jumps towards the cantilever and remains attached to it due to the adhesive forces between the powder particle and the cantilever. Although these forces are strong enough to keep the particle attached to the cantilever, they cannot prevent the probe particle from being removed if we make an indentation experiment with a substrate particle.

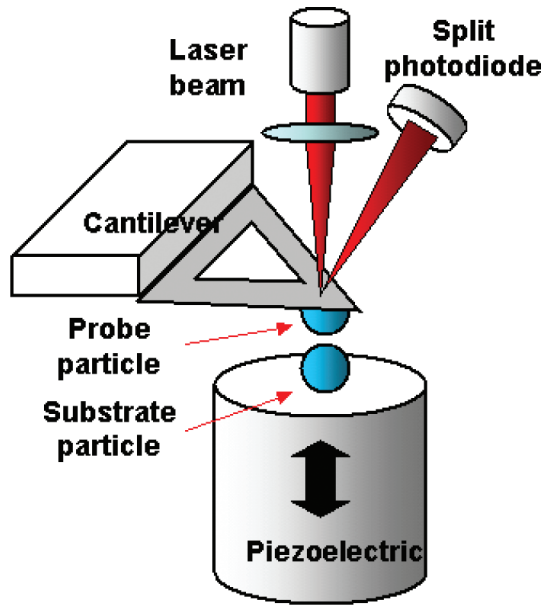


Figure 10. Sketch of the AFM.

In order to keep the probe particle permanently attached to the cantilever, the piece holding the cantilever with the particle on it is heated to sinter the contacts between particle and cantilever, controlling the temperature to avoid melting the particle or changing its shape. We have preferred this method to the use of adhesive to glue the particle to the cantilever in order to avoid its possible spreading on the surface of the particle. Each time, we have taken the particle in the cantilever to the AFM to be sure that this blocking temperature has not deformed the particle. The substrate particles are spread over a piece of transparent film and fixed to it permanently by heating them in the same way. The probe particle is brought close to an isolated substrate particle on the film under computer control. The computer detects the movement on the cantilever and stops the approach when the cantilever starts to bend. We place the probe particle very close to the substrate particle, but avoiding contact between them. The substrate particle is then retracted slightly, moved vertically by means of the AFM piezoelectric tube. At the beginning of a loading–unloading curve (see figure 11), both particles are apart (point A). The substrate particle is moved upwards till it makes contact with the probe particle (point B) and is pushed until a certain cantilever deflection is achieved (point C). Upward deflection of the cantilever means a positive load force. After that, the substrate particle is slowly withdrawn. Both particles remain in contact causing the cantilever to bend downwards (negative load force or tensile force), until the substrate particle is detached (point D). The largest downward deflection achieved by the cantilever gives the adhesion force. The piezoelectric extension and the current given by the split photodiode are recorded. The piezoelectric extension is transformed in nano-newtons assuming that both particles remain in contact while the piezoelectric is

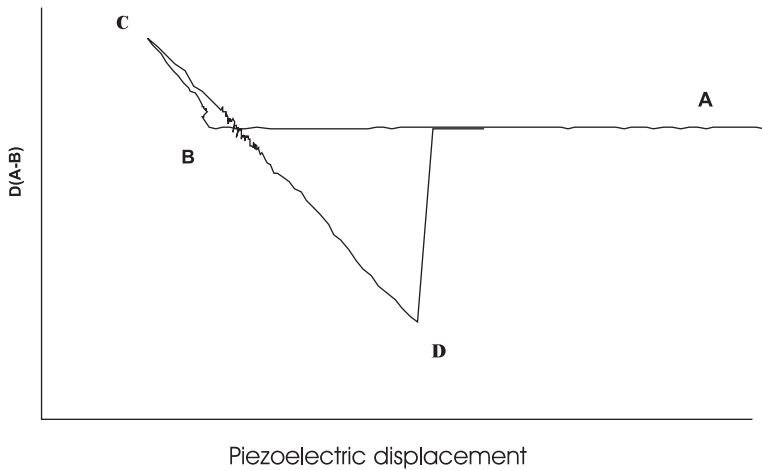


Figure 11. Loading–unloading curve.

retracting until the ‘substrate’ particle is detached. Neglecting particle deformation (at the level of the whole grain) in the indentation process we obtain a proportionality constant that relates the piezoelectric displacement and cantilever displacement, and from it and the spring constant of the cantilever the force exerted between the particle and the substrate is derived.

**Materials:** We have run the AFM experiments with xerographic toners based either on styrene–butadiene (TA toners) or polyester (TB toners). These toner particles are produced by an attrition process thus having an irregular shape. Attrition is followed by size classification using a cyclone separator apparatus. Aerodynamic classification produces a narrow toner particle size distribution, thus they are rather monodisperse. The toners are blended with a flow control additive consisting of fumed silica nanoparticles, which coat the polymer particle surface (fumed silica has been treated with hexamethyldisilazane, rendering the silica extremely hydrophobic). Admittedly, these model materials are quite specific, but their main advantage is that they are very well characterized. The know-how of Xerox is used to vary surface energy, average particle size, roughness through the use of nanoparticle coating, and their mechanical properties, Young modulus and hardness by changing the base polymer material, or for the same polymer by cross-linking. The study of the effect of a single parameter is possible, both in the AFM and in bulk behaviour, thus enabling us to test the general theories of interparticle contact mechanics.

TA toners are identical in particle resin type (styrene-butadiene), pigment concentration, average particle volume diameter ( $d_p = 12.7\mu\text{m}$ ), and particle density  $\rho_p = 1.117\text{ g/cm}^3$  (see figure 12). The mechanical properties of the copolymer styrene–butadiene (a thermoplastic resin) are Young’s modulus  $E_{TA} = 3.5\text{ GPa}$ , Poisson’s coefficient  $\nu_{TA} = 1/3$ , and tensile yield strength  $Y_{TA} = 100\text{ MPa}$ . The work of adhesion  $w$  for polymers is within the interval  $(0.01\text{--}0.1)\text{J/m}^2$ . In our case we take  $w = 0.07\text{ J/m}^2$  [77]. TA powders differ only in the quantity of flow controlling additive (Aerosil R812 from Degussa, silica particles of density

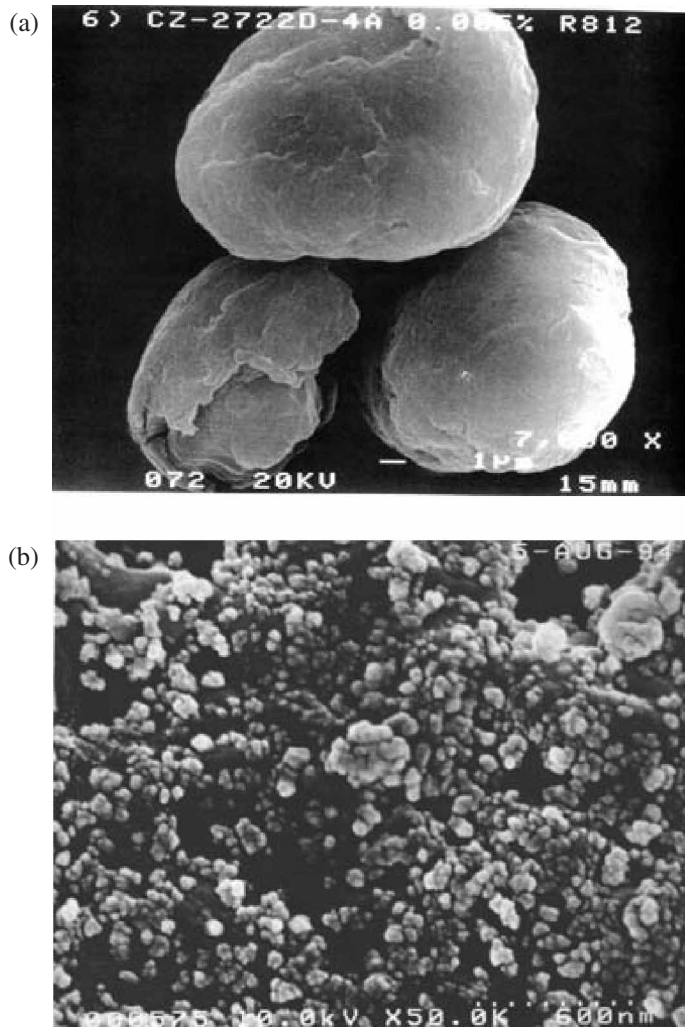


Figure 12. (a) Toner TA005 made of styrene-butadiene with 0.05 per cent in weight of flow additive (aerosil); (b) Detail of the surface of toner particle TA04. Agglomerates on the surface are also made of Aerosil particles.

$\rho_s = 2.56 \text{ g/cm}^3$  and nominal diameter 7 nm). From scanning electron microscopy (SEM) pictures of the toner particles (see figure 12a), we have observed that additive particles are distributed in agglomerates that are randomly placed on the powder surface. These agglomerates have estimated diameters ranging from 40 to 60 nm. In table 1 we present their properties (for explanation of the last two columns see the following section).

The second set of toners, which we call TB toners, is based on resin polyester with no pigment, and particle density  $\rho_p = 1.25 \text{ g/cm}^3$ . The mechanical properties of the polymer polyester are Young's modulus  $E_{TB} = 3.5 \text{ GPa}$ , Poisson's coefficient

Table 1. TA toners. Particle density  $\rho_p = 1.117 \text{ g/cm}^3$ ; average volume particle diameter  $d_p = 12.7 \mu\text{m}$ ; diameter of additive particles  $d_s = 7 \text{ nm}$ ; diameter of additive particles aggregate  $d_a = 50 \text{ nm}$ ; Young's modulus  $3.5 \text{ GPa}$ ; Poisson coefficient  $\nu = 1/3$ ; tensile yield strength  $Y_{TA} = 100 \text{ MPa}$ ; surface energy  $w = 0.07 \text{ J/m}^2$ ; % weight: % in weight of the additive relative to toner particle weight;  $\text{SAC}_a$ : surface area coverage of additive aggregates;  $(\text{SAC}_a)_{pp \rightarrow ps} = 2.18\%$ : surface area coverage for transition polymer-polymer to polymer-silica contacts; and  $(\text{SAC}_a)_{ps \rightarrow ss} = \pi/16 \simeq 20\%$  surface area coverage for transition of polymer-silica to silica-silica contacts.

Toner	%w (%)	SAC (%)	$\text{SAC}_a$
TA001	0.01	1.98	0.54
TA005	0.05	9.89	2.77
TA01	0.1	19.8	5.54
TA02	0.2	39.6	11.1
TA04	0.4	79.2	22.1

Table 2. TB toners. Particle density  $\rho_p = 1.25 \text{ g/cm}^3$ ; Young's modulus  $3.5 \text{ GPa}$ ; Poisson coefficient  $\nu = 1/4$ ; tensile yield strength  $Y_{TB} = 50 \text{ MPa}$ ; surface energy  $w = 0.07 \text{ J/m}^2$ ;  $d_p$ : particle diameter in  $\mu\text{m}$ ;  $d_s$ : diameter of additive particles in  $\text{nm}$ ; % gel: % in weight of a gel cross-linking agent; % weight: % in weight of the additive relative to toner particle weight;  $(\text{SAC}_a)_{pp \rightarrow ps} = 2.18\%$  for toners with small additive size, and  $1.78\%$  for with large additive particles;  $(\text{SAC}_a)_{ps \rightarrow ss} = \pi/16 \simeq 20\%$  is the surface area coverage for transition of polymer-silica to silica-silica contacts.  $d_a$ : the diameter of additive particle aggregate is 50 and 200 nm for the smaller and larger additives respectively.

Toner	$d_p$ ( $\mu\text{m}$ )	$d_s$ (nm)	%gel (%)	%weight (%)	SAC (%)	$\text{SAC}_a$ (%)	$(\text{SAC}_a)_{pp \rightarrow ps}$ (%)
TB46	7.03	8	0	0.15	18.7	5.99	2.18
TB47	7.0	8	0	0.75	93.2	29.8	2.18
TB48	6.95	40	0	0.75	18.5	7.40	7.14
TB49	7.03	40	0	3.75	93.6	37.4	7.14
TB50	6.89	8	14.2	0.15	18.4	5.87	2.18
TB51	7.32	8	14.2	0.75	97.5	31.2	2.18
TB52	7.38	40	14.2	0.75	19.7	7.82	7.14
TB53	7.32	40	14.2	3.75	97.5	39	7.14
TB54	7.28	8	28.4	0.15	19.4	6.2	2.18
TB55	7.10	8	28.4	0.75	94.5	30.3	2.18
TB56	6.95	40	28.4	0.75	18.5	7.40	7.14
TB57	6.99	40	28.4	3.75	93.1	37.2	7.14
TB58	7.36	8	45	0.15	19.6	6.27	2.18
TB59	7.47	8	45	0.75	99.5	31.8	2.18
TB60	7.38	40	45	0.75	19.7	7.86	7.14
TB61	7.47	40	45	3.75	99.5	39.8	7.14

$\nu_{TB} = 1/4$ , tensile yield strength  $Y_{TB} = 50 \text{ MPa}$ , and work of adhesion  $w = 0.07 \text{ J/m}^2$ . They have slightly different radii, and their additives are either agglomerates of 50 nm diameter of Cabosil particles of 8 nm (TS350 from Cabot), or agglomerates of the order of 200 nm made of particles of 40 nm (RX50 from Cabot), both of them of density  $\rho_s = 2.2 \text{ g/cm}^3$ . In table 2 we present the properties of TB toners, and in figure 13 SEM images of the toner TB61 are shown.

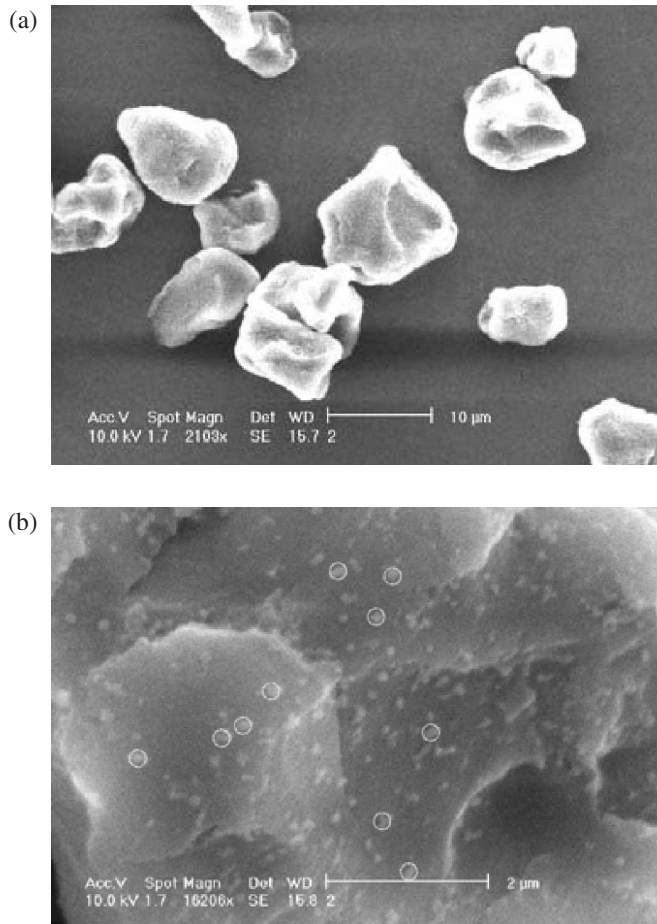


Figure 13. (a) Toner particle TB61 made of polyester with 3.75% in weight of flow additive of 40 nm (aerosil); (b) Agglomerates at surface of TB particles (the circles have a diameter of 0.2 μm).

**AFM experimental results:** The experimental results are presented in figure 14. The data form a cluster with a large dispersion. These points have been ordered by increasing value of the load force and distributed in groups. Each point represents the average value of ten independent measurements in each adhesion group versus the load force.

The strong dispersion in the values of the adhesion is due to several effects: (1) The angle of contact is not controlled, and because the laser light-cantilever-photodiode setup responds to bending and torsion of the cantilever, the output signal is influenced both by normal forces (adhesion) and tangential contact forces (friction, peeling). Thus for a given load force, if tangential forces act in the area of contact, the force of adhesion may diminish; (2) The surface of the particles is not homogeneous: local radius, hardness and Young modulus vary from point to point, (3) Particles can make contact through more than one asperity.

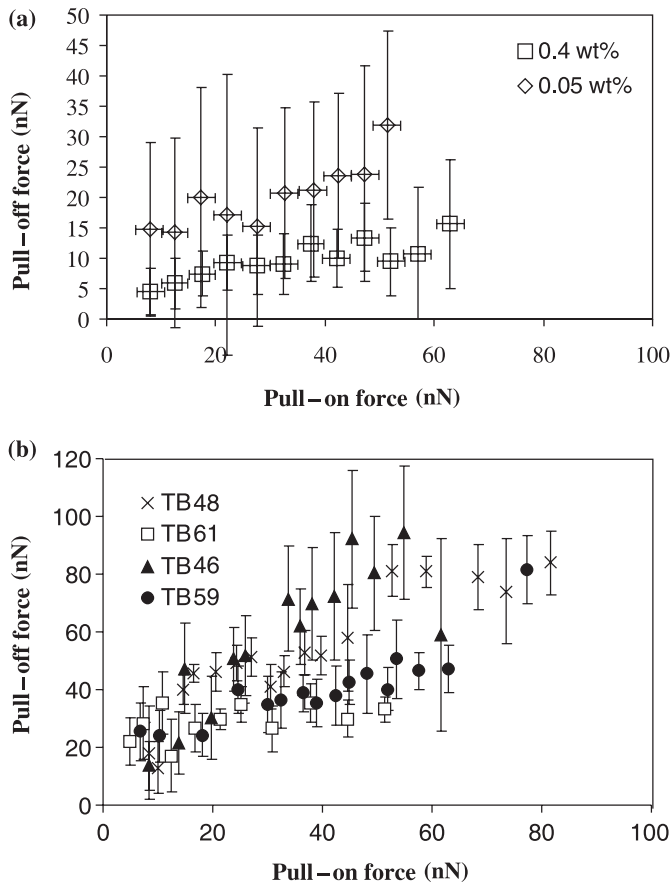


Figure 14. Average value of the pull-off force as a function of the pull-on force: (a) TA toners; (b) TB toners.

## 7. Normal forces: comparison between theory and experiments

This section is dedicated to the application of the previously discussed contact mechanical theories to interpret the AFM experimental results for toners. As is evident from the bibliography cited in section 5.4 similar reasoning has been and is routinely applied to grains made of all kind of materials, going from metallic to uranium oxides and from a few microns to millimetre sized particles (for additional information see in [www.adhesionsociety.org](http://www.adhesionsociety.org) the annual proceedings published by the Adhesion Society and the book by Kendall [29]). The originality of the work presented here is the extension of the modelling to the elastic-plastic regime.

### 7.1. Nature of contact

Prior to any comparison we need firstly to know what type of contacts, polymer-polymer, polymer-silica, silica-silica, predominate, and secondly, if the contact is elastic or plastic.

**7.1.1. Does the contact take place between the base polymer, or through the additives?** We assume that our powder particles and flow additives are spherical, and that additives coat the surface uniformly. Manufacturers know with good precision the percentage of additive weight compared to the toner weight,  $w\%$ . From this value they calculate the percentage of the area of toner surface that is covered by additives,  $SAC$ , assuming that the silica nanoparticles are individually distributed on the toner particle surface. Clearly, the equivalent surface radius is larger than the volume equivalent radius as the particles are irregular and rough. However, in the absence of a precise measurement of the particle surface,  $S_p$ , we follow the usual practice of assuming them equal. In this case there is a well defined relation between  $w\%$  and  $SAC$ . For example, when additives are far from covering the surface with a monolayer, the area of each additive particle is  $\pi(d_s/2)^2$ , and we have

$$w\% = \frac{N_s \rho_s d_s^3}{\rho_p d_p^3}, \quad SAC = \frac{N_s d_s^2}{4d_p^2} \quad (87)$$

with  $N_s$  the total number of additive particles. Consequently

$$SAC = \frac{\rho_p d_p}{4\rho_s d_s} w\% \quad (88)$$

For aggregates, the effective surface area coverage is  $SAC_a = N_a d_a^2 / 4d_p^2$  with  $N_a$  the total number of aggregates.  $N_a \rho_a d_a^3 = N_s \rho_s d_s^3$ , and therefore, the relation between  $SAC$  and  $SAC_a$  is known, once the aggregate solid fraction is known. Aggregates are formed of small cohesive particles, thus their solid fractions may vary from 0.2 to 0.64 depending on the process and the applied consolidation pressure. In our case the additives are formed through a milling process for which the transient consolidation pressures may be high. Thus we take for the aggregates a solid volume fraction  $\phi_a \sim 0.5$ , closer to the packing of noncohesive grains than to the limit of infinitely cohesive aggregates made by ballistic deposition at zero consolidation pressures ( $\phi_a = 0.18$ ). Under this assumption the relation between  $SAC$  and  $SAC_a$  is

$$SAC_a = \frac{2d_s}{d_a} SAC \quad (89)$$

Let us now consider for which values of the %weight of additives the transition from polymer–polymer to polymer–silica contacts takes place. If, on average, adjacent aggregates belong to opposite asperities, the average inter-aggregate distance *on the same toner particle* is  $2d_{ia} = 2\sqrt{2d_{asp}d_a + d_a^2}$  (see figure 15a). The number of aggregates on the toner surface is then  $N_a \simeq \pi d_p^2 / d_{ia}^2$ . The corresponding additive percentage weight should be

$$(w\%)_{pp \rightarrow ps} = \frac{N_a \rho_a d_a^3}{\rho_p d_p^3} \sim \frac{\pi \rho_s d_a^3}{2\rho_p d_p (2d_{ia})^2} = \frac{\pi \rho_s d_a^2}{8\rho_p d_p (2d_{asp} + d_a)} \quad (90)$$

and

$$(SAC_a)_{pp \rightarrow ps} = \frac{N_a d_a^2}{4d_p^2} \sim \frac{\pi d_a^2}{4d_{ia}^2} = \frac{\rho_p d_p}{2\rho_s d_a} (w\%)_{pp \rightarrow ps} \quad (91)$$

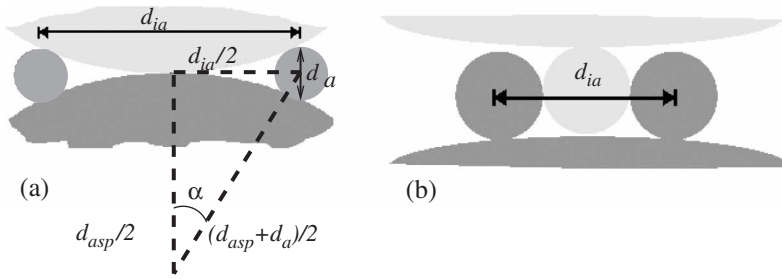


Figure 15. (a) Transition from polymer–polymer to polymer–silica contact; (b) Transition from polymer–silica to silica–silica contact.

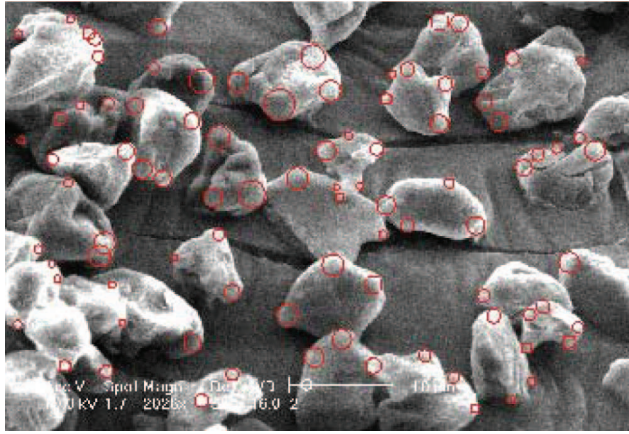


Figure 16. Estimation of visible local radii of curvature for TB toners.

To determine the transition from polymer–silica to silica–silica contacts, we take into account that the effective area occupied by each aggregate is  $(2d_a)^2$  as is evident from figure 15b. The number of aggregates would be  $N_a = \pi d_p^2 / 4d_a^2$ , and we have

$$(w\%)_{ps \rightarrow ss} \simeq \frac{N_a \rho_a d_a^3}{\rho_p d_p^3} \sim \frac{\pi \rho_s d_a}{8 \rho_p d_p}, \quad (SAC_a)_{ps \rightarrow ss} = \frac{\rho_p d_p}{2 \rho_s d_a} (w\%)_{ps \rightarrow ss} = \frac{\pi}{16} \quad (92)$$

For TA and TB toners with small additives we take  $d_{asp} \sim 0.1 \mu\text{m}$ . The size of aggregates for TB toners with 40 nm particles is  $0.2 \mu\text{m}$ , thus larger than  $0.1 \mu\text{m}$ . We then have to go to the next level of local radii of curvature. We have estimated that for this higher level,  $d_{asp} = 1 \mu\text{m}$  (see figure 16).

We present in tables 1 and 2 the results for the different toners. According to these rough estimates we should have polymer–polymer contacts for TA005, and polymer–polymer contacts with a few percentage of polymer–silica contacts for TB46 and TB48. Clearly, for TB59 and TB61 the contacts are between aggregates of silica.

**7.1.2. Is the contact elastic or plastic?** We address the question of whether the contact between polymers is elastic, fully plastic or elastic–plastic. First we have to calculate the value of the Tabor parameter, secondly determine the onset of plastic flow, and finally the onset of full plasticity for the toners under investigation.

**Tabor parameter:** For asperities of reduced radius  $R = 0.05 \mu\text{m}$  the Tabor parameter is  $\mu_{TA} = [Rw^2/E^2z_0^3]^{1/3} = 2$ , a value intermediate between the DMT and the JKR models. For TB toners the Tabor parameter,  $\mu_{TB} = [Rw^2/E^2z_0^3]^{1/3} = 2$  is the same as for TA toners. For asperities ten times larger we have  $\mu_{TB} = 4.45$  close to the JKR limit. However, we must bear in mind that we assume that for polymer–polymer contacts the reduced local radius is  $0.05 \mu\text{m}$  for both TB toners.

Let us examine if the contact is purely elastic or plastic.

**Onset of plasticity:** Given the values for the Tabor parameter the onset of plasticity will be intermediate between the criteria given by the JKR and DMT theories. According to JKR theory the onset of plasticity under only the action of attractive forces (at zero load) is given by equation (75). Asperities of reduced radius less than  $R_Y^{JKR}$  will yield plastically. For TA toners,  $R_Y^{JKR} = 0.08 \mu\text{m}$ , and for TB toners,  $R_Y^{JKR} = 0.67 \mu\text{m}$ . In the case of DMT theory we obtain from equation (77) that  $R_Y^{DMT} = 0.073 \mu\text{m}$  for TA toners and  $R_Y^{DMT} = 0.63 \mu\text{m}$  for TB toners. We may conclude that for our toners asperities will on average yield plastically, even at zero load, as they have reduced radius of  $0.05 \mu\text{m}$ , slightly and substantially smaller the values quoted above for TA and TB toners, respectively.

**Onset of full plasticity:** The next question is to know if the contact is fully plastic. In the Maugis–Pollock approximation, for the contact to be fully plastic we must have  $P + 2\pi R w = \pi a_p^2 H$  with  $H = 2.8Y$ , and  $a_p \simeq 60RY/E$ . This gives for the limiting radius

$$R_p^{MP} = \frac{\pi w + \sqrt{\pi^2 w^2 + AP}}{A}, \quad A \simeq \frac{\pi 10^4 Y^3}{E^2} \quad (93)$$

For TA toners,  $R_p^{MP} = 2.75 \text{ nm}$ , whereas for TB46 and TB48 is  $8.59$  and  $8.62$  nanometres, respectively.

We conclude therefore that the contact is elastic–plastic. Thus, we need a model for the elastic–plastic contact in order to estimate the pull-off force needed to separate the particles as a function of the pull-on force.

## 7.2. Adhesive contact in the elastic–plastic regime: an approximate model

**Loading of the contact:** Neither the stress tensor, nor the load-area curve, are known in the adhesive elastic–plastic regime. We propose here to extend the simple model for loading of the Hertzian elastic–plastic contact to the case of adhesive contacts [78].

In an axisymmetric contact the load force  $P$  for a given contact area radius  $a$  must balance the pressure  $p_{ep}$  due to elastic and plastic stress on the contact area and the attractive pressure  $p_a$  due to the interparticle attractive forces:

$$P = \int_0^a 2\pi s p_{ep}(s) ds + \int_0^c 2\pi s p_a(s) ds \quad (94)$$

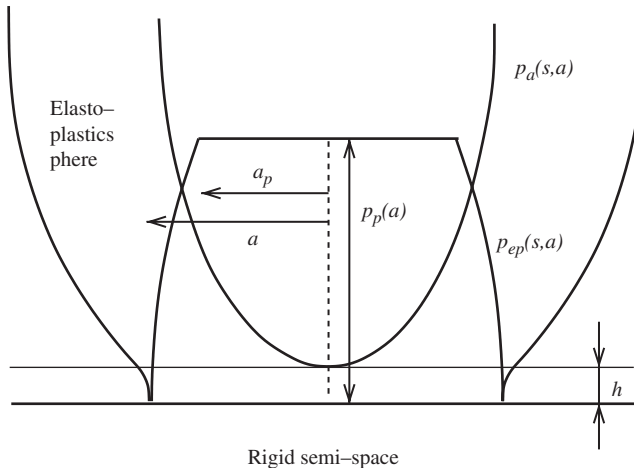


Figure 17. Elastic–plastic and attractive pressures in the area of contact. The level of plastic pressure (flat part) is determined by the expressions given in equation (96).

where  $s$  is the radial coordinate on the contact area,  $p_{ep}$  and  $p_a$  are the elastoplastic and attractive pressures, and  $c$  is the distance beyond which the attractive forces vanish. We restrict our study to the case  $c = a$ . In this case  $p_a$  can be taken from the JKR model for the elastic adhesive contact [47]:  $p_a(s) = -\sqrt{2wEa}/\sqrt{\pi(a^2 - s^2)}$ .

When loading the contact we assume that  $p_{ep}$  is a composition of the solutions already existing for the fully plastic and fully elastic contacts of the pressure as in the case of elastic–plastic non-adhesive contact [79]. For the case of adhesive contact we have to add the tensile pressure as shown in figure 17, Then we may put

$$p_{ep}^L(s, a) = p_p(a)\Theta(a_p - s) + \frac{2E}{\pi R}\sqrt{a^2 - s^2}\Theta(s - a_p) \quad (95)$$

where  $\Theta$  is the Heaviside function, the superscript  $L$  stands for loading, and  $p_p(a)$  is given by

$$p_p(a) = \begin{cases} 0 & \text{below plastic yield} \\ \frac{2E\sqrt{a^2 - a_p^2}}{\pi R} & \text{if } p_p < H = 2.8 Y \\ H & \text{otherwise} \end{cases} \quad (96)$$

To solve for  $a_p$  and  $P$  (for given  $a$  and  $w$ ), an additional equation is needed. We assume that the average value of the elastic–plastic pressure on the contact area (denoted from now on simply as  $\bar{p}^L$ ), increases with the contact area radius  $a$  for  $a > a_Y$  as in equation (70):

$$\frac{\bar{p}^L}{\bar{p}_Y^L} = 1 + \frac{2Y}{3p_Y^L} \ln \frac{a}{a_Y} \quad (97)$$

The value of the contact area radius  $a_Y$ , and the average elastic pressure  $\bar{p}_Y^L$  at the onset of plastic yield are calculated using the von Mises criterion in the JKR model for the elastic adhesive contact. The solution of this system of equations yields the values of  $a_p$  and  $P$  for every fixed value of the contact area radius  $a \geq a_Y$ .

**Unloading the contact:** During unloading we assume that stresses and deformation are predominantly elastic, as happens in simulations of elastoplastic non-adhesive contacts [54]. The elastic pressure  $p_e$  is denoted as  $p_e^U$  and is obtained solving [52]:

$$p_e^U(s, a) = \frac{E}{\pi} \int_s^a \frac{f(\xi)}{\sqrt{\xi^2 - s^2}} d\xi \quad \text{with} \quad f(\xi) = -\frac{2}{E} \frac{\partial}{\partial \xi} \int_{a_p}^{a_f} \frac{sp^l(s, a_f)}{\sqrt{s^2 - \xi^2}} ds. \quad (98)$$

where the superscript  $U$  stands for unloading. We have, for  $f(\xi)$ :

$$\begin{aligned} f(\xi) = & \frac{2\xi}{R} \Theta(\xi - a_p) \\ & + \Theta(a_p - \xi) \left[ \frac{2p_p \xi}{E \sqrt{a_p^2 - \xi^2}} - \frac{4}{\pi R} \frac{\partial}{\partial \xi} \int_{a_p}^{a_f} \sqrt{\frac{a_f^2 - s^2}{s^2 - \xi^2}} ds \right] \\ & + \delta(\xi - a_p) \left[ \frac{2p_p}{E} \sqrt{a_p^2 - \xi^2} - \frac{a_f^2 - \xi^2}{R} + \frac{4}{\pi R} \int_{a_p}^{a_f} \sqrt{\frac{a_f^2 - s^2}{s^2 - \xi^2}} ds \right] \end{aligned} \quad (98)$$

Inserting  $f(\xi)$  in (98) yields  $p_e^U$ . Adding the attractive pressure  $p_a$ , a straightforward numerical integration over the contact area allows us to obtain the force acting on the contact  $F_c(a)$  during unloading. The minimum of  $F_c(a)$  during unloading corresponds to the force of adhesion  $F_a$  for the previously applied load force  $F_c(a_f)$  (see figure 18).

### 7.3. Results

All existing models based on contact mechanics are valid for particles without additives, thus we chose to measure the toners with the lowest additive content but still fluidizable. In figure 19 we show the comparison between the elastic-plastic model, as well as the modified Maugis-Pollock model with the experimental results for the TA005 toner. The measurements have been presented in terms of accumulated frequencies, i.e. the box 80% means that 80 per cent of the measurements lie below the line within the box. Each point represents the average of ten measurements. In figure 20 the comparison is made for toners TB46 and TB48.

The agreement between the model and the experimental results for TA005 toner is fairly good. For TB toners (TB46, TB48) we see a significant deviation in the region of low applied loads. This is to be expected since these toners have a few percentage of silica-silica contacts, and these contacts decrease on one hand the local radius of curvature, and on the other hand increase the hardness, both effects leading to a decrease in the interparticle forces, equation (86).

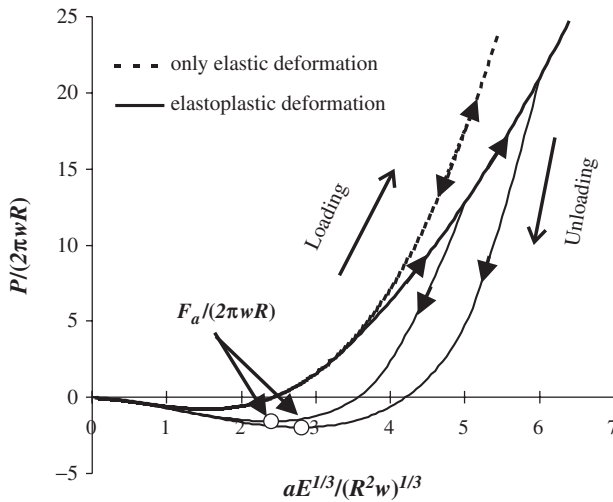


Figure 18. Loading and unloading curves for  $(H/E)(ER/w)^{1/3} = 2$ . Two examples are shown corresponding to different values of the final loading force. The particle properties used are:  $E = 3.5$  GPa,  $\nu = 1/3$ ,  $H = 300$  MPa,  $w = 0.07$  J/m<sup>2</sup>, asperity radius  $0.1$   $\mu\text{m}$ , particle diameter  $12.7$   $\mu\text{m}$ .

It is to be noticed that the modified Maugis–Pollock formula predicts smaller values of adhesion than the elastoplastic model. In our opinion this happens because in formula (86) (see [52, 62]), the attractive forces are neglected during the indentation process. When the attractive forces are imposed at the end of the loading cycle a sudden increase of radius  $a$  must necessarily happen. Thus, disregarding this increase may lead to a serious underestimation of the final contact area at the end of loading.

We must bear in mind that contact models depend on parameters that are not well determined. The work of adhesion of polymers depends on the changing molecular configurations and motions of polymer chains and their segments at adhering and shearing junctions [80], as well as the contamination of the surface, and it is not well known for our materials. We have taken a typical value for polymers as quoted by Persson [77]. Typically the work of adhesion of polymers<sup>†</sup> is comprised between 0.01 and 0.1. The second rough approximation has been to take an average value for the local radius of curvature of  $0.1$   $\mu\text{m}$ . While this may be justified for our attrition made toners it must be accurately determined for other particles. The third approximation is to assume that the contact is only between two asperities. It is also quite possible to have contacts among several asperities. Finally, the mechanical properties are not precisely determined for our materials. In addition, Young's modulus varies from point to point on the surface, and the same is true for the compressive yield strength of polymer particles. Therefore, before concluding on the validity of the approximate model we need to test it with particles with much better defined physical

<sup>†</sup>See [www.surface-tension.de/solid-surface-energy.htm](http://www.surface-tension.de/solid-surface-energy.htm), [www.engineeringreference.com/Properties/surface.htm](http://www.engineeringreference.com/Properties/surface.htm), among others.

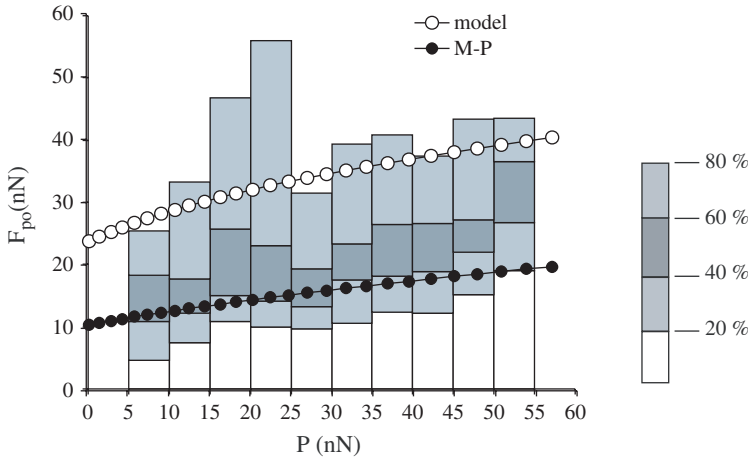


Figure 19. Pull-off force  $F_{po}$  (denoted in the text as  $F_a$ ) versus pull-on force  $P$ . Comparison of the elastic–plastic and the modified Maugis–Pollock models with experimental AFM measurements for TA005. The particles properties are:  $E_p = 3.5$  GPa,  $\nu = 1/3$ ,  $H = 300$  MPa,  $w = 0.07$  J/m<sup>2</sup>, asperity radius  $0.1$   $\mu\text{m}$ , particle diameter  $12.7$   $\mu\text{m}$ .

properties, and to investigate its theoretical foundation by means of extended cavity models and numerical simulations.

**Final considerations:** Due to the complexity of particle interactions it is evident that the theories presented above will not allow us to predict with great accuracy the pull-off force as a function of the pull-on force. However, these concepts from contact mechanics are clear to grasp, and are of great value to guide us in the interpretation of experimental measurements. As it is apparent from figure 14b there is almost a superposition of measured values for TB46 and TB48, and this is consistent with the fact that in both toners contacts are predominantly between the parent toner materials. In the same figure it is clearly seen that an increase in the additive content, for both TA and TB toners, leads to a substantial decrease on the interparticle forces. Again this is to be expected as the additives decrease the interparticle forces.

After these theoretical considerations we may conclude that much more research in this area is needed to measure the fundamental parameters we have discussed in this section, radius of particle, roughness, surface energy, Young modulus and yield strength, as they are clearly needed in order to determine the pull-off force as function of the applied load. It is also necessary to avoid contamination by foreign particles or by fragments of the particle itself due to wear.

## Part II: Powders at the bulk level

### 8. Mechanical properties

Powders are multiphase media consisting in our case of low consolidated assembly of solid particles (of micron size) in ambient gas. As is the case for all granular media

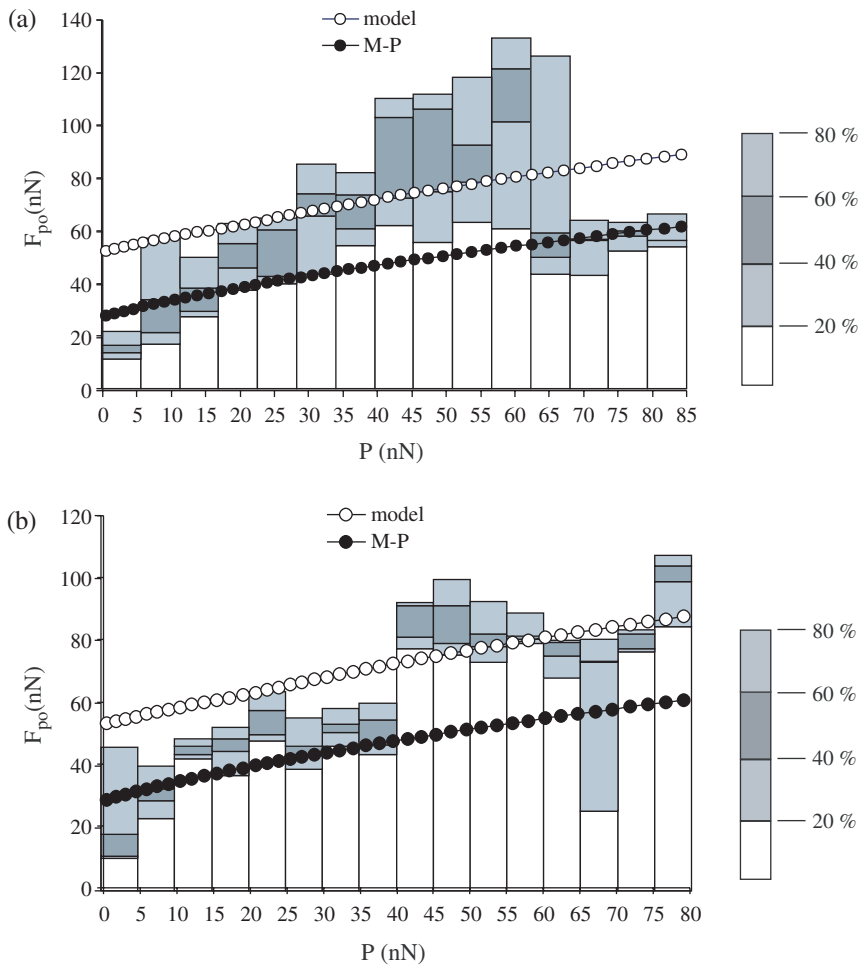


Figure 20. Pull-off force  $F_{po}$  (denoted in the text as  $F_a$ ) versus pull-on force  $P$ . Comparison of elastic–plastic and modified Maugis–Pollock models with experimental AFM measurements for TB46 (a) and TB48 (b). The particles properties are:  $E_p = 3.5$  GPa,  $\nu = 1/4$ ,  $H = 150$  MPa,  $w = 0.07$  J/m<sup>2</sup>, asperity radius  $0.1$   $\mu$ m, particle diameter  $7$   $\mu$ m.

their bulk properties depend on the geometry of particle positions, the geometry, direction and strength of interparticle forces at each contact, and the interaction with the interstitial gas. Unfortunately we cannot measure the interaction between two particles within the powder, neither the drag force of a particle of powder in the flowing interstitial gas. Also, visualization and tracking of individual powder particles is extremely difficult.

We consider first the mechanical properties of a loosely consolidated powder in the regime of permanent contacts and neglecting gas interaction, i.e. as a “solid”. The essential difficulty is the extreme sensitivity of geometry of particles and geometry of contacts to weak external forces and boundary conditions. Because of this, fine powders suffer structure transitions quite easily, and their mechanical properties

depend on their past history. This is why there is no any continuum theory able to predict their complex behaviour. Another consequence is that it is quite difficult to obtain reproducible measurements, which in fact is the more important problem to overcome. Generally the techniques employed lack a satisfactory way of initializing the powder in order to have a reproducible state in which the memory of the powder has been erased. Moreover the more cohesive the powder the large are memory effects. Consequently traditional testers present large experimental variations in powder bulk properties at low consolidations.

We have developed a powder fluidized bed technique, called the Sevilla powder tester (SPT), that yields initial states, “microscopically” different but macroscopically equivalent, allowing us to obtain reproducible measurements of density and a specific kind of tensile stress, that we call uniaxial (oedometric) tensile stress, both as function of load and particle properties. But prior to its discussion, we would like first to present briefly two simple models, and highlight some of the most used techniques in powders from a critical perspective.

### 8.1. Rigid-plastic solid

The simplest model for granular materials was introduced by Coulomb [81]. He assumed that the material is a continuum medium with uniform density,  $\rho$ . The stress tensor,  $\tau$  satisfies the equilibrium equation

$$\nabla \cdot \tau + \mathbf{f} = 0 \quad (99)$$

with appropriate boundary conditions. Here  $\mathbf{f}$  is the force density, which in most cases is  $\rho\mathbf{g}$  with  $\mathbf{g}$  the acceleration. The powder remains in static equilibrium, unless at a given point there is a plane for which  $|\tau| = \mu_{nc}\sigma$ , with  $\tau$  the absolute value of the tangential stress and  $\sigma$  the normal stress acting on that plane. The parameter  $\mu_{nc}$  is the coefficient of internal friction, and it is the only material parameter which characterizes the granular medium. The angle  $\alpha_{nc} = \arctan \mu_{nc}$  is called the angle of internal friction. For cohesive materials this relation is generalized to  $|\tau| = \mu_c(\sigma + \sigma_t)$  with  $\mu_c = \tan \alpha_c$ , and  $\sigma_t$  the tensile strength of the powder. If the same material is compressed to a higher uniform density, both the angle of internal friction and the tensile strength increases. This relation is a straight line in the  $\sigma$ - $\tau$  plane and it is called the Coulomb yield locus of the material (see figure 21). The value of  $\tau$  needed to break the powder in shear at zero normal stress,  $c = \mu_c\sigma_t$ , is by definition the cohesion of the powder.

A similar yield locus exists for the interaction of the powder with the wall,  $|\tau| = \mu_W(\sigma + \sigma_t^W)$ , with  $\mu_W$  the powder-wall friction coefficient and  $\sigma_t^W$  the normal force per unit area needed to separate the powder from the wall, called wall adhesion.

This rigid-plastic model does not include dilatancy. We determine the set of sliding surfaces by the method of characteristics assuming that at each point of the material there is a plane that satisfies equilibrium together with the Coulomb relation, within the powder and along the walls [82].

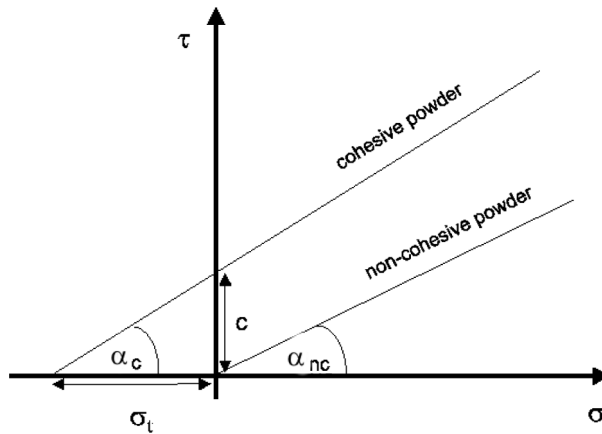


Figure 21. Ideal Coulomb yield locus of powders.

## 8.2. Elastic-plastic solid

Powders yield under high hydrostatic pressures, contrary to metal solids. For each fixed value of density exists another branch of the yield surface, called the consolidation yield locus that connect the yield locus to point  $\sigma_c$  as shown in figure 22. Another remarkable feature of the yield locus is its convex shape at low stresses (stresses near  $\sigma_t$ ). Thus, we have yield loci composed of two branches. The yield locus correspond to points of incipient yielding with the powder dilating thus decreasing its density, whereas in the consolidation locus the powder yields with increasing density.

Typical devices (shear cell testers) for measuring these loci are shown in figure 23. Traditionally the Jenike shear cell [83] has been used by engineers in powder technology to obtain the yield locus. In order to erase as much as possible the initial memory of the powder, the material is always presheared under a fixed normal load to attain the critical state, i.e. flow at constant density under constant shear stress. The yield locus is obtained with the Jenike cell decreasing in steps the normal load (always taking as the initial state for each normal load the critical state) and determining the shear for the onset of incipient yielding. To obtain the consolidation locus we stress the powder by a normal compressive stress to a density intermediate between the density at the critical state and the density at point  $\sigma_c$ . Then, we impose an increasing shear stress. First, the powder keeps a constant density until the point of incipient yield is attained. Increasing the shear stress further, and keeping the normal load constant, the porosity will decrease until we reach the critical state.

The critical state does not belong to any of the loci. According to Jenike the Mohr circle of the critical state must be tangent to the loci at their end points. This definition is however approximate, as we may have experimental points of the yield locus above this one [84]. Note that  $\sigma_c$  is neither an hydrostatic pressure, nor the intersection of the Mohr's circle tangent to the yield locus at the critical state. Similarly  $\sigma_t$  is not the tensile strength of the material, but an uniaxial tensile stress as measured in oedometers, although in Jenike cell tensile stresses can no be attained. The line connecting the origin to the end point of the yield locus is called the effective yield locus.

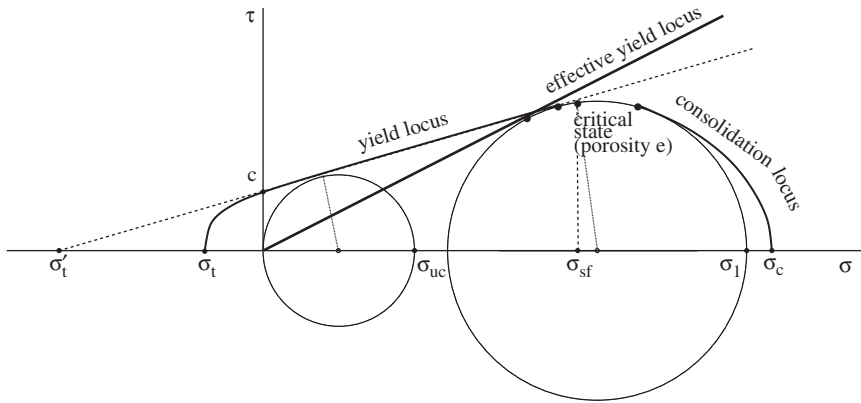


Figure 22. Yield loci of cohesive powders: relation between  $\sigma$ ,  $\tau$  and porosity  $e$ . The porosity is defined only for the critical state, as it changes along the yield and consolidation loci. With higher preconsolidation loads the porosity decreases and the yield loci expand.  $\sigma_t$  is the tensile strength,  $\sigma'_t$  is the apparent tensile strength,  $\sigma_{uc}$  the unconfined yield strength,  $\sigma_{sh}$  is the preconsolidation shear,  $\sigma_1$  is the intersection with the  $\sigma$ -axis of the Mohr circle corresponding to preconsolidation load, and  $\sigma_c$  the consolidating stress at zero shear.

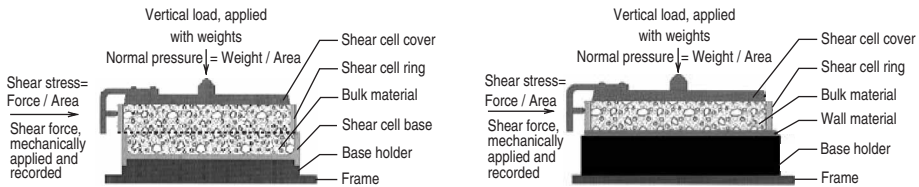


Figure 23. Shear cells used to measured the Coulomb yield within the powder (Jenike cell) (left), and along the wall (right).

In figure 24 we show schematically the relation between  $\sigma_t$ ,  $\sigma_c$ , and porosity  $e$ . When we represent these yield loci as a function of powder porosity,  $e$ , we have a surface in the space  $e, \sigma, \tau$ , called the Roscoe condition diagram of shown in figure 25. The surface bounded by the critical state line and the line  $\sigma_c(e)$  on the quadrant  $e > 0, \sigma > 0$  is the consolidation surface, while the one bounded by the critical line and the  $\sigma_t(e)$  curve is called by Roscoe the flow surface. States below the surface are in equilibrium and respond elastically to stress fields, while states above the surfaces are not allowed. It is beyond the scope of this paper to discuss in detail the way in which the different measurement processes for powders are represented in this diagram (for a detailed discussion of this diagram we refer the reader to [85]).

Unfortunately, in the Jenike cell it is not possible to keep the density of powder constant both during initial deposition and the subsequent manipulation, neither is it possible in general to force the powder to break along perfect planes. Because of this, a precisely defined protocol is needed in order to minimize operator dependence of the experimentally determined “yield locus”. For example, the Jenike cell is commercialized with a reference material with which researchers can check both their

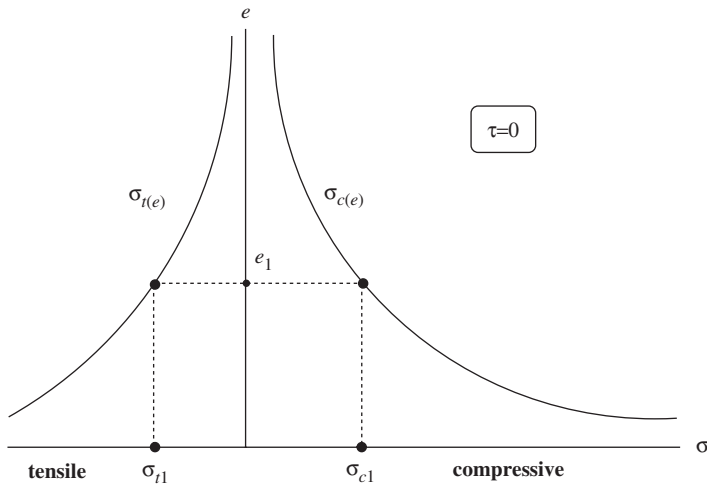


Figure 24. Relation between  $\sigma_t$ ,  $\sigma_c$  and porosity  $e$ .

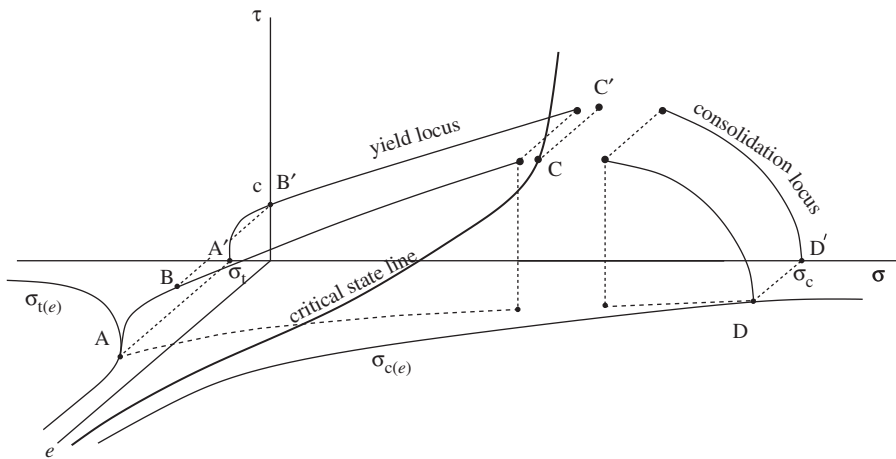


Figure 25. Condition diagram of Roscoe.

equipment and experimental technique. The reference powder consists of “3 kg of limestone powder packed in a polyethylene jar” and is accompanied by a certificate that supplies the limiting shear stress for four different powder normal stresses. These problems are aggravated at small and very small consolidations, as will be obvious from our review of the state of the art measurements in powders. Thus, the Roscoe diagram is not accessible to precise experimental determination for loosely consolidated powders, with the exception, perhaps, of two recently developed powder testers: the ring shear tester by Schulze *et al.* [84] and the aerated Pechl shear cell by Barletta *et al.* [86]. These apparatuses are able to measure the yield locus of powders at very small consolidations. However, in these shear testers special care

has to be taken to obtain a reproducible initial state (operator-independent of the filling procedure). Also, the cells need to be powder tight in order to avoid loss of the initial mass for highly fluidizable powders as the preconsolidation loads are imposed.

### 8.3. Review of the techniques for measuring powder properties and flowability

Schwedes has recently made an extensive review of testers for measuring bulk flow properties of granular materials [87]. In this section we highlight, from a critical perspective, some of the most commonly used techniques in powders.

**8.3.1. Empirical techniques.** A traditional way of testing powder flowability is to measure the ability of the powder to flow through standard devices [88]. For example, we find in the *Book of the American Society for Testing and Materials Standards* a technique that consists of measuring the time that a given mass of powder takes to discharge through a hopper [89]. Even though this technique has been proved to be useful for metallic powders, an external energy source such as tapping is needed for very cohesive powders to help powder flow [90]. Vibration however may consolidate the powder and, specially in the case of fine particles, this enhances cohesiveness. A similar technique, frequently used for pharmaceutical tableting applications, consists of forcing the powder to pass through rings of decreasing diameters [91]. The flowability index is defined as the diameter of the smaller ring through which the sample can discharge three consecutive times. We find also a commercial rheometer similar to the ones employed to measure the viscosity of liquids, that has been adapted to test powder flow [92]. The rheometer incorporates a blade with different sections in the opposite sides of a rotation shaft. The first section has its surface parallel to the rotation shaft whereas the second section is twisted relative to the rotation shaft.

The Hosokawa powder tester [93] is another instrument that has been extensively employed in the xerographic industry to measure toner flowability. In the Hosokawa test a number of screens of different sizes are placed vertically and are vibrated. An estimation of the toner flowability is given by the relative mass of powder that passes through each screen.

The success of these techniques is hindered by the difficulty of initializing the powder in a reproducible state. Therefore, results are dependent on the history of the powder: filling procedure, previously applied stresses, etc. This is particularly important in the case of fine cohesive powders for which interparticle attractive forces may increase by several orders of magnitude with the applied external load [94–96]. An additional problem is that the interaction of the powder with mechanical parts, such as the blade of a rheometer, may produce an “heterogenous” cohesiveness since the load and shear applied can change abruptly from point to point within the sample. Thus the results achieved depend on the particular design of the device and on the experimental procedure. In particular, the reproducibility is poor due to the lack of proper initialization. In figure 26 we present the results of three independent measurements† where the lack of reproducibility is clearly seen, even though a

---

†The experiments were performed by F. Da Cruz and F. Chevoir, and the details of the experimental apparatus may be seen in [97].

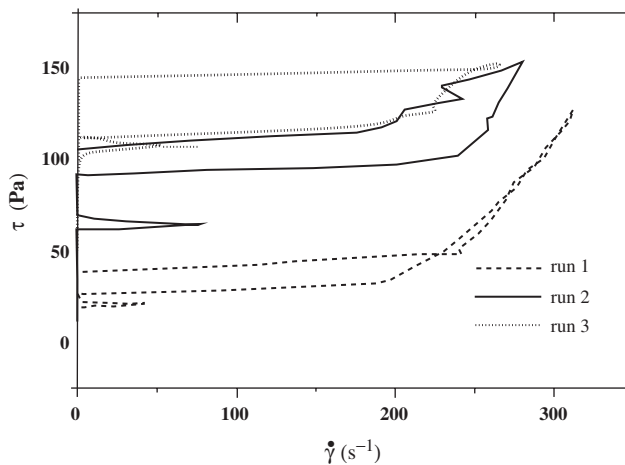


Figure 26. Rheogramme of toner CLC700: torque as function of the rate of deformation.

constant high shear was initially imposed until reaching a steady state in order to erase memory of the process of putting the powder into the rheometer.

In addition, the correlation of the experimental results to fundamental physical parameters of the powder remains rather obscure. Therefore, it would be desirable to measure properties more directly linked to fundamental parameters thus yielding more robust and confident results.

**8.3.2. Techniques of analysing powder flowability based on fundamental properties.** All powder testers provides the user with some value of flowability. The more widely used is the flow function introduced by Jenike,  $\sigma_{uc} = ff_c(\sigma_1)\sigma_1$  (see figure 22). The flowability index,  $ff_c$ , is the ratio of the unconfined yield strength, to the preconsolidation level  $\sigma_1$ , and it depends on the latter. According to Tomas [98] powders are classified as: (1)  $4 < ff_c < 10$  free flowing; (2)  $10 < ff_c < 100$  easy flowing; (3)  $2 < ff_c < 4$  cohesive; (4)  $1 < ff_c < 2$  very cohesive; and (5)  $1 < ff_c$  non-flowing. However the Jenike cell is only appropriate for high consolidation stresses. The recently developed ring shear tester, that represents a great technical improvement on the Jenike tester, is able to measure the yield locus at much smaller loads ( $\sim 100$  Pa) [84]. However, the values of  $ff_c$  tend to 1 for all powders tested [84], which makes this index somewhat inaccurate to characterize flowability at very low consolidations.

An experimental problem that besets the Jenike cell technique and its modified versions is the lack of a reliable method of obtaining reproducible initial states while filling the cell. Interparticle contact forces are very sensitive to small variations of the previous external loads. As a result errors due to poor preparation method can easily arise. Further disadvantages of the Jenike test are that it must be accepted that the slip plane coincides with a horizontal plane and that the shear process takes place uniformly throughout the sample in order to relate the forces to the real stresses inside the material, and this is known to be false [21, 87]. A commercial alternative to the Jenike shear cell is the Peschl annular shear cell, in which the shear stress is

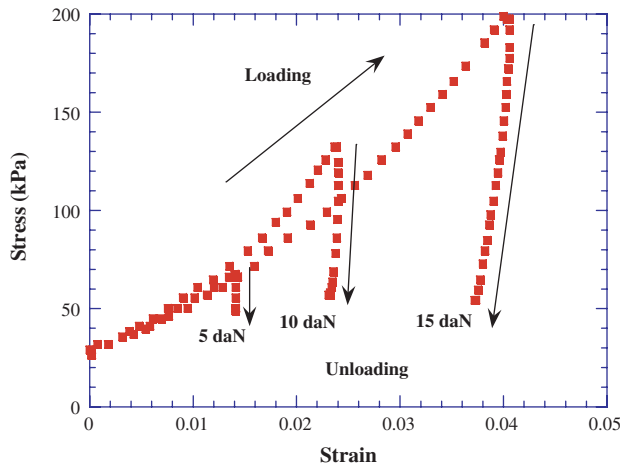


Figure 27. Piston consolidation of toner CLC700 for compressive loads of 5 daN, 10 daN and 15 daN.

applied by rotating the top part of an annular shear box wherein the powder sample is contained [21]. While this test allows for a constant area of shear and unlimited shear distance, making it useful for quantifying powder flow after failure, wall effects and strong uncertainty in stress distribution are major drawbacks. Recently, the Peschl shear tester has been modified to allow aeration of the powder and the application of loads lower than the lid weight [86]. This apparatus is able to go as low as 100 Pa in the yield loci of aerated and non-aerated powders. A major drawback is the lack of reproducibility of the initial state of the powder. New improvements leading to a better definition of the initial state of fine powders at very low consolidations are clearly needed.

Powder compressibility has usually been taken as a measure of powder flowability [99]. Granular materials that flow well end up in very dense packings that are quite difficult to compress, whereas poorly flowing powders pack in open structures that can be further compressed easily. Compaction tests in which a cylindrical plug of powder is compacted axially by a piston are commonly used in civil engineering [100]. In figure 27 we present the results of three independent measurements<sup>†</sup> where the lack of reproducibility is evident even for high normal stresses. Another proposed number to classify powder flowability is the Hausner ratio, defined as the ratio of the tapped powder density to the untapped powder density [102].

Another property that has been employed to quantify powder flow is the angle of repose of a pile of powder [103]. Even though the angle of repose is a well defined property of noncohesive granular materials it is meaningless when cohesive interaction becomes important [82]. We can remember from our childhood that sand-castles may sustain  $90^\circ$  slopes but when we tried to increase the size of the

<sup>†</sup>The experiments were performed by X. Jia. The details of the experimental cell may be seen in [101].

castle landslides would likely happen that decreased the angle of repose well below  $90^\circ$ . The influence of the size of the powder sample on the avalanching behaviour of fine powders is well documented in the literature [104]. Therefore, the size of the pile, which is indeed an external parameter, must be specified in the testing procedure when dealing with cohesive powders.

A common tool to analyse the avalanching behaviour of powders is a horizontal rotating drum partially filled with the granular sample. In this device intermittent and nearly reproducible avalanches are observed for low rotation speeds. For low cohesive well-behaved granular materials avalanches occur quite regularly, with nearly uniform size and time spacing, whereas in the case of poorly flowing cohesive powders the time spacing and size of avalanches shows a noisy behaviour [105]. A rotating drum based equipment, developed by Kaye and coworkers [106], is now commercially available. In this device avalanches are automatically detected by a change in the light intensity captured by a grid of photocells placed behind the drum. The avalanching behaviour is characterized by the time interval between consecutive avalanches. The scatter of the points is a measure of the regularity of the avalanche process. In this technique a gas conditioning system can be implemented [107] in order to control gas conditions inside the chamber that may have a profound effect on powder flowability. Testing cohesive powders is however difficult and the test usually yields inaccurate results. A source of error is that the powder gets easily stuck to the walls of the drum and this reduces visibility. As a result the light intensity series can easily become non-stationary whereas the number of avalanches per unit time detected decreases, thus complicating the analysis of the data. In the case of very cohesive powders it is likely also that the powder slips as a whole. A further criticism is that just the data on the time interval between consecutive avalanches can not be enough to analyse cohesive systems with complex dynamics. For instance, Quintanilla *et al.* [105] have seen that for a class of cohesive powders there is a regular sequence of large avalanches preceded by a number of two or three small precursors. In such cases an in depth statistical analysis is needed.

Since flowability is closely linked to interparticle forces it can be thought that a good bulk test is to measure the powder tensile yield stress for which interparticle attractive force is responsible. The split cell tester is a commercial device able to measure a tensile yield stress [21]. The sample is held in a ring shaped cell and is compacted vertically using a plunger. Then a horizontal tensile stress is applied and steadily increased until the sample is pulled apart. In this way the tensile yield stress for a given consolidation stress is measured. In the lifting-lid tester the sample is pulled vertically in the same direction of compaction [21]. These techniques presents some inconveniences when applied to fine cohesive powders. One of them is again the lack of a mechanism for initializing the powder into a reproducible state of consolidation. As a consequence, results are of poor reproducibility. Another is the difficulty of measuring the tensile yield stress of fine cohesive powders at low consolidation stresses by means of piston consolidation. It must be remarked that the way of preparation and compaction of the powder in the cell does not produce an isotropic state of stresses. Therefore, the tensile yield stress does not have to coincide with the tensile strength. Research tools such as triaxial tests achieve an approximated isotropic behaviour by using hydrostatic compaction, but is applicable only to high compression loads.

#### 8.4. The Sevilla Powder Tester: a new tool to characterize fine cohesive powders at very small consolidations

In figure 28 a schematic view of the automated Sevilla powder tester (SPT) is shown. The powder samples are supported on a porous plate in a vertically oriented cylindrical vessel. Pore size of the distributor plate is  $\sim 5\mu\text{m}$  to ensure that toner particles do not penetrate into the pores and that the gas stream is distributed uniformly over the lower boundary of the bed. By means of a series of computer controlled valves a controlled dry nitrogen flow can be pumped upward or downward through the bed. In this way the gas flow can be used to vary automatically the consolidation stress on the powder. By using dry nitrogen, the complicating effect of humidity, which is known to affect particle adhesion [1], is minimized. The gas flow is controlled by a mass flow controller while the gas pressure drop across the bed  $\Delta p$  is measured by a differential pressure transducer. Readings of the pressure drop across the porous plate (without toner in the cell) are taken before each series of powder measurements. In all the range of gas flows we used there is a linear dependence of the pressure drop across the plate versus the gas flow velocity. The powder sample is weighed and then placed in the vessel; at this stage the sample is quite inhomogeneous, with some loose and some compacted areas. To homogenize the sample the bed is driven into the freely bubbling regime by imposing a large gas flow. In the case of highly cohesive powders, such as toners with very low additive concentration, it is necessary to shake the sample in order to break up channels that conduct fluidizing gas away from the bulk of the powder and prevent fluidization. For that purpose an electromagnetic shaker is incorporated to the setup in the base of the bed [108, 109]. The bed under vibration is allowed to bubble during a time period large enough to reach a stationary state in order to maximize the erasing of memory of the initial

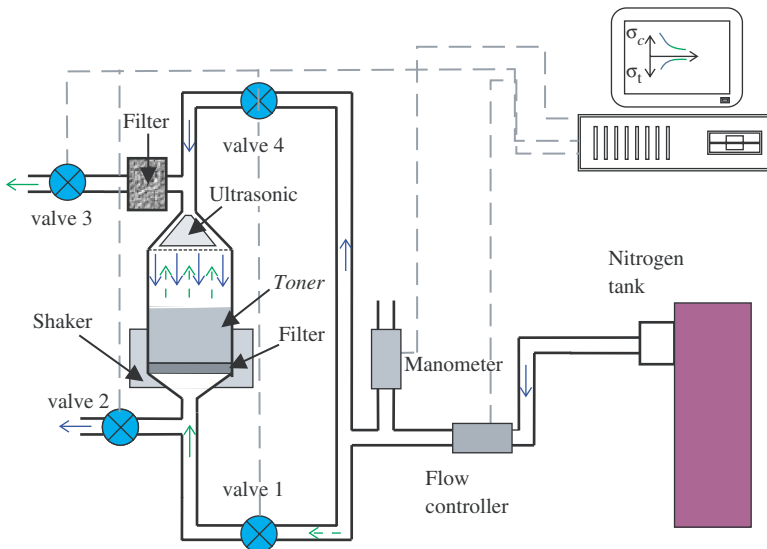


Figure 28. Layout of the Sevilla Powder Tester (SPT).

state [110], and after that the gas flow is suddenly returned to zero. This gives a repeatable starting condition for the powder.

Consider first that the powder is allowed to settle under its own weight. Then, the height of the bed  $h$ , which is automatically measured by means of an acoustic pulse technique, provides an average value of the particle volume fraction

$$\langle \phi \rangle = \frac{m_s}{\rho_p A h} \quad (100)$$

where  $m_s$  is the powder mass,  $\rho_p$  is the particle density that must be known beforehand, and  $A$  is the cross sectional area of the vessel. The average void fraction or porosity is defined by  $\langle e \rangle = 1 - \langle \phi \rangle$ . The consolidation stress  $\sigma_c$  at the bottom of the bed is assumed to be the total weight of the sample divided by the area of the gas distributor.

We subject the vertical layer of powder to an upward directed flow of gas that is slowly increased to put the bed under tension. The total pressure drop is measured and the pressure drop across the gas distributor is subtracted from it. This is shown in figure 29. When the gas passes through the packed bed of particles the gas pressure drop is due to frictional resistance and increases linearly with increasing gas flow at low Reynolds numbers as described in general by the Carman equation [111]

$$\frac{dp}{dx} = \frac{E\mu}{d_p^2} \frac{\phi^2}{(1-\phi)^3} v_g^2 \quad (101)$$

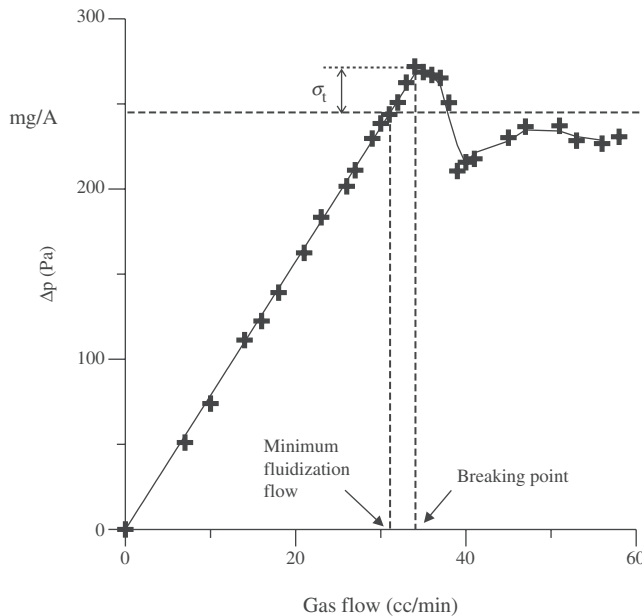


Figure 29. Pressure drop across a bed of toner (Canon CLC500 cyan) consolidated by a consolidation stress  $\sigma_c \simeq 70$  Pa. Cross-sectional area of the bed  $20.3 \text{ cm}^2$ .

where  $x$  is the vertical coordinate measured downward from the free surface of the bed,  $\mu$  is the dynamic gas viscosity ( $\mu = 1.89 \times 10^{-5}$  Pa · s at ambient temperature for dry nitrogen),  $v_g$  the superficial gas velocity, and  $E \simeq 180$  is an empirical constant. There is a critical gas velocity at which the powder fractures and the gas pressure drop across the bed  $\Delta p$  falls abruptly. Visual observations reveal that fracture takes place on a surface, within the powder, and close to the bottom. We define a tensile stress for the powder at the bottom,  $\sigma_t$ , as the difference between the maximum pressure (the pressure at the breaking point) minus the gravitational pressure due to its own weight (see figure 29). This tensile yield stress is a well defined quantity provided the powder always fails across a surface close to the bottom. Obviously, the surface will be always rough and greater than  $A$ , so that our  $\sigma_t$  is an overestimation of the true tensile stress.

To compress the powder above the sample weight per unit area, after the powder has settled, the valves are operated to change the gas flow path to the reverse mode. Then the downward directed gas flow is slowly increased from zero to a given value. The gas imposes a distributed pressure over the granular assembly pressing it against the distributor plate. The consolidation stress at the base of the bed is thus increased up to

$$\sigma_c = W + \Delta p_0 \quad (102)$$

where  $W = \rho_p \langle \phi \rangle gh$  and  $\Delta p_0$  is the downward directed gas pressure drop. Further increasing the compressing gas flow imposes further pressure on the sample.

On the other hand the automatic powder tester provides us with a useful technique to test the powder under very low confining pressures like in microgravity. To decrease  $\sigma_c$  below the powder weight per unit area we allow the powder to settle under a remaining upwards directed flow. In this way  $\sigma_c$  is lowered down to

$$\sigma_c = W - \Delta p_0 \quad (103)$$

where  $\Delta p_0$  is the pressure drop of the remaining gas flow reducing consolidation.

As before the uniaxial tensile yield stress of the consolidated sample is measured by slowly increasing an upward directed gas flow that subjects the bed to a tensile stress. figure 30 show the gas pressure drop across the bed during the breaking process for over-consolidated and under-consolidated states respectively. As consolidation is increased it is clearly seen that the slope of the linear part increases as a consequence of the increase of the average particle volume fraction. The overshoot of the pressure over the weight per unit area (i.e. the uniaxial tensile yield stress) also increases. Conversely when the sample consolidation is subsequently decreased the average particle volume fraction decreases and hence the slope of the linear part decreases and the uniaxial tensile yield stress decreases.

Figures 31 and 32 give an idea of the sensitivity of the SPT to differentiate the flowability of apparently similar powders. In figure 31 we present the phase diagrams, for two samples of different colour of the toner Canon CLC700 (magenta and cyan), yielded by the aeroflow meter [106], a rotating drum in which the profile of the powder is recorded with an array of photodetectors as function of time. The time of

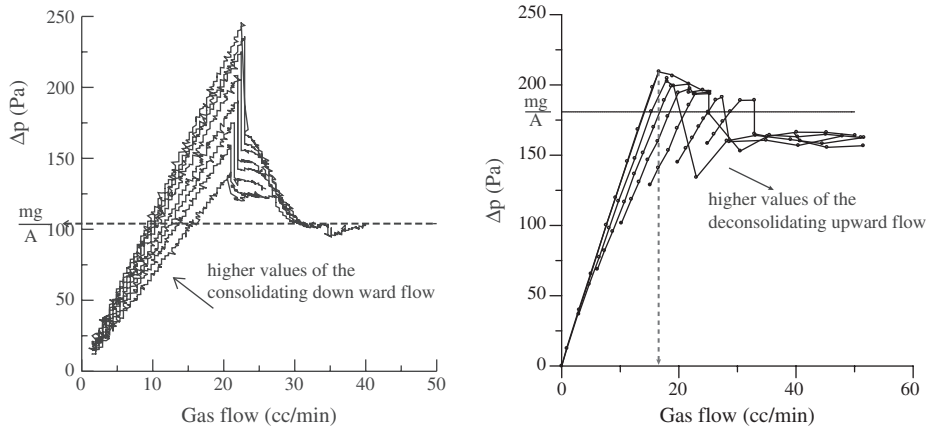


Figure 30. Gas pressure drop versus gas flow for a given mass of xerographic toner (with 0.05%wt. of silica) previously consolidated with a downward directed gas flow. Curves in the left direction correspond to increasing values of the compressing gas flow and hence to increasing values of the consolidation stress  $\sigma_c$ . Curves in the right direction correspond to increasing values of the decompressing gas flow and hence to decreasing values of the consolidation stress  $\sigma_c$ .

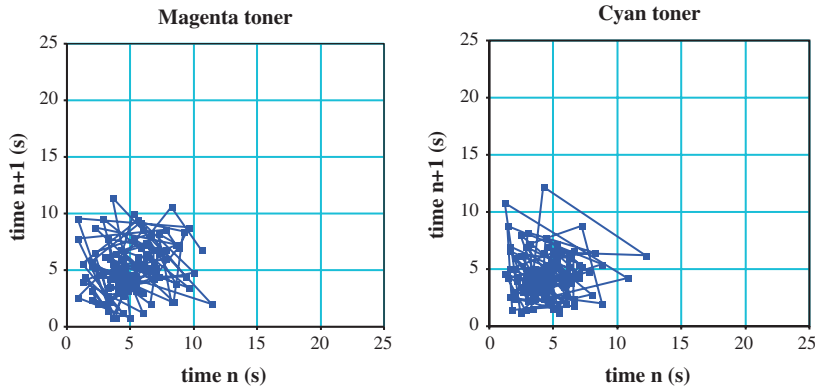


Figure 31. Delay reconstructed attractor map for two samples of different colour (magenta and cyan) of the commercial xerographic toner Canon CLC700. The points of time  $T_n$  at which an avalanche occurs are represented against the time  $T_{n+1}$  of the next avalanche.

each avalanche is plotted versus the time of the next avalanche. It is difficult to establish a quantitative difference in the flowability of both samples.

Figure 32 shows the average particle volume fraction of both samples as a function of the consolidation stress applied by the downward gas flow, equation (102). Now both toners are well separated. As a consequence of their better ability to flow the magenta toner particles are able to pack in a more compact structure for the same consolidation stress and this is clearly captured by the SPT. A straightforward

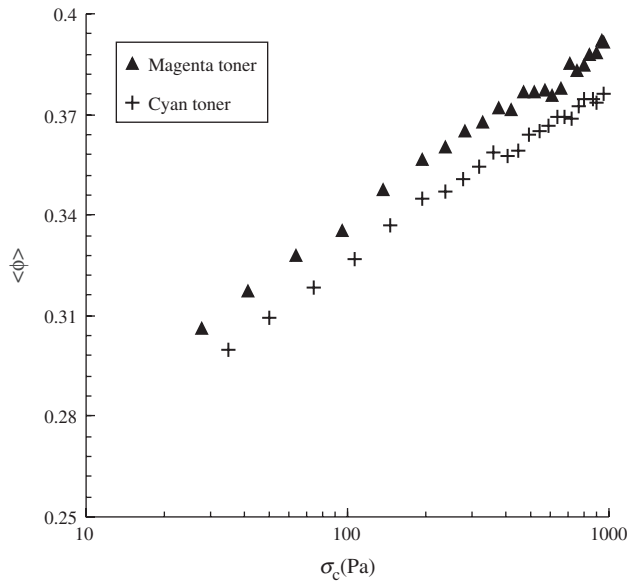


Figure 32. Average particle volume fraction as a function of the consolidation stress measured using the SPT for two samples of different colour (magenta and cyan) of the commercial xerographic toner Canon CLC700.

extension of the SPT consisting of using nitrogen with controlled relative humidity enables the characterization of powder flow under well-controlled ambient conditions.

**Location of fracture in the fluidized bed:** Tsinontides and Jackson [112] predicted theoretically and later observed that fracture always takes place at the bottom of the bed. In their one-dimensional analysis they neglected the wall effect and considered the uniaxial stress  $\sigma$ , local particle volume fraction  $\phi$  and gas pressure depending only on the vertical coordinate  $x$ . Next we give a slightly modified analysis of that of Tsinontides and Jackson to show explicitly that the condition for tensile yield will be first met at the lowest point of the bed as the gas flow is progressively increased.

In the consolidated equilibrium state, previous to the application of gas flow, there are no external forces acting upon the particles except for the gravity force. We have a compressive stress  $\sigma_c(x)$  across the bed that obeys the simple equation

$$\frac{d\sigma_c}{dx} = \rho_p \phi g \quad (104)$$

The vertical coordinate  $x$  is measured downward from the free surface of the bed. When the gas is forced to pass through the bed we must also consider the drag force per unit total volume  $F_s$  exerted by the gas on the particles, which is given by the gas pressure drop per unit length  $F_s = dp/dx$ . Then the force balance equation is

$$\frac{d\sigma}{dx} = \rho_p \phi g - \frac{dp}{dx}, \quad (105)$$

Since in fine powders the gas flow usually is at small Reynolds numbers it is admitted that  $F_s$  is proportional to the gas velocity  $F_s \approx \beta(\phi)v_g$ . For a sufficiently large gas velocity the negative contribution of the drag force will turn the stress  $\sigma$  negative and equal to the tensile yield stress  $\sigma_t$  at some point within the bed. In order to find the yield condition, equation (102) must be integrated. There are several empirical equations in the literature for  $\beta(\phi)$ . Tsinontides and Jackson found it reasonable to adopt the Richardson–Zaki equation [113]:

$$\beta(\phi) = \frac{\rho_p \phi g}{v_t} \frac{1}{(1 - \phi)^{n-1}} \quad (106)$$

where  $n$  is  $\sim 5$  for small Reynolds number and  $v_t$  is the sedimentation velocity of a single particle,  $v_t = (1/18)(\rho_p - \rho_g)d_p^2 g/\mu$  ( $\rho_g$  is the gas density), in the Stokes regime. While equation (106) describes well the behaviour of fluidized beds at small values of the particle volume fraction, the Carman equation (101), gives the best results for  $\phi > 0.3$  [23]. Since we are looking for the yield point of the granular solids at large values of  $\phi$ , equation (101) seems more appropriate to us for the pressure gradient. The integration of equation (105) yields

$$\sigma(x) = \int_0^x \rho_p \phi(\xi) g \left\{ 1 - \frac{10\phi(\xi)}{[1 - \phi(\xi)]^3} \frac{v_g}{v_t} \right\} d\xi \quad (107)$$

where we have used  $E = 180$  and the gas density has been neglected as compared to particle density.

Let us consider first the simplest case of a homogeneous bed in which  $\phi = \phi_0$  and  $\sigma_t = \sigma_{t0} < 0$  are constants throughout the bed. Then we have

$$\sigma(x) = \rho_p \phi_0 g x \left( 1 - \frac{10\phi_0}{(1 - \phi_0)^3} \frac{v_g}{v_t} \right) \quad (108)$$

i.e. the uniaxial stress across the bed will increase linearly with a slope that decreases as the gas velocity is increased. Eventually the slope becomes negative and for a sufficiently large gas velocity  $\sigma$  will equal  $\sigma_{t0}$  at the point where  $|\sigma|$  is maximum, which is always the bottom of the bed. Note that if  $\sigma_t$  increases with the depth of the bed (due to an increase in consolidation for example) the fracture will occur also at the base of the sample as long as there is a non-vanishing  $\sigma_{t0}$ , at the free surface (tensile yield stress at zero consolidation).

A more realistic approach is to take into account that  $\phi(\xi)$  increases with the depth of the bed as a result of the increase of the local consolidation stress. In the whole range of consolidations tested we may obtain a good fit to the experimental data on the average particle volume fraction  $\langle \phi \rangle$  for the Canon CLC700 toner by the modified hyperbolic law

$$\langle \phi \rangle(\xi) = 1.366 - \frac{1.088}{(1 + 3.969 \xi)^{0.02454}} \quad (109)$$

with a regression coefficient  $R = 0.9954$ . (see figure 33). To apply this formula we need to assume that the average particle volume fraction  $\langle \phi \rangle(\xi)$  from the free

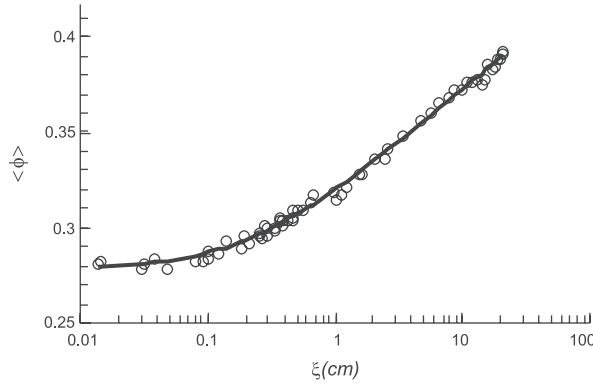


Figure 33. Average particle volume fraction as a function of the effective depth measured from the top free surface. The continuous curve represents the modified hyperbola fit equation (109).

surface to a depth  $\xi$  in a bed of total height  $x$  is equal to the measured  $\langle\phi\rangle$  in a bed of total height  $\xi$ . From the definition of  $\langle\phi\rangle$

$$\langle\phi\rangle(\xi) = \frac{1}{\xi} \int_0^{\xi} \phi(\lambda) d\lambda \quad (110)$$

we may derive the local particle volume fraction  $\phi(\xi)$

$$\phi(\xi) = \langle\phi\rangle(\xi) + \xi \frac{d\langle\phi\rangle(\xi)}{d\xi} \quad (111)$$

to be used in equation (107). Figure 34 shows the new profiles of the uniaxial stress obtained by numerical integration of equation (107) for different values of the gas velocity. The essential difference with respect to the uniform case is the convex shape of  $\sigma(x)$  due to the increase of the drag force with depth. The consequence is that the yield condition is more neatly met at the base of the sample.

According to equation (105) the total gas pressure drop across a bed of height  $h$  at yield,  $(\Delta p)_Y$ , is given by the powder weight per unit area plus the tensile yield stress at the bottom

$$(\Delta p)_Y = \rho_p \langle\phi\rangle gh + |\sigma_t(h)| \quad (112)$$

Thus the overshoot of  $\Delta p$  beyond the bed weight per unit area when the powder fails gives us a quantitative measure of the uniaxial tensile yield stress  $\sigma_t(h)$ .

**Rate of gas flow:** For practical purpose we have checked that the tensile yield stress is not sensitive to the rate of increase of the gas flow. Figure 35 shows results of  $\sigma_t$  for a given sample obtained using different rates. It is seen that the deviation between the results is within the experimental scatter ( $\pm 1$  Pa).

**Dependence of results on porous plate properties:** As noted by Tsinontides and Jackson [112] the condition for tensile yield can be met either at the lowest point within the powder bed or at the contact between the bed and the gas distributor plate. However, we have consistently observed that the gas distributor surface always

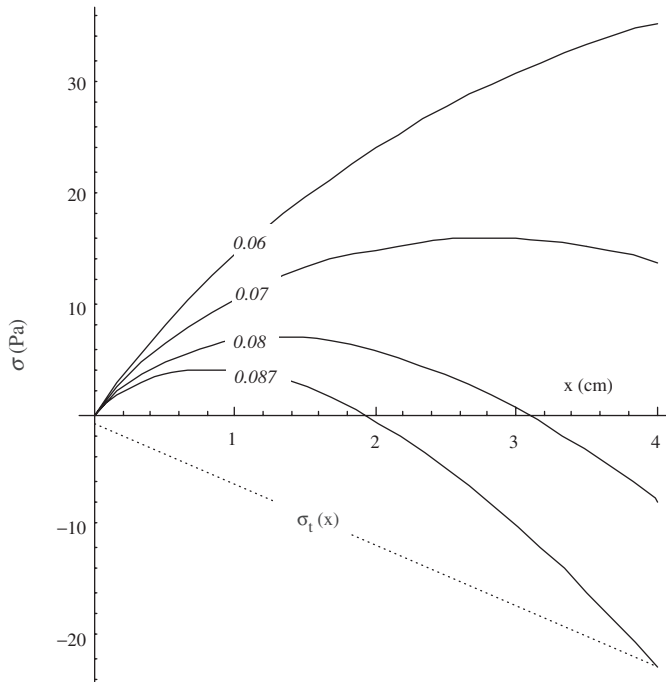


Figure 34. Continuous lines: uniaxial tension ( $\sigma$ ) across a non-homogeneous bed of powder as the gas flow is increased (the ratio of the gas velocity to the sedimentation velocity of an individual particle  $v_g/v_t$  is indicated for each curve). The free surface is at  $x=0$  and the bottom at  $x=4$  cm. The calculation is performed for Canon CLC700 toner with particle density  $\rho_p = 1199 \text{ kg/m}^3$  and average particle volume fraction given by equation (106). The dotted line is the experimental tensile yield stress ( $\sigma_t = 1 + 5.5x \text{ Pa}$ ) for Canon CLC700. The yield condition ( $\sigma = \sigma_t$ ) is met at the bottom of the powder ( $x=4$  cm) for  $v_g/v_t \simeq 0.087$ .

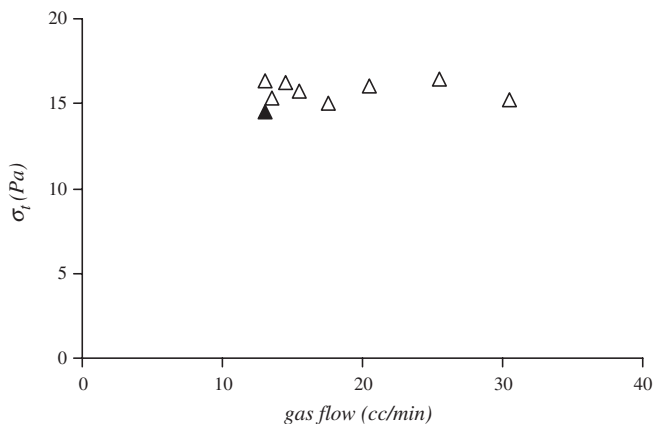


Figure 35. Uniaxial tensile yield stress measured by increasing quasistatically the gas flow (solid triangle) and by imposing instantaneous values (void triangles) of the gas flow represented in the horizontal axis. The gas flow is measured in cubic centimetres per minute.

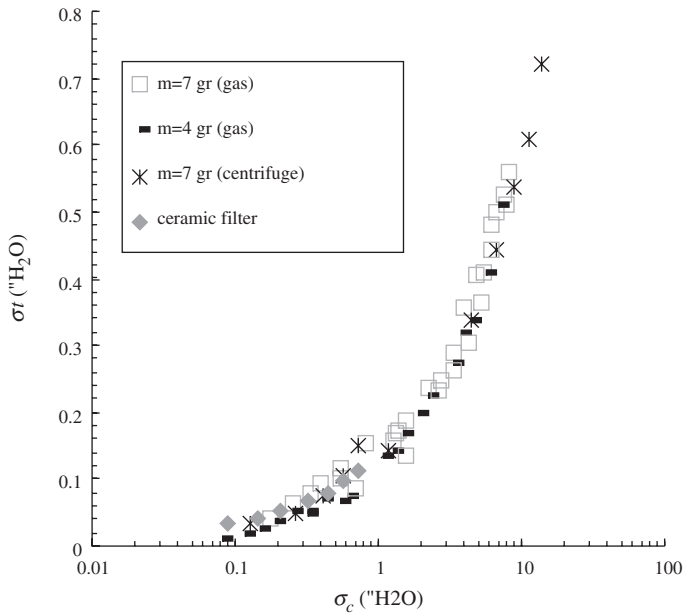


Figure 36. Uniaxial tensile yield stress as a function of the consolidation stress for toner TA02 (TA toner with 0.2% concentration by weight of additive). Data from different tests: (1) using consolidation by gas (two tests with samples of different masses) and centrifuging in a bed with a metallic gas distributor, and (2) data obtained in a bed with a ceramic gas distributor where consolidation was increased by adding new mass to the sample, are jointly plotted.

remains covered by a thin layer of powder after the break. Thus the measurement is indeed that of the tensile yield stress of the powder rather than a measure of the interface strength between the distributor plate and the powder. As a further proof we present in figure 36 experimental measurements of  $\sigma_t$  using both metallic and ceramic gas distributor plates. Within the experimental scatter the results fit to a single curve.

**Wall effects:** It is well known that minimum fluidization velocity may be affected by lateral walls (see [114] and references therein). This effect may lead the experimenter to the erroneous conclusion that his material has cohesion. Valverde *et al.* [94] have checked that wall effects are negligible for particles with typical size of  $\sim 10 \mu\text{m}$  in beds with typical heights not larger than their diameter as can be seen in figure 37. Data of the average particle volume fraction from circular section beds and from a rectangular section bed fit within the experimental scatter to a single curve.

**Consolidation by gas flow versus gravity or centrifugal consolidation:** In our early investigations two techniques were employed in order to test the powder under different consolidation stress. In the first one the powder mass was varied by adding powder to the bed [94]. In the second one the vessel with the powder inside was centrifuged prior to measuring the tensile yield stress [115] thus increasing the apparent gravity by  $g_a = (g^2 + \omega^4 r^2)^{0.5}$ , where  $\omega$  is the angular velocity and  $r$  the average

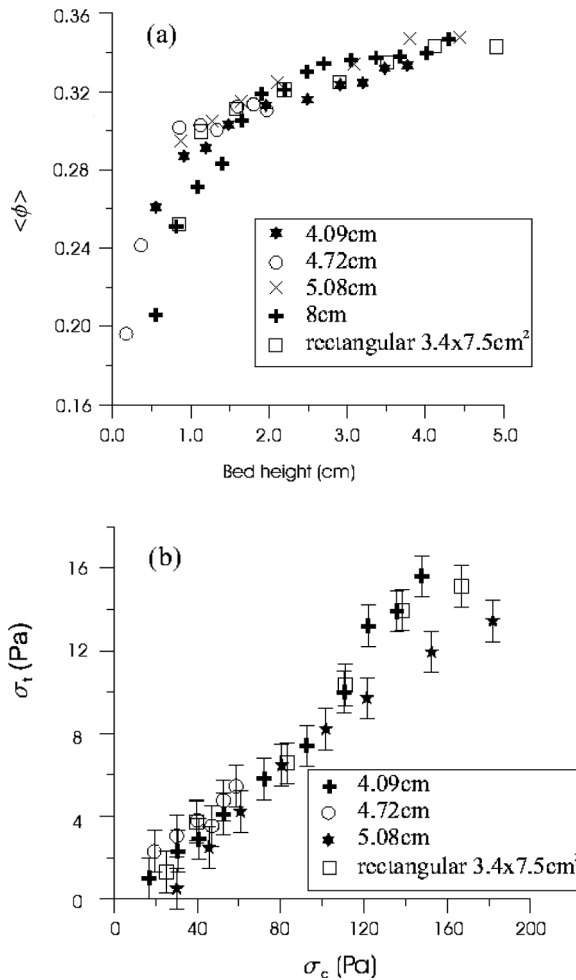


Figure 37. (a) Average particle volume fraction as a function of the bed height. (b) Test of the uniaxial tensile yield stress versus consolidation stress. Data obtained for toner with 0.4% additive obtained with different bed diameters (4.09 cm, 4.72 cm, 5.08 cm, 8.0 cm) and with a rectangular bed.

radius at which the bed is rotating (see figure 36). These techniques needed to be performed by a human operator and therefore none of them allowed for automation of the measurements. Furthermore there are some difficulties related to testing the powder under very low or high consolidations. For very small consolidation stresses, beds of extremely low height must be used. In such cases it was likely that non-uniform consolidation allowed the gas to flow preferentially through regions of high porosity such as channels. In the other extreme, if we wanted to achieve high consolidations by adding mass to the bed, its height should be increased up to values larger than the bed diameter for which wall effects are not negligible. In those cases the tensile yield stress measured had an important contribution from the wall friction as shown by figure 38.

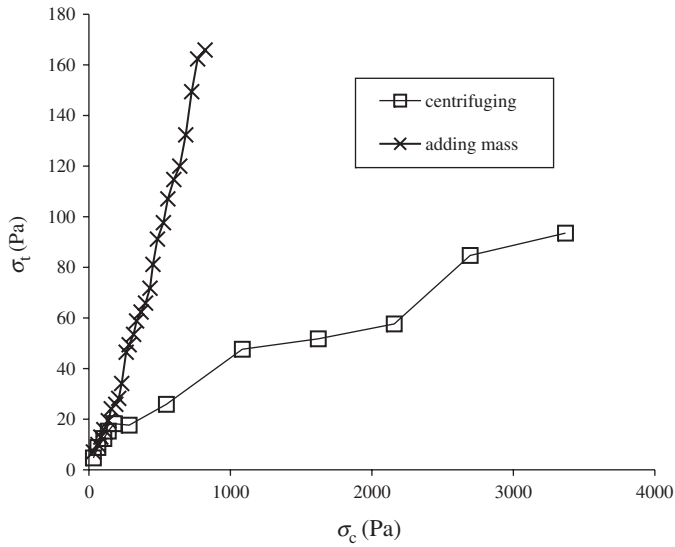


Figure 38. (a) Average particle volume fraction as a function of the bed height. (b) Test of the uniaxial tensile yield stress versus consolidation stress. Data obtained for toner with 0.4% additive obtained with different bed diameters (4.09 cm, 4.72 cm, 5.08 cm, 8.0 cm) and with a rectangular bed.

These problems were solved by using the gas flow as an agent to compress or decompress the powder. The gas flow can be used to vary automatically the consolidation stress on the powder avoiding at the same time wall effects and inhomogeneous gas distribution through shallow layers.

**Final remarks:** The yield condition will be more neatly met at the base of the powder for the most cohesive toners ( $|\sigma_t|$  large) while a large portion of powder remains far from the yield condition. In contrast for low cohesive powders ( $|\sigma_t|$  small) stresses will be close to the tensile yield stress throughout all the material, therefore, in practice, the fracture will be less clearly visible at the base. In our experimental work we observe a variety of behaviour at the yield point depending on the magnitude of the tensile yield stress and in agreement with this theoretical prediction. For the most cohesive powders the fracture at the bottom is clean and the powder rises in the bed as a plug. Furthermore the bottom of the plug does not erode as it rises in the bed. The toner without flow additives behaves in this way. For powders with intermediate–large cohesiveness fracture of the bed is still clearly visible and plugs are still formed, but the plug erodes as powder agglomerates fall away from its lower surface. The plug then becomes unstable and collapses at a certain height. Examples of this behaviour are toners TA001 and TA005 (12.7  $\mu\text{m}$  particle size). For powders of low cohesiveness plugs are rarely visible. After the break at the bottom of the bed, the fracture propagates until a certain height. Then, the gas escapes from the powder through channels which erupt like miniature volcanoes. The less the cohesiveness of the toner, the less stable are the channels. These effects are observed for example in the toners TA01 and TA02. Finally, for the

least cohesive powders, for example the experimental toner TA04 or Canon CLC700 toner, plugs do not develop, channels are very unstable, and a state of homogeneous fluidization is easily reached. We note however that these types of behaviour depends also on the consolidation stress  $\sigma_c$  that influences the tensile yield stress as we will see. In that sense, beds of small  $\sigma_c$  favour the formation of channels, whereas highly consolidated beds favour the formation of stable plugs.

## 8.5. Experimental results

**8.5.1. Materials.** We have investigated three sets of model toners. The first two are the TA and TB toners already described (see tables 1 and 2). The third set of toners (TC toners) is made of copolymer styrene *n*-butylmethacrylate. Particles have density  $\rho_p = 1.185 \text{ g/cm}^3$ , and different sizes. They have also varying weight percentage of silica particles additives of 8 nm and density  $\rho_s = 2.2 \text{ g/cm}^3$ . In table 3 we present their properties. The naming of toners indicates their approximate diameter and approximate surface area coverage *SAC*.

**8.5.2. Viscosity effects in interparticle contacts.** An interesting experiment that can be automatically performed with the powder tester is to subject the sample to a fixed value of the consolidation stress for a controlled period of time. After this time period the consolidation stress is removed and the tensile yield stress is measured. The increase of the tensile yield stress gives us an insight of the viscosity effects of the interparticle contacts. From a practical point of view the increase of tensile stress with time of consolidation during storage is a relevant issue. Our measurements for xerographic toners indicate that the estimated adhesion force [116] rises exponentially to a maximum in a time scale that depends on the load imposed and on the

Table 3. TC toners,  $d_p$ : particle diameter in  $\mu\text{m}$ . % weight: % in weight of the additive relative to toner particle weight. SAC surface area coverage.  $\text{SAC}_a$  aggregate surface area coverage.  $(\text{SAC}_a)_{pp \rightarrow ps} = 2.18\%$  aggregate surface area coverage for the transition of polymer–polymer to polymer–silica contacts.  $(\text{SAC}_a)_{ps \rightarrow ss} = \pi/16 \simeq 20\%$  is the surface area coverage for transition of polymer–silica to silica–silica contacts.

Toner	$d_p$	% weight	SAC (%)	$\text{SAC}_a$
TC8-8	7.8	0.062	8.14	2.60
TC8-16	7.8	0.124	16.3	5.21
TC8-32	7.8	0.250	32.8	10.5
TC8-64	7.8	0.490	64.3	20.6
TC12-8	11.8	0.041	8.14	2.61
TC12-16	11.8	0.081	16.1	5.15
TC12-32	11.8	0.163	32.4	10.1
TC12-64	11.8	0.325	64.6	20.7
TC15-8	15.4	0.031	8.04	2.57
TC15-16	15.4	0.062	16.1	5.14
TC15-32	15.4	0.125	32.4	10.4
TC15-64	15.4	0.250	64.8	20.7
TC19-8	19.1	0.025	8.04	2.57
TC19-16	19.1	0.050	16.1	5.14
TC19-32	19.1	0.100	32.1	10.3

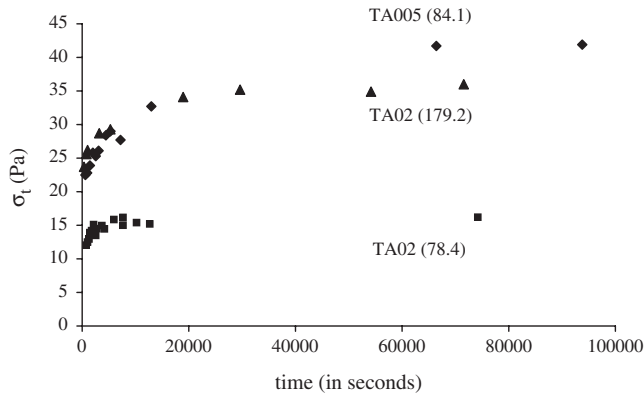


Figure 39. Tensile stress as a function of the time during which the powder is consolidated. Examples are shown for TA toner particles with different surface Aerosil coverage and subjected to different load forces (indicated in parenthesis).

additive surface area coverage. Figure 39 indicates that as the load is increased while keeping constant the surface additive coverage the relative increase of the adhesion force gets more pronounced. A similar behaviour is obtained if the surface additive coverage is decreased while keeping constant the load. Therefore, not just the actual value of the adhesive force for a given load force, but also the time of application of the force, plays a role in the compression process, suggesting a viscoelastic/viscoplastic deformation of the contact in large time scales. To avoid viscosity effects the SPT data presented here were taken from measurements made within a short time scale ( $t < \sim 5$  min.).

**8.5.3. Effect of particle properties and flow additives on the cohesive properties of bulk powder.** The SPT experimental results provide us with a direct qualitative insight of the relationship between the parameters that govern interparticle contact and the tensile stress, compressive stress and average volume fraction of the bulk powder.

**Effect of surface area coverage for fixed particle size:** In figure 40a we present the diagram that can be obtained from the SPT. It shows the interdependence between the consolidation stress, the tensile yield stress and the porosity for TA toners. Clearly, for each toner a higher consolidation implies larger average particle volume fraction and tensile yield stress. In the upper part of the figure it is seen that for a given consolidation stress, the particle volume fraction has larger values for higher additive levels. This is a direct result of the increase in flowability with increasing additive, which increases the ability of the toner particles to rearrange themselves at a given stress. For a constant value of the consolidation stress the tensile yield stress increases with decreasing additive concentration. In figure 40b  $\sigma_t$  is plotted versus  $\sigma_c$  for the same value of porosity. We may clearly see the transition between polymer–polymer contacts (below 0.1% in weight of flow control additives) to polymer–silica contacts (above 0.1%). The decreasing of tensile stress is directly related to the

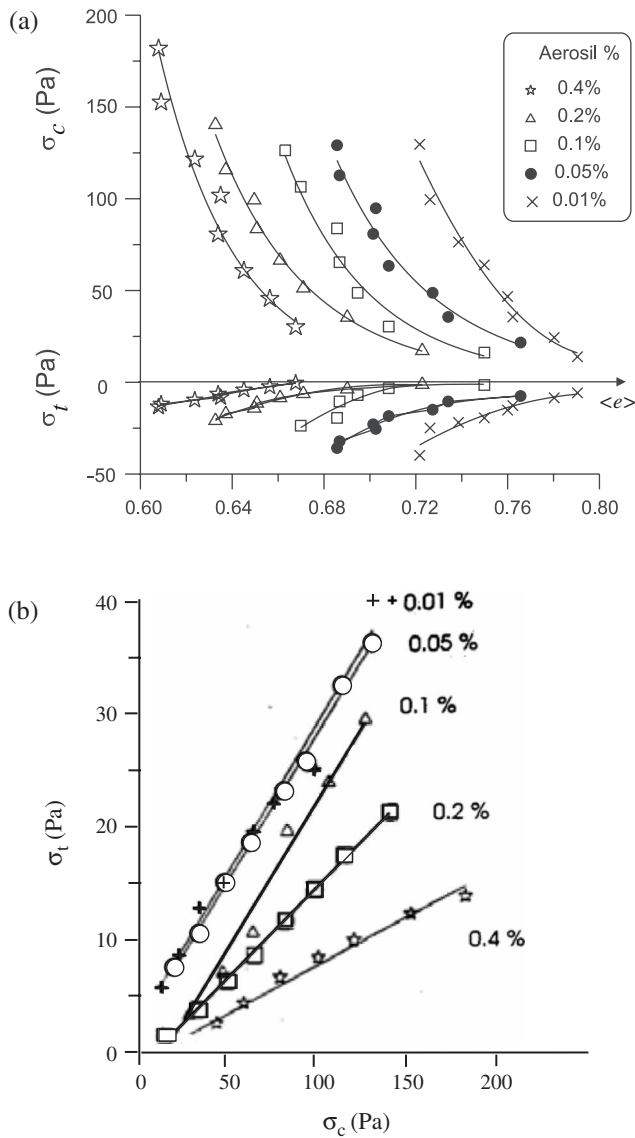


Figure 40. (a) Tensile yield stress as function of consolidation stress and porosity, for toners with  $\approx 12.7 \mu\text{m}$  particle size and different surface additive coverage (SAC) levels. (b) Plot of the tensile stress as a function of consolidation stress for the same porosity.

decrease in interparticle forces. First, with increasing additive concentration the effective radius at contact decreases as we change the polymer–polymer contacts to polymer–silica and silica–silica contacts. Secondly, silica is harder than cross-linked polyester thus further decreasing the interparticle force due to plasticity. Though our contacts need not to be fully plastic, the role of surface energy, local radius and hardness in the elastic–plastic contact follow the trends indicated by equation (86) (see subsection 5.3).

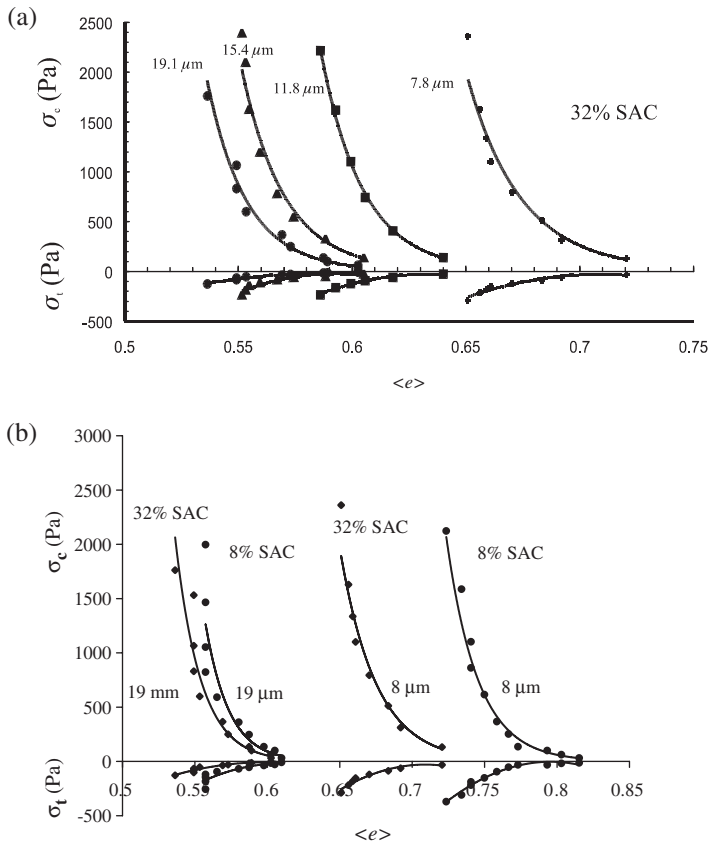


Figure 41. (a) Tensile yield stress as a function of consolidation stress and porosity for toners with different particle size and constant surface additive coverage level 8 %; (b) particles with diameters 7.8 and 19.1  $\mu\text{m}$  and surface area coverages of 8 and 32% SAC respectively).

**Effect of particle size for fixed surface area coverage:** From theory it follows that, for identical toner particles, surface area coverage of flow additives determine the strength of interparticle forces. In figure 41 is shown the effect of weight of the particle for the same surface properties.

For the same SAC, larger particles pack more efficiently as the ratio of interparticle forces decreases in relation to its weight, i.e. their cohesive granular Bond number decrease, and they may roll more easily over each other. For the same reason the importance of interparticle forces decreases as the size of the particle increases as shown in figure 41b. We would like to stress that cohesion of powders depends on the attractive interparticle forces, but not only on that. In effect, contrary to the case of two isolated interacting particles (fixed to the cantilever and the piezoelectric in the AFM apparatus), particles in the powder may form and break contacts. In addition bulk cohesion depends also on the ratio of attractive to normal contact force in the network of contacts. However, the latter depends both on the imposed load, and the weight of the particle. Therefore, for low consolidations, the ratio of

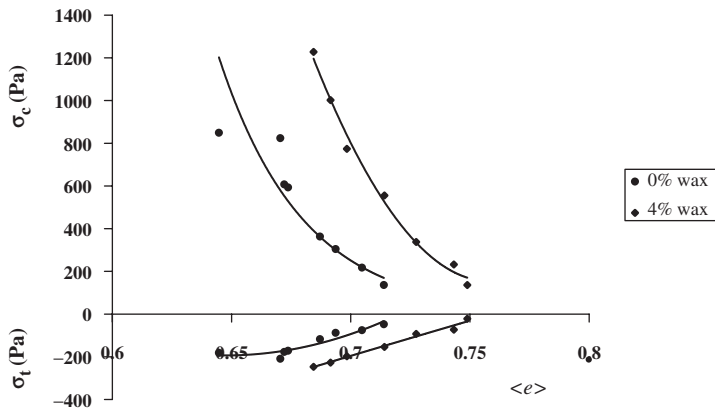


Figure 42. Tensile yield stress as a function of consolidation stress and porosity for two (otherwise identical) toners with 0% and 4% in weight of wax in the base polymer.

attractive force to particle weight may play an essential role in bulk cohesion. On the contrary, for large consolidations, i.e. much larger than the attractive forces, cohesive powders approach the behaviour of noncohesive grains. This is why the cohesion measured in powder testers is not directly related to the adhesive forces between particles. Therefore, interparticle forces alone do not determine bulk powder behaviour.

**Effect of hardness:** The hardness of a particle may be decreased adding a softer material, such as wax, to the parent polymer (see figure 42), or it may be increased by adding a cross-linking agent to the parent polymer, and/or by coating the particle with harder additive particles (usually made of  $\text{SiO}_2$  or  $\text{TiO}_2$ ). In figure 43a the result of increasing hardness of the base polymer by means of a cross-linking agent is distinctly seen, in qualitative agreement with equation (86). When the particle is coated with a monolayer of flow additives the hardness at contact is determined by the silica particles only, as it is evident from figure 43b. We may also see that the particles with 100% SAC are less cohesive than those with 20% SAC, thus indicating that the silica particles are harder than the cross-linked polymer.

## 9. Interparticle forces versus bulk stresses: a semiquantitative approach

Mechanical properties of powders depend in an essential way on the assembling procedure. We may obtain quite different ‘materials’ by depositing the same particles on a substrate one by one, by letting them to aggregate in a gas-like state before applying a confining pressure, or by settling them under gravity as in our powder bed technique. Therefore, in order to correlate quantitatively interparticle measurements between individual particles to bulk stresses we need to understand the underlying structure of the settled powder layer in the SPT. This in turn requires an understanding of the structure of fluidized beds. Here, we focus the analysis on the aggregation process and aggregate settling as they determine the packing structure of the settled layer. Therefore, the onset of fluidization [117], and the detailed study

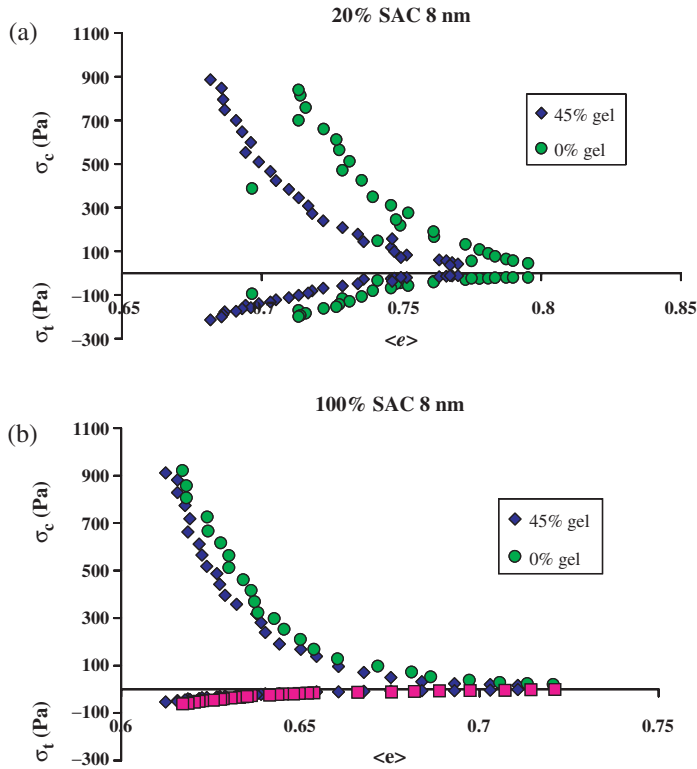


Figure 43. Tensile yield stress as a function of consolidation stress and porosity for TB toners with  $\approx 7 \mu\text{m}$  particle diameter and variable surface additive coverage (SAC) levels. (a) 20% SAC of 8 nm particle additives; (b) 100% SAC of 8 nm particle additives.

of hydrodynamic and solid fraction fluctuations is outside the scope of this paper [110, 118, 119].

### 9.1. The structure of fluidized beds of fine cohesive powders

In figure 44 we present the average porosity versus gas velocity for a typical fluidization experiment. In this kind of experiment the gas is increased quasi-statically in small steps. First, the average porosity, or equivalently the height, remains constant until we reach a velocity, called the minimum fluidization velocity, beyond which the powder layer begins its expansion until we reach the bubbling regime. Decreasing the flow, the porosity does not retrace the same path. As shown in figure 44, it follows instead the upper line. All settling experiments to be described below are performed taken as initial states fluidization states on the upper branch. The reason is that we want to erase as much as possible the influence of the initial packed state.

**9.1.1. Homogeneous fluidized bed: solid-like or fluid-like?** In the past few decades there has been a strong debate, that still persists, about the structure of gas-fluidized beds in the homogeneous fluidization regime, i.e. that between the onset of

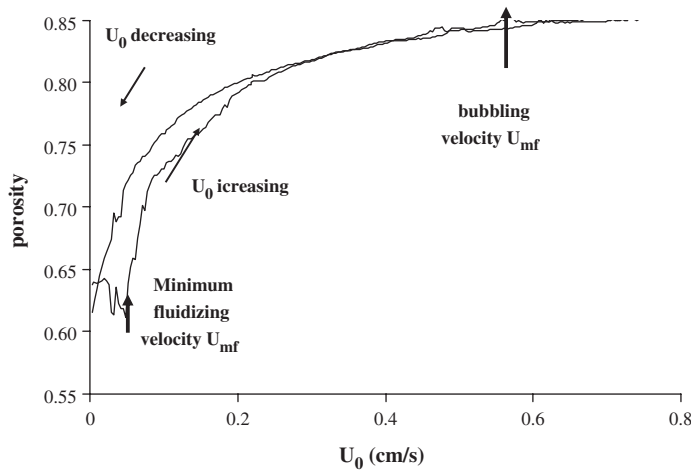


Figure 44. Hysteresis loop for porosity for a typical fluidization experiment.

fluidization and the bubbling point. The controversy dates back to the pioneer work of R. Jackson [120] who outlined that the bubbling instability, which appears when the gas velocity is increased above a critical value, was caused by the delay in the response of the particles to a change in the local concentration of solids due to the larger particle to gas phase inertia. Anderson and Jackson attributed the mechanism that tends to suppress disturbances to the gradient of an effective particulate-phase pressure [121, 122]. Yet the physical origin of this term remains unclear even nowadays. Many theoretical and numerical works have appeared that put emphasis on the hydrodynamic interaction between the solid and the fluid phases as a keystone for the stable structure of a gas fluidized bed. A common feature is to consider particle velocity fluctuations, which are assumed to control the particle-phase pressure, as the stabilizing factor [123]. However, just one decade after the work of R. Jackson, K. Rietema [124] came on with a radically different picture. He stated that interparticle cohesive forces were the responsible for the stabilization of the non-bubbling fluidized bed. These contact forces were assumed to give an effective elastic modulus to the bed that could stabilize the system against small disturbances. In that state the bed would behave like a weak solid rather than a fluid. To corroborate his thesis he showed that when the homogeneously fluidized bed was tilted the bed surface remained stable because of the existence of a certain mechanical strength. Later on, Tsinontides and Jackson [112] made a series of fluidization and de-fluidization experiments that led them to firmly support Rietema's arguments. The improvement of technology has allowed for sophisticated analyses to measure particle fluctuations in the fluidized bed. Cody *et al.* [125] derived the so-called granular temperature of the particles at the wall of a gas-fluidized bed by measuring the acoustic noise due to random particle impact at the wall. They showed that particles fluctuate in the fluidized bed and that the fluctuating kinetic energy (granular temperature) of the impacting particles on the wall depended strongly on the fluidizing gas velocity while macroscopic bubbles were not visible. Menon and Durian [126] reported on measurements by diffusion-wave spectroscopy of the

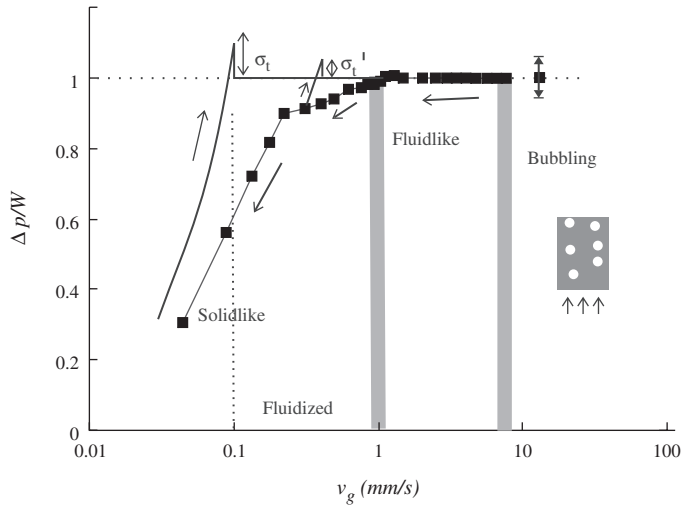


Figure 45. Gas pressure drop, made non-dimensional with the powder weight per unit area ( $W = mg/A$ ), versus gas velocity. The continuous line is the gas pressure drop when the gas velocity is increased and serves to determine the axial tensile yield stress  $\sigma_t$  of the powder. The solid boxes represent the gas pressure drop when the gas velocity is decreased.

reflection of laser light from fluidized glass beads. Surprisingly, they found no fluctuations in the interval of non-bubbling fluidization. This finding led them to the conclusion that “the uniformly fluidized state was a completely static state”. In agreement with Rietema they argued that particles in the fluidized state were held by enduring contacts and that velocity fluctuations were initiated by the instability to bubbling.

In spite of the use of these novel, non-intrusive technologies, the structure of the homogeneous fluidized bed remained quite elusive. Remarkably, in most of the experiments the powders used were composed of particles larger than 50 microns to avoid strong interparticle adhesive forces. Indeed finer particles are very cohesive and cannot usually be fluidized in the conventional sense; they form channels, or lift as a plug in the bed. For  $\sim 50 \mu\text{m}$  sized particles however the interval of uniform fluidization is very short or even absent, gas bubbles form at or slightly above the minimum gas fluidizing velocity and bed expansion is small (a maximum of 4% of the initial bed height in Menon and Durian’s work). Thus, a detailed study of the bed structure seemed quite difficult. However, the use of flow controller additives in xerographic toners ( $\sim 10 \mu\text{m}$  sized polymer particles) allows for a very wide interval of homogeneous fluidization in which the bed exhibits a considerable expansion (up to a 40% of expansion over the initial volume).

Figure 45 shows the gas pressure drop  $\Delta p$  across a fluidized bed of the xerographic toner Canon CLC700 against the superficial gas velocity  $v_g$ . It is seen that, when the gas velocity is slowly decreased from the bubbling regime,  $\Delta p$  lies below the powder weight per unit area  $mg/A$  for  $v_g < v_c \simeq 1 \text{ mm/s}$ . The consolidation stress on the powder  $\sigma_c = mg/A - \Delta p$  becomes then positive and increases as the gas velocity is further decreased. We may see, that below the bubbling point, there exists two well defined regimes. Between the bubbling velocity and a velocity of order 1 mm/s the

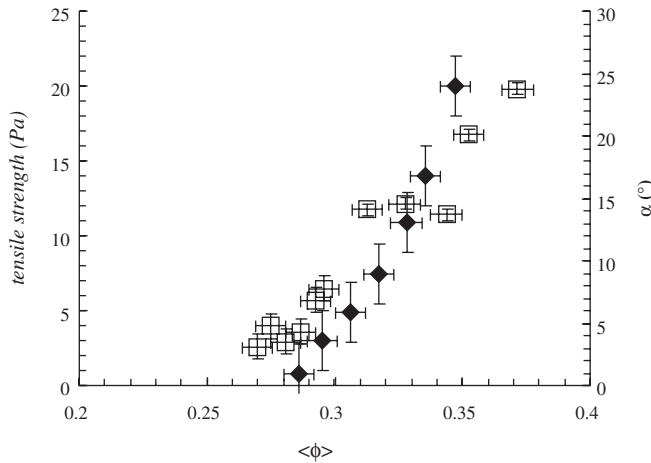


Figure 46. Uniaxial tensile yield stress  $\sigma_t$  of a fluidized bed of toner Canon CLC700 (solid symbols) and maximum angle of stability  $\alpha$  of the free surface of the fluidized bed when it is slowly tilted. For average particle volume fractions smaller than  $\langle\phi\rangle \simeq 0.28$  we measured  $\sigma_t \simeq 0$  Pa and  $\alpha \simeq 0^\circ$ .

pressure drop is equal to gravitational pressure as in fluidized beds of noncohesive powders. For gas velocities less than 1 mm/s the pressure drop lies below  $mg/A$ , implying the possible existence of network of permanent contacts able to sustain the pressure difference. A proof of the existence of this weak “solid” is obtained when we use the SPT to measure the uniaxial tensile yield stress of the fluidized bed. Figure 46 shows that the xerographic toner Canon CLC700 has a non-vanishing tensile yield stress when the average particle volume fraction  $\langle\phi\rangle$  of the fluidized bed increases above the approximate critical value 0.28 (or, equivalently, the gas velocity is smaller than  $\sim 1$  mm/s). Moreover the uniaxial tensile yield stress increases as  $\langle\phi\rangle$  is increased above 0.28. A further check of the existence of a mechanical strength could be obtained by slowly tilting the fluidized bed (see figure 46). Therefore, and in agreement with Rietema’s experiments the bed remained stable like a solid while the top surface was tilted. However a radically different behaviour was found for the fluid-like regime. The powder then appeared like a low viscosity liquid, its upper surface remaining horizontal when the container was tilted.

The transition from the fluidlike to the solidlike regime at  $\langle\phi\rangle_c \simeq 0.28$  for the toner Canon CLC700 became also clear when we investigated the response of the fluidized bed to vertical vibrations [127] (see figure 47). We found that for  $\langle\phi\rangle < 0.28$  the bed expanded reversibly as vibration amplitude was increased up to a critical height in which the fluidized state destabilized and large gas bubbles appeared rising across the bed. We rationalize this behaviour on the basis that vibrations increase the rate of collisions between aggregates, which induces their disruption and therefore improves the mixing of the gas and solid phases. On the contrary for  $\langle\phi\rangle > 0.28$  the bed behaved much like a weak granular solid [128, 129] despite that the gas velocity being the minimum fluidization gas velocity ( $v_{mf} \sim 0.1$  mm/s, see figure 29). In this solid-like regime the system relaxed irreversibly toward a more compact state by eliminating low-density metastable configurations.

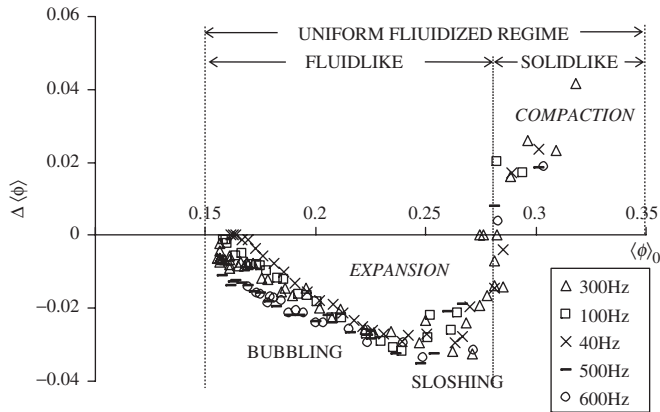


Figure 47. Average particle volume fraction increment before the onset of instability when a fluidized bed of Canon CLC700 is vertically vibrated at a fixed frequency. In the fluid like regime the bed expands while on the solid like regime the particles evolves toward a more compact configuration.

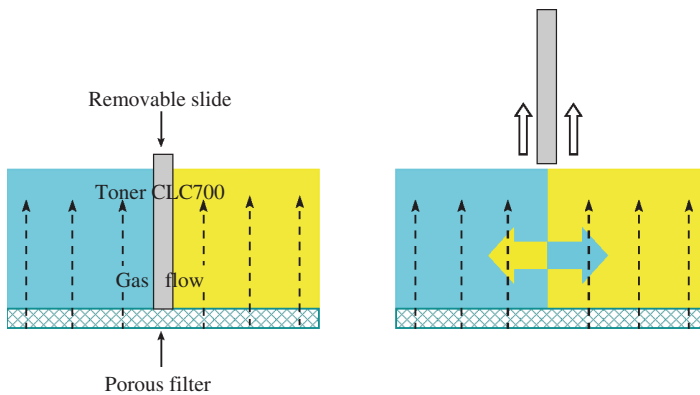


Figure 48. Blue and yellow CLC700, of essentially the same particle properties and size, are fluidized in the cell. The removable slide is taken out at  $t=0$ , and particle mobility is monitored by colour diffusion.

Measurement of the mobility of particles in the two regimes provided another additional test. The experimental cell is schematically represented in figure 48. In the solid-like regime powders do not mix, while in the fluid-like regime they display a diffusive dynamics. In this region the diffusion coefficient increases with gas velocity until the bed expansion approaches its maximum value [130].

We can assure that the fluid-like regime is really an interval of non-bubbling expansion, but, since bubbles are well developed instabilities [122], we might wonder if the fluidized bed is actually stable in this interval. From diffusion measurements [130] we obtained mean fluctuation velocities for the particles as large as two orders of magnitude greater than the gas velocity, in agreement with Cody *et al.* results [125]. Certainly any purely diffusive mechanism by which such huge velocities could

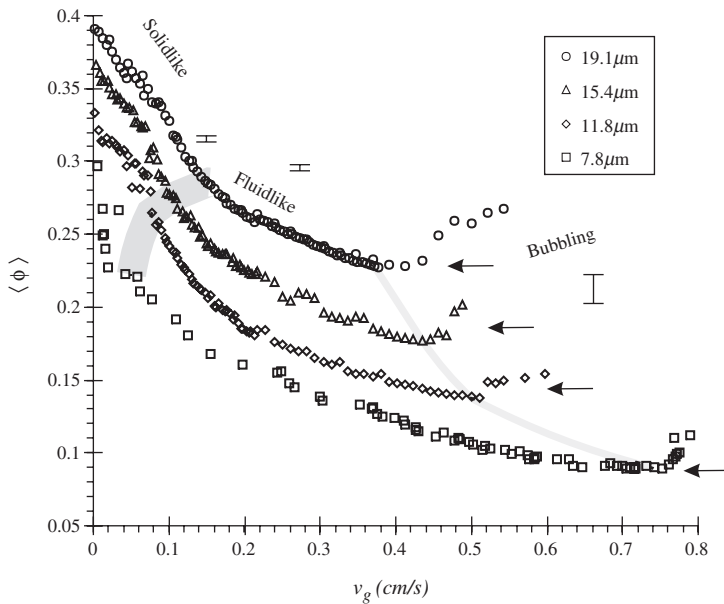


Figure 49. Average particle volume fraction as a function of the gas velocity for fluidized beds of TC toners. Toner particles differ in their average size (indicated in the inset) and have the same 32% surface Aerosil coverage.

be generated in a uniform suspension is inconceivable. Otherwise fast diffusion could arise from the growth of a hydrodynamic instability that does not develop into recognizable bubbles. Indeed we have recently identified the presence of mesoscale spatiotemporal structures and short-lived voidage instabilities [118] in close similarity with observations in liquid-fluidized beds [131]. The enhanced pressure, viscosity, and diffusivity are generated by momentum transport resulting from the mesoscale fluctuations.

**9.1.2. Fluid-like domain as a function of particle size and cohesiveness.** Following a suggestion of R. Jackson we investigated the extension of the fluid-like regime interval as a function of particle size and cohesiveness [119]. Figure 49 shows the average particle volume fraction of the powder bed as a function of the gas velocity for xerographic toners with different particle size but with the same surface area coverage of Aerosil (i.e. same interparticle attractive force). It is observed that as particle size is increased the interval of gas velocities in which the fluidized bed shows a non-bubbling fluid-like behaviour shortens. If we plot the width of this interval as a function of the cohesive granular Bond number of particles (figure 50) we predict that it should shrink to zero for  $Bo_g < \sim 10$ . A rough estimation of the van der Waals force of attraction for glass beads, equation (15), yields  $F_{vdW} \equiv Ad_a/(12z_0^2) \simeq 4\text{nN}$  (Hamaker constant  $A \simeq 1.5 \times 10^{-19}$  J, typical asperity reduced size  $d_a \simeq 0.1 \mu\text{m}$ , and minimum interparticle distance  $z_0 \simeq 4 \text{Å}$ ) while the particle density is  $\rho_p \simeq 2.5 \text{g/cm}^3$ . Following our threshold criteria we would obtain that for  $d_p > \sim 50 \mu\text{m}$  bubbling should be only restrained by the solid-like behaviour of the fluidized bed in

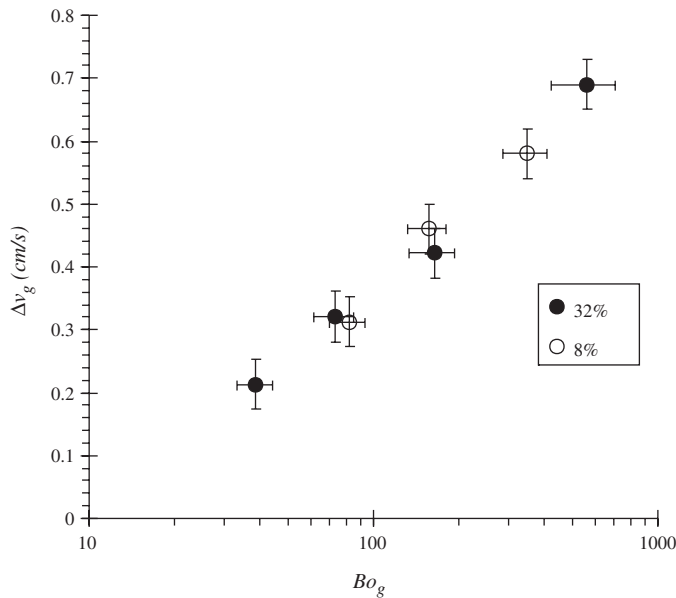


Figure 50. Extension of the interval of gas velocities over which fluidized beds of TC toners display a non-bubbling fluid-like regime against the cohesive granular Bond number. Data for toners with different particle size and different surface Aerosil coverage of the particles (indicated in the inset) are represented.

agreement with the experiments. These results must therefore put an end to arguments about hydrodynamics versus contact forces as stabilizing mechanisms. Instead of being contradictory they are rather complementary.

## 9.2. Aggregation in the fluid-like regime of homogeneously fluidized beds of fine cohesive powders

Because of the strong interparticle attractive force as compared to particle weight, toner particles are likely to be aggregated in the fluidlike regime, where there is no load on the contacts and particles interact hydrodynamically with the gas undergoing an effective diffusive process. The average size and weight of the aggregates can be obtained from settling experiments.

**9.2.1. The settling experiments.** The SPT can be employed to test the settling of powders. For each homogeneously fluidized state, the gas flow is abruptly reduced to zero, the bed collapses and the powder settles under its own weight. Figure 51a shows an example of the powder bed height measured by the ultrasonic pulser-receiver as a function of time just after shutting off the gas supply. It is seen that there is an initial constant slope that defines the initial settling velocity  $v_s$ . We have measured, for different initial superficial velocities of the fluidizing gas, the initial settling velocity of the head of the bed. Figure 51b displays  $v_s$  as a function of  $\langle\phi\rangle$  for the Canon CLC700 magenta toner (particle size  $d_p \simeq 8.53 \mu\text{m}$ ). For an explanation of the lines see below.

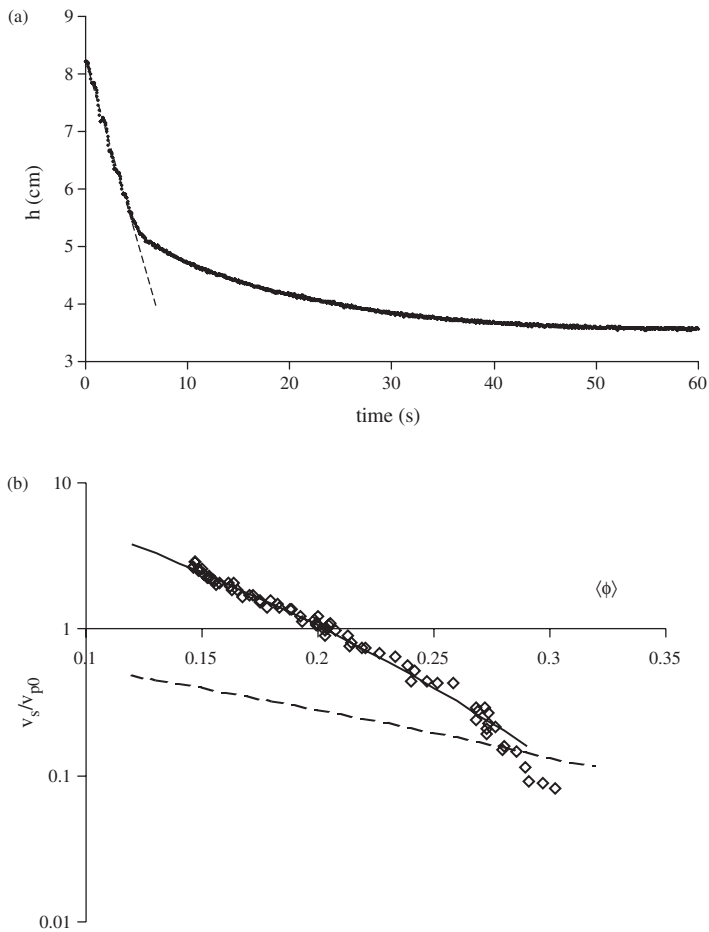


Figure 51. (a) Evolution in time of the height of an initially fluidized bed of Canon CLC700 toner. The gas velocity before shutting off the gas supply was 0.54 cm/s. (b) Initial settling velocity as function of solid volume fraction for the set of canon CLC700 toner. Dashed lines is the Richardson–Zaki prediction for isolated powder particles, continuous line is the best fit from equation (114).

**9.2.2. The fluidized bed as a suspension.** In figure 52 we may see that immediately after the gas is stopped the initial settling velocity is, within the experimental scatter, equal to the superficial gas velocity in the homogeneous fluidization phase. Thus, in the frame of reference of the superficial gas velocity our homogeneous fluidized powder can be viewed as a suspension where particles, sediment with velocity  $v_s$ . Then, the well-known phenomenological Richardson–Zaki (RZ) law [113], which gives the relationship between the settling velocity of noncohesive spheres in sedimentation  $v_s$  and the average particle volume fraction  $\langle\phi\rangle$  can be used to interpret our results. These authors obtained experimentally that for monosized spheres

$$\frac{v_s}{v_t} = (1 - \langle\phi\rangle)^n. \quad (113)$$

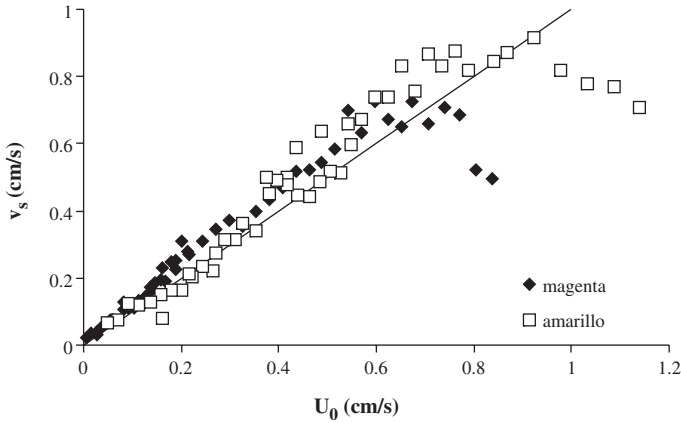


Figure 52. Superficial gas velocity versus initial sedimentation velocity of particles for CLC700 Canon toners.

where  $v_t$  is the free fall velocity of an isolated sedimenting particle, and the parameter  $n$  was  $\sim 5$  for particle Reynolds numbers  $Re_t < 0.2$  ( $Re_t = \rho_g d_p v_t / \mu$ ) which is our case. Certainly, we find in the literature a wide variation in the reported values of the Richardson–Zaki exponent. Garside and Al Dibouni [132] proposed the empirical relation  $(5.1 - n)/(n - 2.7) = 0.1 Re_t^{0.9}$ . Buscall *et al.* [133] reported on measurements of the mean sedimentation velocity of polystyrene spheres in water in the small Reynolds number range over the whole range of values of  $\langle \phi \rangle$  that fitted to the Richardson–Zaki law for  $n = 5.5$ . Later on, Rowe [134] fitted experimental data by the law  $(4.7 - n)/(n - 2.35) = 0.1 Re_t^{3/4}$ . Batchelor [135] derived theoretically for low Reynolds numbers ( $Re_t < 0.1$ ) the settling velocity in the dilute limit of hard spheres by means of a renormalization method. The result for the dilute limit,  $v_s/v_t \simeq 1 - 5.6\langle \phi \rangle$ , matched the Richardson–Zaki limit for  $n = 5.6$ . As pointed out by Snabre and Mills [136]  $n$  may be depend on neglected wall effects, residual polydispersity effects and inertial screening effects. Snabre and Mills suggest that because of long range hydrodynamic interactions a rise is expected in the exponent towards a value  $n \approx 5.6$ . Our choice is to use  $n = 5.6$  in order to conform it with Batchelor’s limit for dilute suspensions. In figure 51a the Richardson–Zaki equation for individual powder particles, assuming they are spheres of size  $d_p \simeq 8.53 \mu\text{m}$ , is displayed. This shows that there are no isolated particles, but aggregates.

**9.2.3. Estimation of average number of particles and average size of aggregates.** Let us consider that our fluidized bed consist of uniform aggregates interacting hydrodynamically with the gas as effective noncohesive spheres of radius  $R_{ag}$ . We characterize aggregates by the number of particles aggregated  $N$  and by the ratio of aggregate radius to particle radius  $\kappa = R_{ag}/(d_p/2)$ . When the gas supply to the fluidized bed is suddenly cut off aggregates settling may be well described by a modified Richardson–Zaki law for aggregates [117, 137]

$$\frac{v_s}{v_{ag}} = (1 - \langle \phi \rangle^*)^{5.6}. \quad (114)$$

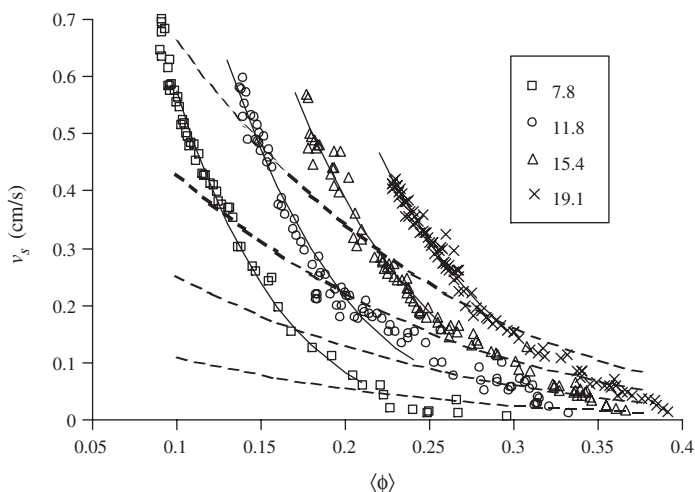


Figure 53. Initial settling velocity as function of solid volume fraction for the set of TC toners with 32% SAC. Particle size is indicated in  $\mu\text{m}$ . Dashed lines are the Richardson–Zaki prediction for isolated powder particles; the continuous line is the best fit from equation (114).

where  $v_{ag} = Nm_p g / 6\pi\eta R_{ag} = v_t N / \kappa$  is the settling velocity of an individual aggregate and  $\langle\phi\rangle^*$  is the volume fraction filled by the aggregates  $\langle\phi\rangle^* = N_{ag} (4/3)\pi R_{ag}^3 / V = \langle\phi\rangle \kappa^3 / N$ , with  $N_{ag}$  the total number of aggregates, and  $V$  the total volume.

Above  $\langle\phi\rangle_c$  aggregates are held together by enduring contacts, settling is hindered and therefore  $v_s$  decreases below the Richardson–Zaki predicted values, thus indicating we are in the solid-like regime. Using the modified Richardson–Zaki law (equation 114) to fit experimental results for  $v_s$  in the range  $\langle\phi\rangle < 0.28$  we derive  $N \simeq 96$  for the numbers of particle per aggregate and  $\kappa \simeq 5.76$  for the ratio of aggregate size to particle size. Figure 51b shows that the modified Richardson–Zaki law with these parameters is a good fit to the experimental data.

We have used the SPT to perform settling experiments on TC toners with the same interparticle attractive force and with primary particle sizes in the range from 7.8 to 19.1  $\mu\text{m}$ . In figure 53 we show the settling for these TC toners. Table 4 shows the best fitting parameters to the experimental data.

Figure 54 show photos of aggregates taken from fluidized beds of powders with particle size 7.8  $\mu\text{m}$  and 19.1  $\mu\text{m}$ , respectively.

The technique employed to take these photos makes use of the strong tendency of powder particles to adhere to a paper surface. A piece of card was slowly lowered edgewise into the fluidized bed surface so as to cleave it parallel to the gas flow path. Then, on carefully and slowly withdrawing the card, it was found to carry a replica of the fluidized powder. In these photos one clearly sees that the number of particles aggregated decreases as particle size is increased while the same value of the interparticle attractive force is maintained. Thus the number of particles per aggregate in the fluidized state depends essentially on the cohesive granular Bond number  $Bo_g$  (the ratio of interparticle attractive force to particle weight,  $W_p = mg$ ). Since the load on the contacts is zero in the fluidized state the interparticle attractive force can be

Table 4.  $d_p$ : particle size.  $N$ : average number of particles per aggregate in the fluidized bed.  $\kappa$ : average ratio of aggregate size to particle size.  $\phi_{ag} = N/\kappa^3$  internal particle volume fraction of the aggregates.  $\langle\phi\rangle_c$ : average particle volume fraction of the powder sample at the transition from fluid like to solid like regime.  $\langle\phi\rangle_c^* = \langle\phi\rangle_c \kappa^3/N$ : volume fraction filled by the aggregates at the transition. Canon powder refers to commercially available magenta Canon CLC700 xerographic toner. The rest of the powders are experimental TC toners with 32% SAC.

$d_p$ ( $\mu\text{m}$ )	$N$	$\kappa$	$\phi_{ag}$	$\langle\phi\rangle_c$	$\langle\phi\rangle_c^*$
7.8	63	5.22	0.44	0.225	0.51
11.8	23.7	3.55	0.53	0.27	0.51
15.4	12.4	2.72	0.61	0.32	0.52
19.1	9.6	2.45	0.65	0.335	0.51
8.5 (Canon)	96	5.71	0.52	0.28	0.54

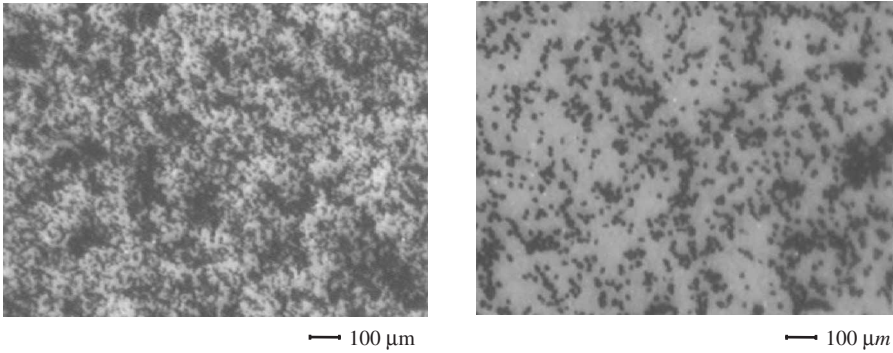


Figure 54. Left: aggregates of TC toner particles of 7.8  $\mu\text{m}$  particle size and 32% surface Aerosil coverage. Right: aggregates of TC toner particles of 19.1  $\mu\text{m}$  particle size and 32% surface Aerosil coverage.

approximated by the van der Waals force. In figure 55 we have plotted the values of  $N$  and  $\kappa$  obtained from settling experiments as a function of  $Bo_g$ . We found  $N \sim Bo_g^\alpha$  ( $\alpha \simeq 0.7$ ). The results suggest that aggregation of particles will likely occur whenever  $Bo_g > 1$  while for  $Bo_g < \sim 1$  particles will flow individually. A remarkable feature of the results is that in all the range of particle sizes investigated the fractal dimension of the aggregates  $D = \ln N / \ln \kappa$  is close to  $D = 2.5$ , which is the value given by the diffusion-limited aggregation (DLA) model of Witten and Sander in 3D [138] (aggregates are not really fractal in the strict sense of the word since their fractal scaling is only observed over finite length scales). This suggests a physical picture for aggregate growth controlled by a diffusive process and characterized by the sticking of particles to the outer zone of the aggregate (due to the strong interparticle attractive forces it is rather unlikely that the particles are able to stick to internal zones of the aggregate). As a result aggregates appear like branching structures. Such aggregates screen external fields very effectively and thus the fluid flow inside the aggregate is negligible compared to the flow outside [138]. This screening effect validates our approximation of equating the hydrodynamic radius of the aggregates to their gyration radius as it is

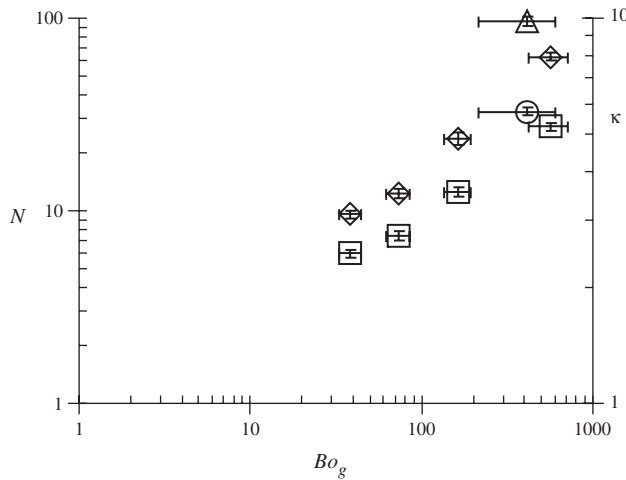


Figure 55. Average number of particles per aggregate ( $N$ : diamonds) and ratio of aggregate size to particle size ( $R/a$ : boxes) for TC toners with 32% SAC as a function of the cohesive granular Bond number. Results for Canon CLC700 toner ( $N$ : triangle and  $R/a$ : circle) are also shown.

obtained from theoretical and experimental works [139]. The size of the aggregates ( $kd_p \simeq 40\text{--}50 \mu\text{m}$ , see table 4) is approximately independent on the particle size (for a constant interparticle attractive force). The ratio of the interparticle attractive force to aggregate weight (aggregate cohesive granular Bond number)  $Bo_g^* = Bo_g/N$  turns out to be quite similar for all the powders and just slightly above one.

**9.2.4. Scaling laws for aggregates.** Since our fine particles are athermal the limits to aggregate growth in the initial fluidized state result from the interplay of gravitational and flow shear effects [140]. In order to estimate the limit size of our DLA aggregates we will adopt a similar approach to that used in ref. [141], where the limits to gelation (growth of DLCA aggregates) in colloidal aggregation are studied. In the fluidized bed the weight of the aggregate is balanced by the hydrodynamic drag from the surrounding gas, which acts mainly at the surface of the aggregate whereas gravity is a body force acting uniformly through the aggregate. This results in shear forces distributed across the aggregate limiting its size. Using a simple spring model for the aggregate [140, 141], we have  $\gamma K_{ag} R_{ag} \sim N m_p g$ , with  $\gamma$  the typical strain on the aggregate.  $K_{ag}$  is the aggregate spring constant given by  $k_0/\kappa^\beta$ , where  $k_0$  is the interparticle spring constant, and the elasticity exponent is  $\beta \simeq 3$  in the 3D case [142]. Thus the local shear force is

$$F_s \sim k_0 \gamma d_p / 2 = k_0 (\kappa^D) (m_p g d_p / 2) / [(k_0 / \kappa^3) (\kappa d_p / 2)] \sim (m_p g) \kappa^{D+2} \quad (115)$$

where we have taken into account that  $N = \kappa^D$ . Manley *et al.* [141] use a critical value, measured independently, for the maximum strain sustainable to calculate the maximum size of their DLCA aggregates. Generally, the critical shear force must be

of order of the interparticle attractive force  $F_s^{max} \sim F_a$ , which leads to  $Bo_g \sim \kappa^{D+2}$ , thus the maximum number of particles per aggregate should be

$$N = \kappa^D \sim Bo_g^{D/(D+2)} \quad (116)$$

For DLA aggregates ( $D = 2.5$ ) we obtain  $N \sim Bo_g^{0.6}$ , in fair agreement with our experimental results. Moreover, for our aggregates ( $\kappa < 10$ ) the inter-aggregate cohesive Bond number is  $Bo_g^* = Bo_g/N = \kappa^2 < 100$ , and typically less than 43 for the powders with high percentage of silica surface area coverage, i.e. inter-aggregate cohesiveness is small. We understand now why for a constant  $F_a$ , the size of our aggregates is almost independent of particle size since the criterion predicts

$$R_{ag} = \kappa d_p/2 \propto d_p^{-(D-1/D+2)} = d_p^{-(1/3)} \quad (117)$$

as can be derived using equation (116), and taking  $D = 2.5$ . We conclude therefore that particle aggregation stops when the shear force manages to equilibrate interparticle attraction.

The internal particle volume fraction of the aggregates

$$\phi_{ag} = \frac{N(4/3)\pi a^3}{(4/3)\pi R^3} = \frac{N}{\kappa^3} \quad (118)$$

is shown in table 4 for several powders. There is a tendency towards higher  $\phi_{ag}$  for larger particles, i.e. smaller number of particles aggregated (in the limit  $N \rightarrow 1$  one would expect  $\phi_{ag} \rightarrow 1$  for perfectly spherical particles). For fractal aggregates we would have the power law  $N \propto \kappa^D$  (the proportionality constant must be one if this equation holds for  $\kappa \rightarrow 1$ , see [143, 144] for a detailed discussion and measurements on the prefactor of fractal aggregates). Hence

$$\phi_{ag} \propto \frac{1}{\kappa^{3-D}} \text{ with } D = 2.5 \text{ for 3D-DLA aggregates.} \quad (119)$$

We observe in figure 56 that the intraaggregate particle volume fraction of our aggregates are well fitted by the law  $\phi_{ag} \propto 1/\sqrt{\kappa}$ . Experimental results from porosity measurements made by Hoge Kamp and Pohl on individual fragile aggregates consisting of fine cohesive powders such as milk and pectin powders (private communication) are jointly displayed in figure 56. Likewise equation (119) describes reasonably well the behaviour of the intraaggregate particle volume fraction as these fragile aggregates are artificially grown in size.

### 9.3. Compaction of the sedimented layer

Once the layer is sedimented in the SPT we compact it by means of downward flow. Figure 57 shows the relationship between the particle volume fraction and the consolidation stress for TC toners with the same surface additive coverage, 32% SAC, and varying particle size. As expected it is observed that for a given  $\sigma_c$ ,  $\langle \phi \rangle$  increases with particle size as a result of the improved flowability. We see also that the particle volume fraction increase is well fitted by a logarithmic law

$$\Delta \langle \phi \rangle = \nu \log \sigma_c \quad (120)$$

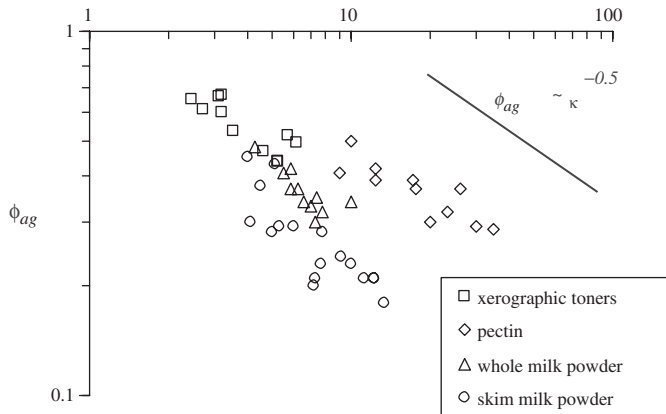


Figure 56. Internal particle volume fraction for aggregates of TC xerographic toner particles and for other fine cohesive powders (derived from direct measurements of porosity of individual aggregates reported in the literature [145]). Pectin powder consists of comminuted (pin mill) particles of median particle size of  $30\ \mu\text{m}$ . Milk powder is commercially available (Nestle) with primary particle size about  $100\ \mu\text{m}$  [146]. The continuous line represents the law  $\phi_{ag} \propto 1/\sqrt{\kappa}$  followed by DLA aggregates.

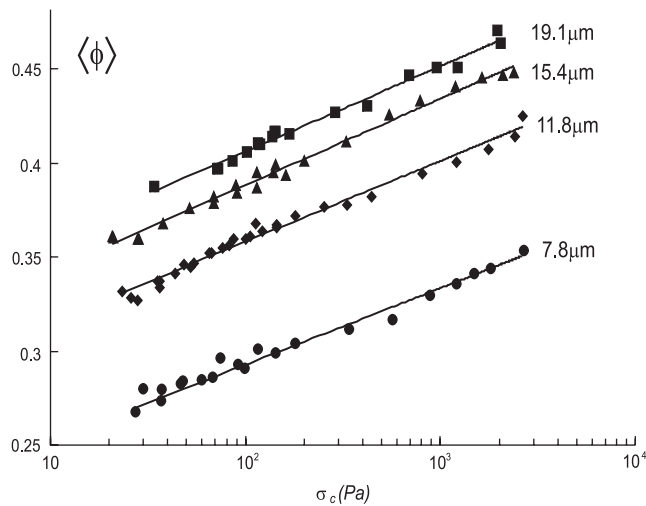


Figure 57. Particle volume fraction as a function of the consolidation stress for a set of toners with the same surface additive coverage (32%) and different particle size (indicated).

with  $\nu \simeq 0.04$  almost independent of particle size. Certainly this trend cannot be valid in the limit  $\sigma_c \rightarrow 0$  since the fluid-to-solid transition takes place at a finite value of the particle volume fraction. In order to have a clear understanding of the physical mechanisms involved on compaction our research should begin at the very transition from the fluid-like state, where there are not enduring interparticle contacts, the consolidation stress  $\sigma_c$  is zero and particles undergo an effective

diffusive process, to the solid like state, where interparticle contacts become permanent and  $\sigma_c > 0$ .

**9.3.1. Compaction under consolidations below the sample weight.** As the gas velocity in the fluid like regime is decreased there comes a point at which the aggregates become in permanent contact with each other and are suddenly arrested. This is a non-equilibrium kinetic transition from a fluid-like to a solid-like jammed state [147]. In figure 58a we have plotted the average particle volume fraction  $\langle \phi \rangle$  of a sample of Canon CLC700 as a function of the consolidation stress  $\sigma_c$ . We see that for consolidations smaller than  $\sigma_c \simeq 15$  Pa the volume fraction-stress dependence can be

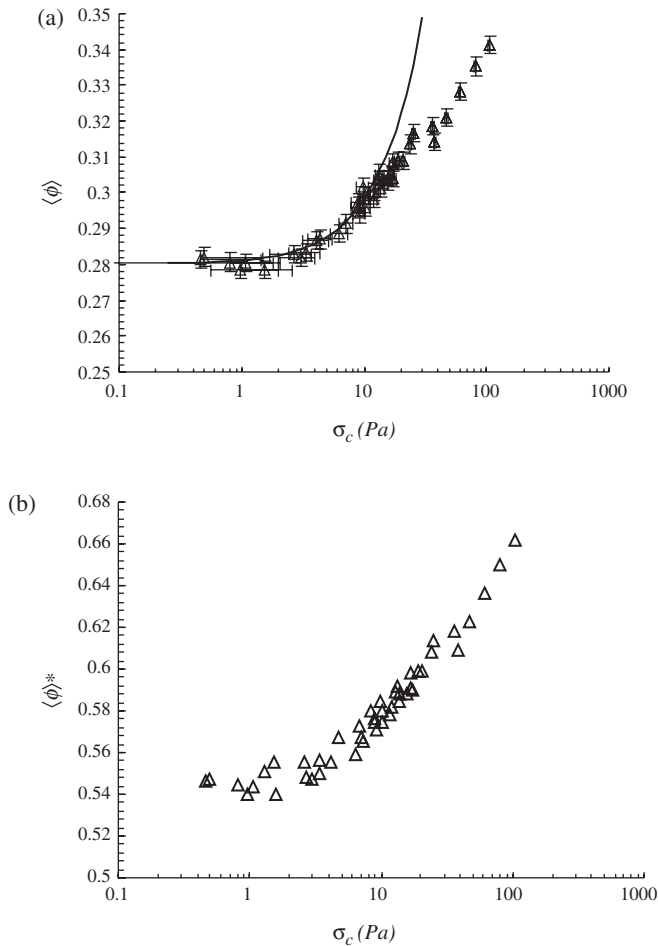


Figure 58. (a) Average particle volume fraction of the powder vs. the consolidation stress. The continuous line corresponds to the power-law  $\sigma \simeq 271(\langle \phi \rangle - \langle \phi \rangle_J)^{0.824}$  ( $\langle \phi \rangle_J \simeq 0.28$ ) that fits to the data in the range  $\sigma_c < \sim 15$  Pa. (b) Effective volume fraction filled by the aggregates of particles  $\langle \phi \rangle^* = \langle \phi \rangle \kappa^3 / N$  as a function of the consolidation stress assuming that aggregates remain unbroken as consolidation is applied. Data correspond to toner Canon CLC700.

well fitted by a power law functional form

$$\sigma_c \propto (\langle \phi \rangle - \langle \phi \rangle_J)^\delta \quad (121)$$

where  $\langle \phi \rangle_J \simeq 0.28$  is the particle volume fraction at the fluid-to-solid transition, and  $\delta \simeq 0.8$ . We measure a critical exponent  $\delta$  that in most cases is close to one irrespective of powder cohesiveness. Examples of this critical-like behaviour near the jamming transition are also found in different granular systems such as hard sphere granular materials, attractive colloids, foams, and emulsions [148]. The quasilinear increase of the stress with  $\langle \phi \rangle$  found in our experiments agrees with the experimental results on soft particle granular systems such as foams and emulsions and indeed our weak aggregates should behave like soft rather than hard particles. Also, the small value of  $\delta$  as compared with the one predicted for systems of hard spheres undergoing Hertzian interaction ( $\delta \simeq 1.5$  [149, 150]) results from the slow increase of  $\langle \phi \rangle$  in the vicinity of the jamming transition, which is due to the effectiveness of inter-aggregate cohesive forces to counteract small consolidations.

According to our sedimentation experiments  $\kappa \simeq 5.71$  and  $N \simeq 96$  for the toner Canon CLC700 magenta. Figure 58b is a plot of  $\langle \phi \rangle^*$  as a function of the consolidation stress for this toner. In the initial quasistatic regime  $\langle \phi \rangle^* \sim 0.54$ , which is a value slightly smaller than the random loose packing of noncohesive hard spheres at the limit of zero gravitational force ( $\phi_{RLP} \simeq 0.56$ , see ref. [6]), and it is in accordance with the reported value for spheres of equivalent size,  $\kappa d_p \simeq 50 \mu\text{m}$  [151]. Obviously aggregates, viewed as effective low cohesive spheres, cannot pack in values of  $\langle \phi \rangle^*$  above the random close packing limit of noncohesive hard spheres ( $\phi_{RCP} \simeq 0.64$ , see ref. [152]). We must admit therefore that aggregates must be disrupted, at least partially, for consolidation stresses such that  $\langle \phi \rangle^* > 0.64$ , which typically corresponds to  $\sigma_c < \sim 100 \text{ Pa}$ .

In figure 59a data of  $\langle \phi \rangle$  corresponding to TC toners with the same surface additive coverage (32%) and with different particle size are presented. These results show clearly that the ability of the toner to pack in more compact assemblies increases as particle size is increased. We see again the cross-over from the power-like behaviour typical of soft spheres to the logarithmic trend typical of soils. For these powders however the change of behaviour occurs for larger critical stresses ( $\sigma_{cY} \simeq 20 \text{ Pa}$ ) as we might expect according to their larger cohesiveness. Remarkably the data for the different toners collapse into a single curve when we plot the effective volume fraction of the aggregates  $\langle \phi \rangle^*$  vs.  $\sigma_c$  (see figure 59b). As previously shown, the size of aggregates  $\kappa d_p/2$ , is more or less independent of the primary particle size for a given interparticle attractive force and therefore we would have systems of equivalent effective spheres that behave similarly and independently of the toner primary particle size. Since the internal particle volume fraction of the aggregates decreases as  $\kappa$  increases it turns out that the average particle volume fraction of the powder decreases as the primary particle size is decreased as seen in figure 59a. This means that aggregates made of smaller particles are less compact. It is interesting to notice that, according to our expectations, the less cohesive aggregates of TC toners with 64% SAC jam in a larger volume fraction  $\langle \phi \rangle^* \simeq 0.57$  (see figure 59b), which is close to the typical value found for suspensions of noncohesive spheres [153]. Moreover the range of values obtained of  $\langle \phi \rangle^*$  are in agreement with Kong and

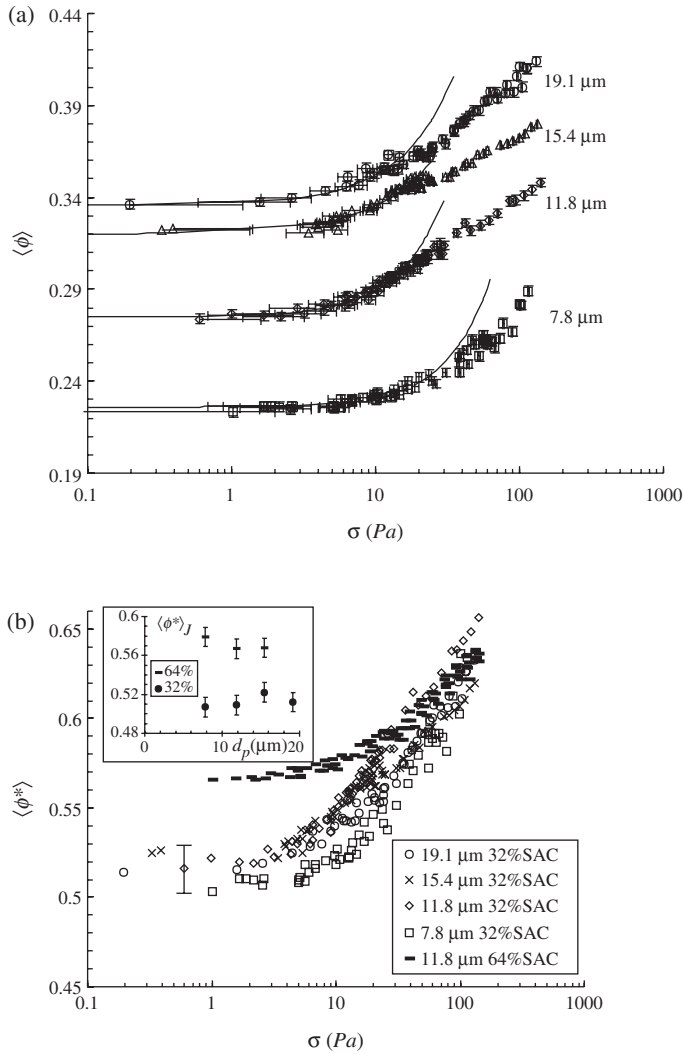


Figure 59. (a) Average particle volume fraction in the solidlike state vs. the consolidation stress. The continuous lines represent the power-law  $\sigma = \alpha(\langle \phi \rangle - \langle \phi \rangle_J)^\beta$  that fit to the data in the range  $\sigma < \sim 20$  Pa. (b) Effective volume fraction filled by the aggregates of particles  $\langle \phi \rangle^* = \langle \phi \rangle \kappa^3 / N$  as a function of the consolidation stress assuming that aggregates remain unbroken as consolidation is applied. Data for TC toners of different particle size (indicated in the inset) and with approximately 32% of surface Aerosil coverage. In (b) we have also included data for a TC toner of diameter 11.8  $\mu\text{m}$  with 64% SAC.

Lanutti simulations results on the loose packing fraction during the fall of aggregates having low inter-aggregate adhesion strengths [154]. As in the case of Canon CLC700 toner we must admit that aggregates must be disrupted, at least partially, for consolidation stresses such that  $\langle \phi \rangle^* > 0.64$ , which typically corresponds to  $\sigma_c < \sim 100$  Pa.

**Nature of the aggregates:** From our estimations we have inferred that the fractal dimension of our aggregates is near to DLA fractal dimension. We now revisit this conclusion. We have performed two independent experiments, settling and compaction, which has given us two quantities,  $v_s(\phi)$  and  $\langle\phi\rangle_J$ , while the number of variables is three,  $\kappa$ ,  $D$  and  $\langle\phi^*\rangle_J$ . Since the latter has to be equal to the packing fraction of aggregates at jamming, it is  $\langle\phi^*\rangle_J \simeq 0.53$ . Using  $\langle\phi\rangle = (N/\kappa^3)\langle\phi^*\rangle_J \simeq 0.53\kappa^{D-3}$  we may express  $v_s$  as a function of  $\kappa$  and  $D$ . Letting  $k$  arbitrary, it may be shown that no fit is possible for  $D \leq 2.3$ , which gives a lower bound for the fractal dimension of our aggregates. This excludes the possibility of having DLCA aggregates (diffusion limited cluster aggregates), as their fractal dimension would be approximately given by 1.78.

**9.3.2. Compaction of powders subjected to consolidations above the sample weight.** We will show that the initial distribution of voids rules the compaction process, and that these voids are mainly determined by the internal particle volume fraction of aggregates that are jammed at the initial unconsolidated state [155]. Figure 60 shows the data for low consolidation stresses along with the data for high consolidations for Canon CLC700 and TC32-8 toners. Clearly both sets of data are satisfactorily connected. We see in figure 60 that for  $\sigma_{cY} > \sim 15$  Pa,  $\langle\phi\rangle$  increases with the applied stress according to the same logarithmic law, equation (120) as TC toners. The logarithmic trend initiated at  $\sigma_{cY} \sim 15$  Pa is maintained in the regime of large consolidations. According to figure 59b and for consolidations typically larger than  $\sim 100$  Pa aggregates cannot behave as individuals since  $\langle\phi\rangle^*$  is larger than the random close packing of noncohesive hard spheres at this level of stress, which is physically unacceptable. Therefore the rearrangement process must

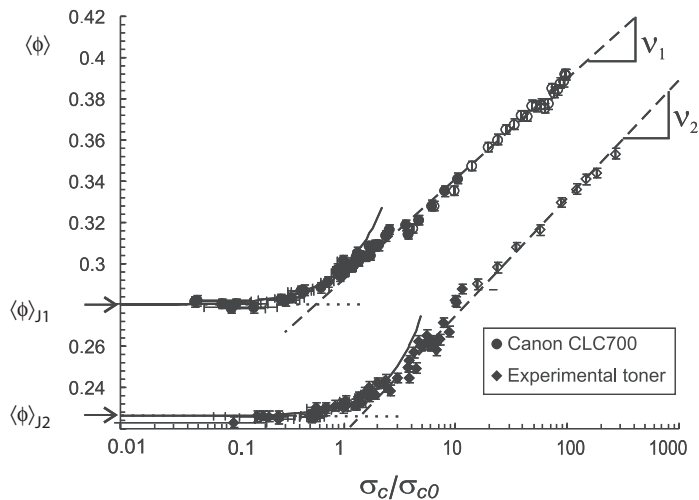


Figure 60. Average particle volume fraction as a function of the consolidation stress. Data correspond to commercial toner Canon CLC700 (100% SAC) and to TC32-8 with similar particle size. The lines correspond to the power-law  $\sigma_c \propto (\langle\phi\rangle - \langle\phi\rangle_J)^\beta$  that fits to the data in a range  $\sigma_c < \sim \sigma_{c0} = 10$  Pa, and to a logarithmic fit  $\langle\phi\rangle - \langle\phi\rangle_J \simeq \nu \log \sigma_c$  that fits to the data in the range  $\sigma_c > \sim \sigma_{c0}$ . (low consolidations, solid symbols; large consolidations, open symbols.)

be also characterized by the breaking of interparticle contacts within the aggregates. For our micrometric sized particles the disruption of aggregates occurs therefore at loads ( $\sim 100$  Pa) considerably smaller than the typical ones ( $\sim$  MPa) for nanometric particles that are found in ultrafine powders such as ceramics.

Experiments on the compaction of soils subjected to large consolidations date back to the beginning of the last century. Walker [156] fitted his results by the phenomenological logarithmic law:

$$\Delta \frac{1}{\langle \phi \rangle} = -\lambda \log \frac{\sigma_c}{\sigma_{c0}} \quad (122)$$

where  $\Delta(1/\langle \phi \rangle) = 1/\langle \phi \rangle - 1/\langle \phi \rangle_0$ , with  $\langle \phi \rangle$  the average particulate solid fraction,  $\sigma_c$  is the applied pressure,  $\sigma_{c0}$  is the lowest available experimental consolidation stress (usually above 10 kPa),  $\langle \phi \rangle_0$  is the corresponding average solid fraction and  $\lambda$  (compression index) is an empirical parameter. This equation has been traditionally used in civil engineering both in triaxial and oedometric tests [157, 158]. Sometimes the void ratio ( $e \equiv \langle e \rangle / (1 - \langle e \rangle)$ ) is preferably used in equation (122) instead of the void index [159]. Equation (122) applies well when compaction is driven by rearrangement of the particles and seems to be solely founded on the geometric constraints in a 3D assembly of grains [160].

From statistical mechanics considerations, equation (122) and the value of the compression index  $\lambda$  have been predicted for noncohesive spheres assuming that it is the filling of the large pores, comprising the interparticle space, what generates the irreversible evolution of the void distribution. A central point of the derivation was to postulate that the distribution of pores obeys an exponential law as suggested by the principle of maximum entropy [161]. Recently an experimental analysis by means of X-ray microtomography of a granular packing undergoing compaction has confirmed that compaction is governed by the reduction of the number of large pores which are statistically distributed along a broad exponential tail [162]. Equation (122) has also served to describe the behaviour of some cohesive granular materials for which  $\lambda$  depends on adhesive forces through their influence on the local rearrangement of grains. Compaction for clays contained in soils subjected to low pressures revealed that  $\lambda$  increases almost linearly with the void ratio of the unconsolidated powder [163]. A similar trend is obtained for the compaction of ultrafine (particle size  $< \sim 1 \mu\text{m}$ ) metallic powders of different cohesiveness [164] (larger void ratio implies larger cohesiveness). Indeed, the role of cohesiveness can be twofold. On one hand attractive forces lead to the formation of stable arches which would increase the number of large pores. From this point of view cohesiveness should weaken the structure under compression and therefore the compression index should increase as obtained. On the other hand if adhesive forces oppose strongly particle rearrangement we might expect an increased yield stress of the assembly and therefore a decrease of the compression index. In these studies the initial state is arbitrarily taken as the state corresponding to the minimum consolidation, typically 10 kPa. Here we will study the influence on compaction of the true initial state, i.e. the unconsolidated jammed state.

We plot in figure 61 the inverse of particle volume fraction,  $1/\langle \phi \rangle$ , versus the dimensionless consolidation stress,  $\sigma_c/\sigma_{c0}$  ( $\sigma_{c0} \simeq 10$  Pa), for TC toners with 32%

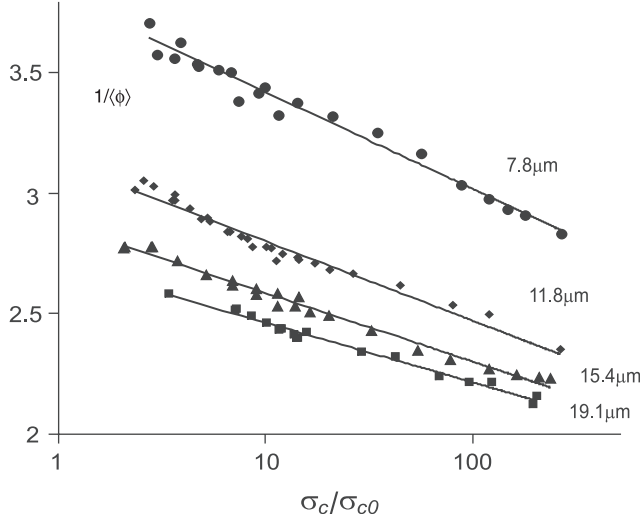


Figure 61. Inverse of particle volume fraction versus the consolidation stress, where lines are the logarithmic fits to the data,  $\Delta(1/\langle\phi\rangle) = \lambda \log \sigma_c/\sigma_{c0}$ .

surface area coverage and varying sizes. These data are well fitted to a logarithmic law

$$\frac{1}{\langle\phi\rangle} - \frac{1}{\langle\phi\rangle_J} = -\lambda \log \frac{\sigma_c}{\sigma_{c0}} \quad (123)$$

with  $\langle\phi\rangle_J$  the particle volume fraction at jamming. As  $\lambda$  depends on cohesion we look for a power law fit of  $\lambda$  versus  $Bo_g$  (calculated assuming that attraction arises from van der Waals forces  $F_{vdW}$ ). This gives  $\lambda \simeq 0.1Bo_g^{0.21}$ . The increase of compression with cohesiveness has been reported in the engineering literature [164, 165]. Moreover, the extrapolated value for  $Bo_g = 1$  is  $\lambda = 0.1$ , matching the typical value reported for noncohesive granular materials ( $Bo_g < \sim 1$ ) such as sand [163].

**Scaling law for the compression index:** Let us discuss the experimental scaling law found with  $Bo_g$ . To a first approximation

$$\Delta(1/\langle\phi\rangle) \simeq [\partial(1/\langle\phi\rangle)/\partial \log \hat{\sigma}_c]_0 \log \hat{\sigma}_c \simeq -(1/\langle\phi\rangle_J)^2 \nu \log \hat{\sigma}_c, \quad (124)$$

where  $\nu \simeq [\partial\langle\phi\rangle/\partial \log \hat{\sigma}_c]_J$ , and we have used  $\hat{\sigma}_c = \sigma_c/\sigma_{c0} \simeq 1$  and  $\langle\phi\rangle \simeq \langle\phi\rangle_J$  at the initial state. Thus  $\lambda \simeq (1/\langle\phi\rangle_J)^2 \nu$ . Let us write  $\langle\phi\rangle_J = \langle\phi\rangle_J^* \phi_{ag}$ , where  $\langle\phi\rangle_J^*$  is the volume fraction filled by the aggregates at jamming, and  $\phi_{ag} = N/\kappa^3 = \kappa^{D-3}$  is the particle volume fraction within the individual aggregates. Then  $\lambda \simeq (1/\langle\phi\rangle_J^*)^2 \nu Bo_g^{(6-2D)/(D+2)} = (1/\langle\phi\rangle_J^*)^2 Bo_g^{0.22}$ , where we have used the aggregate size limit criterion ( $Bo_g \simeq \kappa^{D+2}$ ), and  $D = 2.5$ . Aggregates behave as low cohesive effective spheres and thus  $\langle\phi\rangle_J^*$  is almost independent on  $Bo_g$ . Using the values of  $\nu \simeq 0.4$ , and  $\langle\phi\rangle_J^* \simeq 0.53$  for the TC toners with 32% SAC (see figure 59b) we would predict  $\lambda \simeq 0.14Bo_g^{0.22}$  in good agreement with the experimental scaling law. In summary

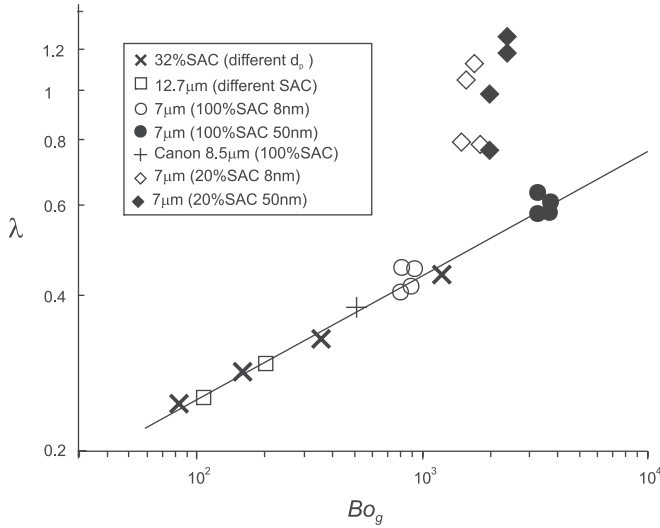


Figure 62. Compression index versus cohesive granular Bond number for toners with different particle size and %SAC (indicated). The van der Waals force is used for all toners. The continuous line is the power law fit for toners with  $SAC \geq 30\%$  ( $\lambda \propto Bo_g^{0.24}$ ).

it expresses the fundamental role of the size and fractal structure of jammed aggregates on the distribution of voids to be filled in the compaction process.

We plot in figure 62 the data for  $\lambda$  versus  $Bo_g$  for all measured toners (for which we admit that attractive forces are van der Waals forces). The new data for toners with  $SAC \geq 30\%$ , also fits to the predicted scaling law.

**The case of highly cohesive toners:** The case of highly cohesive powders ( $SAC < 30\%$ ) needs additional discussion. In figure 62 we included data for highly cohesive toners (TB's with approximately 20% SAC) using  $F_a = F_{vdw}$  to calculate  $Bo_g$ . The data deviates clearly from the scaling law, showing unexpectedly large values of  $\lambda$  that indicate the existence of large aggregates. Moreover, in spite of the similar values of  $Bo_g$  (same particle weight and same van der Waals force:  $A \simeq 10^{-19}J$ ,  $d_a \simeq 0.2\mu m$ ), there is a clear difference between the compression indexes of toners with different gel. The reason is that these powders retain memory of their initial packed state, i.e. the fluidization process during the bubbling regime is unable to break the powder to its constituent particles. Gas flow breaks the layer in large aggregates. Settling experiments on Canon CLC700, compressed to 30 kPa in the packed state, shows that the aggregates have a number  $N \simeq 320$ , much larger than the corresponding number in aggregates obtained from packed states subjected to much lower compressions.

To estimate the cohesive granular Bond number for these highly cohesive toners we may use on the hand the scaling in size given by the criterion for aggregate settling in fluidization, and on the other hand the information we have from the jammed state. We estimate the aggregate limit size from  $Bo_g = \kappa^{D+2}$ , with  $D \simeq 2.5$  according to our sedimentation experiments. Next, we obtain  $\kappa$  from the ratio  $\langle \phi \rangle_J / \langle \phi \rangle_J^* = \kappa^D / \kappa^3$ , where  $\langle \phi \rangle_J$  and  $\langle \phi \rangle_J^*$  are the experimentally measured solid

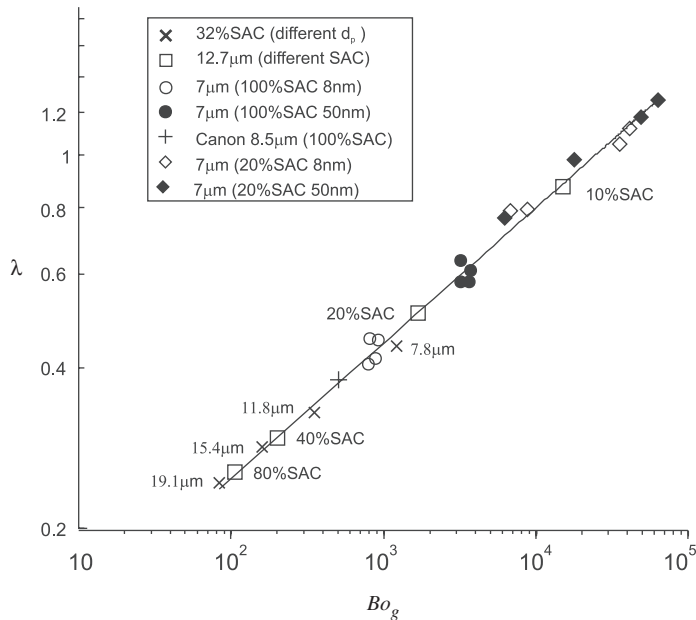


Figure 63. Compression index versus cohesive granular Bond number for toners with different particle size and %SAC (indicated).  $Bo_g$  is calculated assuming that the interparticle attractive force in fluidization is the van der Waals force for SAC > 30%, while we take into account memory effects for toners with SAC < 30% (see text). The continuous line represents the power law fit for the whole set of toners ( $\lambda \propto Bo_g^{0.25}$ ).

fractions for particles and aggregates in the unconsolidated jammed state. Notice that  $\langle \phi \rangle_J^*$  is almost constant, but  $\langle \phi \rangle_J$  shows large variations. The estimated cohesive granular Bond number following this procedure is similar to the one estimated using the attractive van der Waals forces only for the low cohesive toners (those with a SAC above 30%). On the contrary, the new estimation for the highly cohesive toners is substantially larger. Figure 63 includes the data for 20% SAC and 10% SAC toners with the new estimation of  $Bo_g$ , showing a good fit to the predicted power law. We can also discriminate now between the compression indexes for 20% SAC toners in base of the hardening effect due to the cross-linking agent added to the parent polymer.

**Remark on the fluidization of nanopowders:** It is well known that nanopowder aggregates may have a tensile strength in the range of kPa to MPa. Therefore nanopowders will not be decomposed to their constituent particles by fluidizing the powder, a fact confirmed by experiments [166, 167]. What we should expect, instead, is that in the homogeneous fluidized state, these preexisting aggregates will in turn aggregate, possibly in a multistage process. Therefore, the Richardson–Zaki law and the scaling laws discussed here for fine powders have to be modified for nanopowders to take into account this hierarchical aggregation process. In [168] a simple two-stage process of aggregation for nanopowders is considered.

#### 9.4. Micromechanics of granular materials

One essential step before proceeding to correlate the AFM and SPT measurements is to establish the relationship between the micromechanics of contacts and the bulk properties. For a system of hard monodisperse spherical particles with a random isotropic packing the relation [169, 170]

$$F = \frac{\pi d_p^2}{\phi k} \sigma \quad (125)$$

was established between the contact force  $F$  and the hydrostatic stress  $\sigma$ , where  $d_p$  is the particle diameter,  $k$  is the coordination number, which is defined as the average number of contacts per particle, and  $\phi$  the volume solid fraction. This relationship depends on the assembling procedure, the particle properties and the interparticle forces. Thus, for a given solid fraction, there is no unique coordination number. However, for a continuous process of compaction, the average coordination number is a monotone increasing function of  $\langle\phi\rangle$ . Here, we use the expression

$$k = \frac{\pi}{2} (1 - \langle\phi\rangle)^{3/2} \quad (126)$$

which is practically equal to the expression  $k = 1.61(1 - \phi)^{-1.48}$  given by Nakagaki and Sunada [171] (as mentioned in Suzuki *et al.* [172]), and discussed in detail by Jaraiz *et al.* [173]. Computer simulations of the compaction process of an assembly of cohesive particles [151, 174], yield almost identical results to equation (125) in the range of solid volume fractions  $\phi \in \sim [0.2, 0.5]$  which are of interest in our powders.

The effect of an anisotropic distribution of contacts has been considered in reference [175]. From the energy conservation principle, the stress tensor  $\sigma_{ij}$  and the interparticle contact force  $F_i$  can be related by the equation

$$F_i = \sigma_{ij} n_k A_{kj} \quad (127)$$

where  $n$  is the unit vector parallel to the contact orientation, and  $\bar{A}$  is the inverse of the fabric tensor  $F_{ik}$  of the material, which for the case of spherical particles is written in terms of the contact angular distribution  $P(\Omega)$  (normalized to unity) in the form [175]:

$$F_{ik} = \frac{3\phi k}{\pi d_p^2} \int P(\Omega) n_i n_k d\Omega \quad (128)$$

provided that all contacts with the same orientation carry the same contact force. Under this hypothesis, and if the contact angular distribution and the coordination number are known, equations (127) and (128) can be used to derive contact forces from stresses.

For an oedometric test along the  $z$  axis, and neglecting the wall effect, the stress tensor has the general form:

$$\sigma_{ij} = \sigma_h \delta_{ij} + (\sigma_z - \sigma_h) \delta_{i3} \delta_{j3} \quad (129)$$

with  $h$  denoting the horizontal (radial) coordinate.

Numerical simulations [176] have shown that the principal directions of the fabric tensor coincide with the principal directions of the strain-rate tensor, which has cylindrical symmetry around the  $z$  axis in an oedometric test. Therefore the

fabric tensor and the contact angular distribution must have cylindrical symmetry around the  $z$  axis and reflection symmetry in the  $xy$  plane. The contact angular distribution can be expanded in a series of spherical harmonics having this symmetry. For the sake of simplicity we consider only the two first terms in the series to estimate the effect of the anisotropy in the distribution of contact directions:

$$P(\Omega) = N(Y_{00} + \zeta Y_{20}) \quad (130)$$

with  $N$  the normalizing factor, and  $\zeta$  is the factor that takes into account the anisotropy.

In the measurements of interparticle contact forces using the AFM we checked that the centres of the probe and substrate particles were approximately collinear in the vertical direction. This means that the vertical direction was close to the normal to the surfaces of the area of contact. Then, and provided that  $\sigma_h < \sigma_z$ , using equations (128), (129), (130) in equation (127) the (average) value of the normal force  $F_n$  acting on a contact can be approximated by

$$F_n = F_i n_i = \frac{\pi d_p^2}{\phi k} \sigma_z \left(1 + \frac{2}{\sqrt{5}} \zeta\right)^{-1} \quad (131)$$

In the absence of anisotropy,  $\zeta = 0$ , we recover equation (125). In a 2D system  $\zeta \sim 0.1$  [176] which means only a 10% of decrease in the contact force. Hopefully this correction will not be much higher for a 3D system.

The effect of polydispersity has also been addressed in the literature. Tsoungui *et al.* [177] give the mean normal force  $F$  on a contact as a function of the external stress  $\sigma$  for a polydisperse 3D system

$$F = \frac{\pi d_p^2}{\phi k} \sigma \beta \quad (132)$$

where  $\beta = 1$  for a monodisperse packing, thus recovering equation (125). The parameter  $\beta \geq 1$  was shown to be a function of the variation of the density of the packing with the mean particle volume. For a bimodal distribution in a 3D system,  $\beta$  presents a maximum value of 1.5 for a small particle volume fraction close to 0.2, but, in general, displays a weak dependence on the particle size ratio. Our experimental powders are rather monodisperse and we expect that this correction will be minor. Thus, the effects of anisotropy and polydispersity are the inclusion of a multiplicative factor close to unity in equation (125). In what respects to the irregularities of particles surface we have not found any realistic approach that deals with this effect and we will ignore it.

A serious drawback of the Rumpf formula, and its generalization to aggregates (see next section) is that force chains in the powder are neglected. The existence of force chains is well established in coarse granular media made of hard particles. On the contrary for fine, soft and highly compressible powders there is a fundamental lack of knowledge about the existence of strong force chains. Some experimental results for soft compressible coarse powders show that stresses are more ‘‘Gaussian’’ distributed [178]. Also Makse *et al.* [4] point out that for high loads (larger particle deformations) the force distribution crosses from exponential to Gaussian. Certainly our aggregates are extremely soft particles, and the powder highly compressible.

Thus we should expect no chain forces at very low consolidations. For higher loads, although our particles are soft compared to glass beads and deform plastically, it is unclear whether we can neglect force chains. Unfortunately, our experimental results are not precise enough to rule them out, and clearly this merits further investigation. Here, and in order to establish a semiquantitative relationship between interparticle forces and packing, we take the simplistic approach that the contact force distribution is Gaussian, and that it is meaningful to define an average force per contact.

### 9.5. Correlation between the AFM and SPT measurements

In figure 14 we presented the results for TA005 and several TB toners. However, TB toners of such small size and low additive concentration display a quite inhomogeneous fluidization. Therefore, we restrict our discussion to the TA005 toner.

In figure 64 we plot the estimation of contact forces and its comparison with the theoretical results from the modified Maugis–Pollock theoretical predictions for TA005 with two values of the Young’s modulus. We have chosen the value of 3.5 GPa in Part I, which is a typical value for polymers (this is why we have also chosen the same value of Young’s modulus for TB toners). The value,  $E_{TA} = 3.5 \text{ GPa}$  fits better the AFM median values, while  $E_{TA} = 6 \text{ GPa}$ † fits better the AFM average values (the same is true for the elastoplastic model). Probably, the true value of the Young’s modulus may be in between since there is a fraction of polymer–silica contacts that may affect the value of Young’s modulus of the bare polymer.

For very low consolidations, the estimation of interparticle forces by means of the Rumpf formula for isolated particles is systematically below the AFM measurements. Then, it is clear that at very small consolidations we must take into account the existence of aggregates. In figure 65 we present the sedimentation velocity of the top free surface of the fluidized bed measured just after turning off the gas supply as a function of the initial particle volume fraction. Note that for  $\langle \phi \rangle > 0.17$  the cloud of data is mostly above the phenomenological law, which might be due to the presence of large solid-like regions that accelerate the settling process as compared to a perfectly homogeneous fluidized state. The large variations of sedimentation velocity near the settling hampers any reliable measure of the number and size of the aggregate. Thus we have to turn to the solid volume fraction versus gas velocity and compaction curves for this toner. We may see from figure 66a, that the fluid-to-solid transition takes place at  $\langle \phi \rangle_J \simeq 0.21$ . Since the data of figure 66b can be fitted to the equation  $\langle \phi \rangle - \langle \phi \rangle_J \simeq \lambda \log(\sigma_c/\sigma_{c0})$ , we obtain  $\sigma_{c0} \simeq 20 \text{ Pa}$ . Assuming that for this highly cohesive toner  $\langle \phi \rangle^* \simeq 0.5$  (see figure 58b) we have for the ratio of aggregate to particle radius  $\kappa$ , and for the number of particles  $N$  in the aggregate

$$\kappa = \left( \frac{\langle \phi \rangle_J^*}{\langle \phi \rangle} \right)^{1/(3-D)} \quad N = \kappa^D \quad (133)$$

---

†In our previous work [116], we took for Young’s modulus,  $E_{TA} = 6 \text{ GPa}$ .

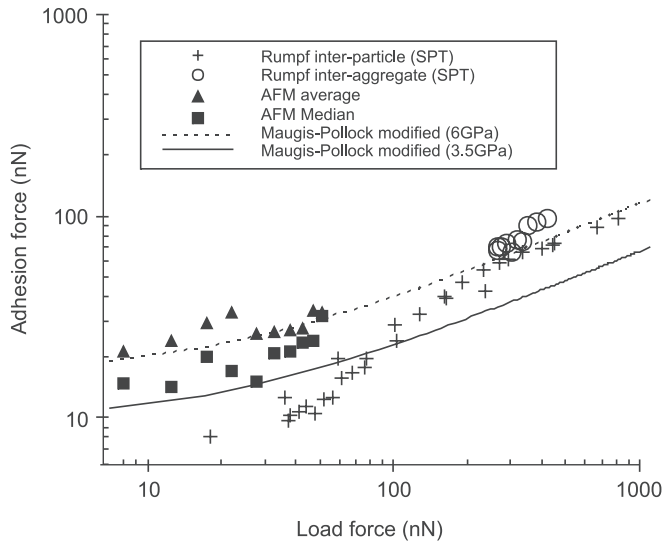


Figure 64. The contact forces for TA005 estimated by means of the Rumpf formula, equation (124) for particles, the modified Rumpf equation (134), for aggregates, and their comparison with the modified Maugis–Pollock equation (86), for Young’ modulus 3.5 and 6 GPa. Also represented are the median and the average of AFM measurements.

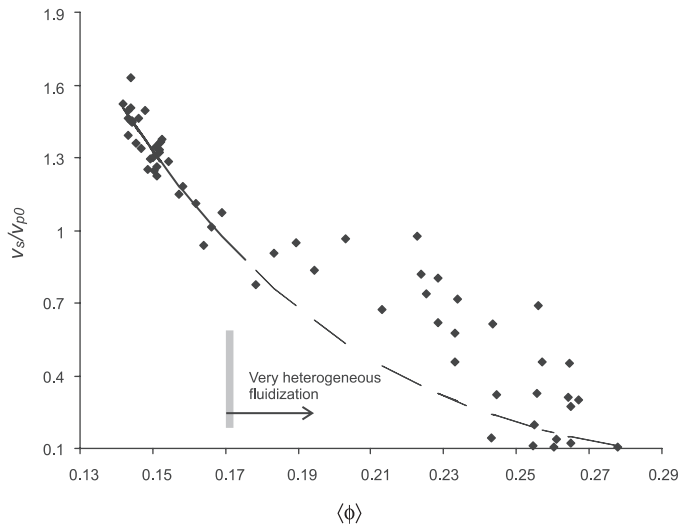


Figure 65. Sedimentation velocity of the top free surface of the fluidized measured just after turning off the gas supply as a function of the initial particle volume fraction for toner TA005.

Given that the sedimentation curve is quite sensitive to the value of  $D$ , we fit the points in the homogeneous fluidization regime (see figure 65), to equation (114) with the values of  $N$  and  $\kappa$  given above. We obtain in this way  $D \simeq 2.52$ . Finally,  $N \simeq 96.5$ , and  $\kappa \simeq 6.12$ . Assuming that aggregates are minimally disrupted below

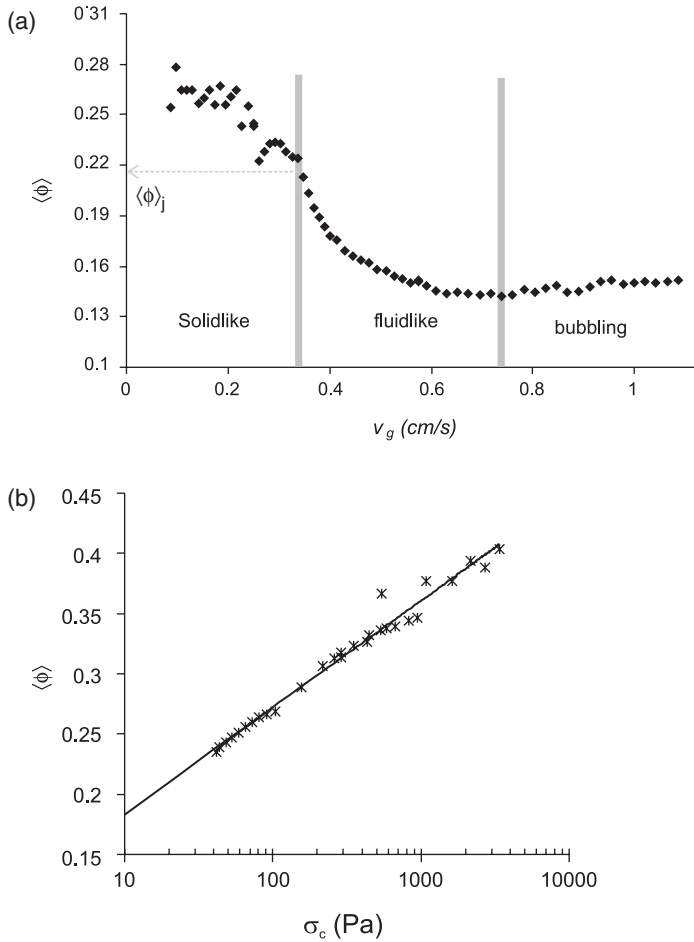


Figure 66. (a) Particle volume fraction as a function of the fluidizing gas velocity for TA005 toner. The vertical line indicate the limits of the different fluidization regimes. (b) Particle volume fraction in the solid-like regime as a function of the consolidation stress. The continuous line is a logarithmic fit to the data.

$\phi^* \leq 0.64$  we estimate their interparticle force generalizing the Rumpf formula in the form

$$F_a^* \sim \sigma_t \frac{\pi d^{*2}}{\zeta^* \langle \phi \rangle^*} = \sigma_t \frac{N}{\kappa} \frac{\pi d_p^2}{(\pi/2) \left(1 - \frac{\kappa^3}{N} \langle \phi \rangle\right)^{-3/2} \langle \phi \rangle} \quad (134)$$

We have plotted in figure 64 the interaggregate forces as circles. It is seen that this forces are a better fit to the theoretical curve than the interparticle forces in this region of very low consolidations. On the other hand, the Rumpf formula for isolated particles fit better the results for consolidations above 300 Pa thus indicating a considerable aggregate disruption, and that the load tends to be uniformly

distributed among contacts between isolated particles. Given that the particles are not perfectly spherical nor monodisperse, the uncertainties in the values of the average asperity ratio and the mechanical properties, and our neglect of force chains, our comparison can be at most semiquantitative. However the results are encouraging. To progress in this direction we need better defined systems, both at the grain and the bulk level.

### 9.6. Contact forces in the bulk: qualitative comparison with theory

The Rumpf equation (125) provides us with a reasonable estimate of the average contact forces provided that consolidation stresses are large. We present in figure 67 the adhesive contact forces as a function of the square root of load contact force. As shown in figure 67a, the trend for high normal forces is as predicted by formula (86). Also, the slope of the line does not change, since  $E, H$ , and  $w$  are the same for all these toners. Moreover, the forces at low consolidations also merge in a single curve. In figure 67b, we present the data for the TA toners (same particle size  $12.7\ \mu\text{m}$ , and different surface area coverings). Again, the estimated pull-off contact force is linearly related to the square root of the pull-on-force. The slope now differs for the different toners as the hardness and surface area change as a function of silica content, with the slope decreasing as the latter increase. The value of the slope for powders with the lowest additive coverage ( $SAC < \sim 10\%$ ) is  $\gamma \simeq 4\sqrt{nN}$  in good accordance with the theoretical slope calculated from equation (80) (for polymer–polymer contacts ( $\gamma \simeq 3.6\sqrt{nN}$ ) using  $w \simeq 0.07\ \text{J/m}^2$ ,  $\nu \simeq 1/3$ ,  $E \simeq 6\ \text{GPa}$ ,  $H \simeq 0.3\ \text{GPa}$ ). As with respect to the slope for high silica coverage it is difficult to compare the experimental data with a theoretical prediction since a theory on the hardness and Young modulus of the contact between hard nanoparticles resting on a relatively soft substrate does not exist.

Concerning the effect of size of silica nanoparticles additive, in figure 68 we represent the estimated interparticle adhesion force as a function of the interparticle load force for TB46 and TB48 toners. We observe that for small loads the adhesion force increases with the size of the additive ( $F_c < \sim 100\ \text{nN}$ ) according to the van der Waals dependence on the radius at contact and to the fraction of polymer–silica contacts. Since for large loads the contact is dominated by the hardness, we expect that interparticle forces will be smaller for TB48 as its hardness is smaller according to its aggregate surface area covering compared to TB46.

The effect of gel content may be seen in figure 69 where it is represented the pull-off force  $F_t$ , as a function of the pull-on force  $F_c$  for toners with same  $SAC$ , and identical particle size. It is apparent from the figure that gel content increases slightly the hardness of the contact, thus decreasing the slope of the fitted straight line.

## 10. Flow regime boundaries in cohesive powders

In general, granular materials display four different flow regimes: plastic behaviour, inertial flow, fluidized flow and entrained flow. Particle size,

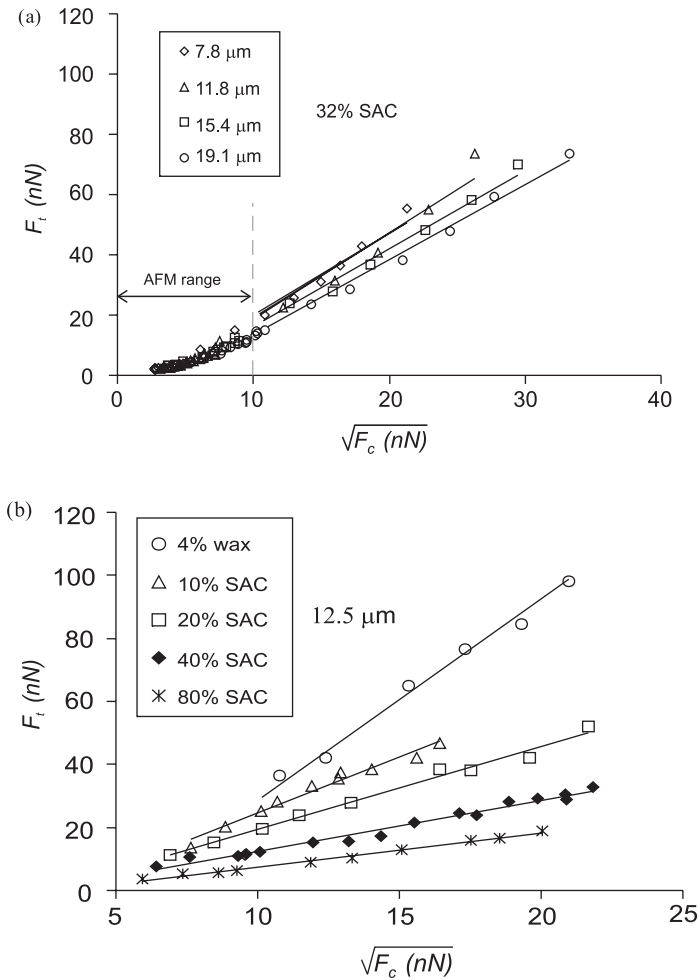


Figure 67. (a) Adhesive contact force  $F_t$  (previously denoted as  $F_a$ ) as a function of the square root of the load contact force  $F_c$ . (a) Toners with the same surface silica additive coverage (32%) but with different particle size. (b) Toners with the same particle size (12.7  $\mu\text{m}$ ) but with different surface silica additive coverage. Data from experiments on a toner with wax additive are also shown. The straight lines are the best linear fits to the data.

particle density, cohesiveness and gas flow determine which of these types of behaviour occur.

- The plastic regime is characterized by a small spacing between neighbouring particles. Velocities are small or zero and the stresses are independent of velocity for simple geometries.
- In the inertial regime the stresses are due to the transport of momentum by interparticle collisions. The spacing between particles is much smaller than the particle size, but greater than in the plastic regime. We note that the interstitial fluid plays no part in most inertial flows.

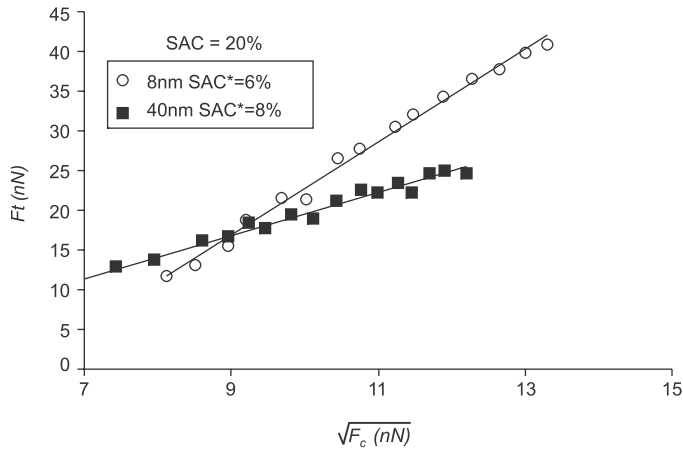


Figure 68. Adhesive contact force  $F_t$  as a function of the square root of the load contact force  $F_c$  for TB46 and TB48 toners (they have approximately 20% SAC, and 8 nm and 40 nm silica nanoparticles additive respectively). The approximate real surface area coverage of additive due to aggregation of silica nanoparticles (SAC\*) is indicated in each case. The straight lines are the best linear fits to the data.

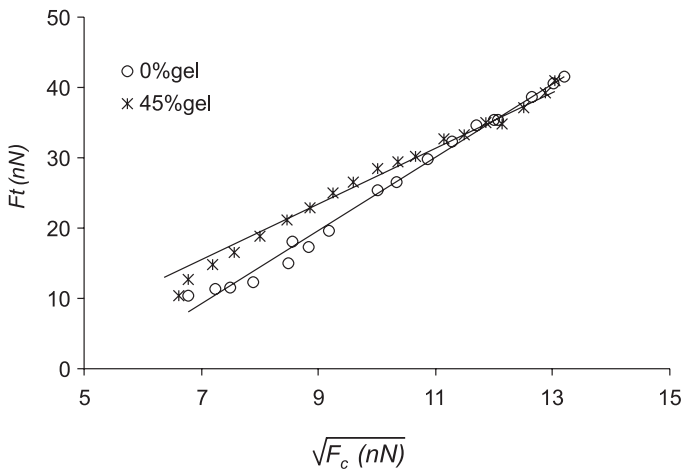


Figure 69. Adhesive contact force  $F_t$  as a function of the square root of the load contact force  $F_c$  for toners with 0% and 45% of cross-linking agent (gel). The straight lines are the best linear fits to the data.

- Powders are capable of being fluidized by gas flow provided their cohesiveness is not too great. In this regime the interparticle distance is of the same order of magnitude as the particle size. The interstitial fluid is the agent of transfer of momentum between particles, and fluid velocity determines the stresses in the material.

- A fourth regime is that of entrainment, or suspension of the particles by the gas. In this case the distance between particles is much greater than the size of the particles, the mean velocity of the material is close to the fluid velocity and the interaction between particles is negligible. This is the case in a dust storm or a sand storm.

For each regime of granular behaviour there is a dominant mechanism that determines the order of magnitude of the stresses in the bulk, and the transitions between the various flow regimes can then be obtained by comparing the magnitude of these stresses.

For the plastic regime, in the absence of external stresses, the dominant stress is  $\rho gh$  ( $\rho$  is the bulk density of the powder,  $g$  the acceleration due to gravity and  $h$  the vertical length scale of the sample).

For the fluidized regime the pressure drop across the powder at the point of fluidization is given by  $\Delta P = \rho gh + \sigma_t$ . This pressure drop is also given by Carman's equation [111],  $\Delta P/h = E\eta U(1 - \langle e \rangle)^2 \langle e \rangle^{-3} d_p^{-2}$ , where  $\eta$  is the gas viscosity,  $U$  the gas velocity,  $\langle e \rangle$  is the average void fraction of the bed and  $E \sim 180$ . Equating these relations we obtain the gas velocity needed for fluidization. For noncohesive powders ( $\sigma_t \simeq 0$ ) the minimum velocity for fluidization is proportional to the square of the particle diameter. When particles are very fine the interparticle cohesive forces become dominant and the minimum velocity for fluidization becomes less dependent on the particle diameter. Referring to figure 70 the line A in the diagram represents

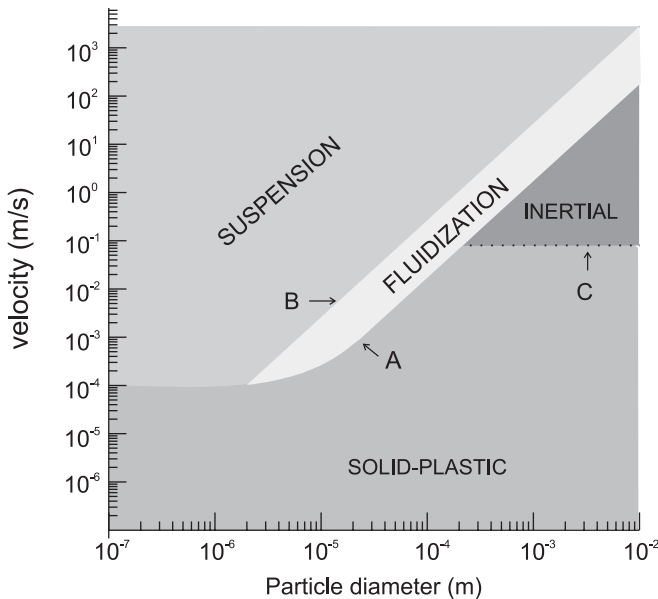


Figure 70. Phase diagram determining the transition between flow regimes as a function of particle diameter.  $\rho_p = 1000 \text{ kg m}^{-3}$ ,  $\eta = 2 \times 10^{-5} \text{ kg m}^{-1} \text{ s}^{-1}$ ,  $E = 180$ ,  $g = 10 \text{ m s}^{-2}$ ,  $\delta = 8d_p$ ,  $P = 1 \text{ Pa}$  (we assume a free moving slab, thickness  $\sim 1 \text{ mm}$ , of toner),  $h = 10 \text{ mm}$ ,  $e = 0.5$ . Line A has been using values for the cohesiveness taken from experimental measurements for toner TA04.

the minimum velocity for fluidization as a function of particle diameter (obviously the exact location of this line depends on the cohesiveness of the particles [179]). The horizontal continuation of A on the left side of the figure represents the case of very cohesive powders, and the location of this boundary depends on the mechanical properties of the particles and on the size of the asperities. The void fraction ( $\epsilon$ ) changes with the ratio of particle weight to interparticle cohesive force, i.e. the cohesive Bond number. Particles above  $3 \times 10^{-5}$  m in diameter pack near the random close packing limit ( $\epsilon \simeq 0.45$ ) and therefore the slope of line A does not depend on the diameter for these large particles. Below this value ( $\epsilon$ ) increases to a maximum of about 0.8 (near the random ballistic aggregation limit). This will slightly change the shape of line A for very fine particles. We have limited the size of our particles to 0.1  $\mu\text{m}$  in the diagram as probably these estimations are not applicable to nanoparticles.

The suspension regime is the upper limit to the fluidization regime. This limit, denoted by line B, is given by Stokes' drag,  $U = \rho_p g d_p^2 / 18\eta$ , where  $\rho_p$  is the particle density (gas density has been neglected). This value of gas velocity,  $U$ , is the minimum required to levitate a particle, and except for very fine powders ( $d_p \leq 10^{-6}$  m) this velocity is greater than the minimum velocity for fluidization. Thus line B represents the minimum velocity for particle entrainment or suspension. As may be seen, there is a critical value of particle diameter for which the suspension velocity equals minimum fluidization velocity. Therefore, if the powder consists of particles of diameter less than this critical size, fluidization by gas flow is impossible as the particles will become entrained by the flow, rather than fluidized.

For the inertial regime, according to Bagnold [180], the stresses in granular flow are proportional to the square of the velocity gradient,  $\tau \sim \rho_p d_p^2 (U/\delta)^2$ , where  $\delta$  is the extent of the shear layer and  $U$  is the velocity decrement of the material across the shear layer (we assume that in the inertial case the gas is swept along by the fast-moving particles so that  $U$  represents both gas and particle velocities). According to Savage and Hutter [181] the transition between plastic and inertial regimes is given by  $\rho_p d_p^2 U^2 / (P\delta^2) \geq 0.1$ , where  $P$  is the total normal stress; the shear layer thickness  $\delta$  scales with  $d_p$  so this transition is represented by a horizontal line such as C in figure 1.

We see from this part of the flow regime diagram that for particles above  $10^{-4}$  m diameter, as flow velocity is increased, the transition from plastic to inertial behaviour is followed at higher flows by a transition to the fluidized regime. In contrast to this, particles between  $10^{-5}$  m and  $10^{-4}$  m do not exhibit inertial behaviour, but undergo a direct transition to fluidization. Below  $10^{-5}$  m fluidization becomes increasingly sensitive to interparticle cohesion; it also becomes very sensitive to initialization conditions, i.e. to the uniformity and degree of consolidation of the powder. For these reasons the flow regime diagram has to be understood in a semiquantitative way, but the general trends of the lines indicate the approximate relationships between particle size and velocity for the various regimes and transitions.

In the vertical axis of the diagram is the interstitial gas velocity. The gas flow may be due to a gas injected through a gas distributor as in fluidized beds, to entrapped air because of avalanching processes, to air entrainment by moving solid bodies inside the powder as blades in rheometers, inner rotating hollow tubes like in tube

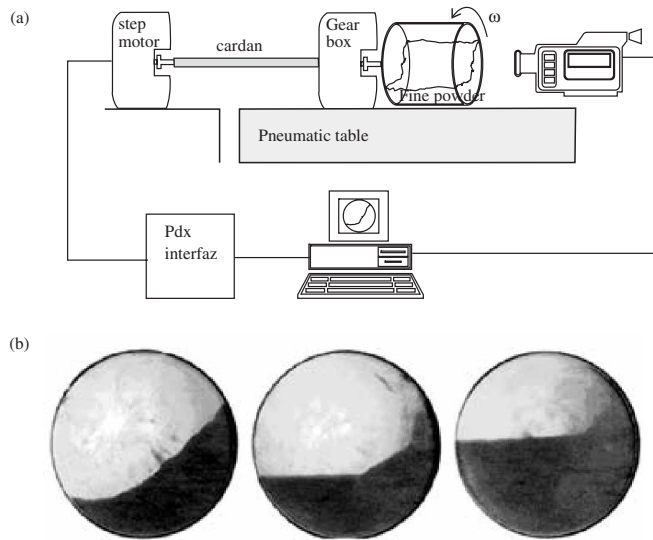


Figure 71. (a) Experimental setup of the rotating drum: (b) Profiles of TA04 toner in a rotating drum for three different angular speeds:  $\omega = 10$  rpm;  $\omega = 45$  rpm;  $\omega = 100$  rpm from left to right. The material is fully fluidized when the free surface is horizontal.

feeders, blades in photoreceptor cleaning equipment, or through impact like in bottle feeders. As an illustration we show in figure 71 the behaviour of a fine powder in rotating drums, which is qualitatively different from the classical behaviour of sand in the same apparatus. At low angular speeds the material experiments periodic avalanches as sand do, but as we increase the drum velocity the gas is entrained inside the powder and fluidization of the avalanching material becomes possible. For an analysis of this fluidization process we refer the reader to [19].

## 11. Conclusion

In the first part of this review we have examined van der Waals interparticle forces, and how they change as function of particle size, local radii of curvature, and surface energy. The response of the particle depends also in the mechanical particle properties (Young's modulus and yield compressive stress). These theoretical considerations are essential to understand the experimental results obtained with the AFM measurements between two particles. From theory is evident that particles of different sizes but similar surface topographies exhibit similar attractive interparticle forces, as have been confirmed by different AFM experiments. We have shown that plasticity may play a fundamental role as it may explain the observed increase of the attractive forces with the applied load in polymer particles (in a single contact). We have developed a simple semi-analytical model for the elastic-plastic contact that yields reasonable agreement with the experimental results, and covers the gap between purely elastic models and fully plastic ones.

Next we have described a new apparatus, called the Sevilla powder tester (SPT). We have shown its usefulness as a powerful characterization and research tool for fine cohesive powders. We have used this apparatus to investigate mechanical properties of the powders as solids. We have presented extensive measurements of the tensile stress as a function of applied load and average powder density. The theories discussed in the first part allow us to understand the experimental measurements at least qualitatively.

In order to establish a relationship between the AFM and SPT measurements for the powder solid we have investigated the structure of the settled powder layer in the fluidized bed technique. This required a detailed research on the structure of the fluidized bed (again using the SPT). These studies on the structure of the fluidized bed have allowed us to resolve an old controversy on the solid-like versus fluid-like nature of the homogeneously fluidized beds below bubbling. From our experiments it is clear that both regimes may exist for particles below 50 microns approximately. For larger particles we go directly from the solid-like regime to bubbling.

By means of settling experiments we have determined the average size, number of particles and fractal structure of the aggregates as function of interparticle forces present in the homogeneously fluidized beds of fine powders. This knowledge has been essential to understand the evolving structure of the sedimented layer through increasing compaction. The knowledge of this structure was necessary to establish a semiquantitative relationship between interparticles forces and bulk behaviour.

The results obtained so far allow us to clarify that there is no a direct translation between interparticle forces and the results obtained by means of shear or tensile testers. This absence of direct correlation has been considered as puzzling for many researches. Here we have shown that a proper understanding of this relationship solves this apparent discrepancy.

We finish by showing the most important effect that we have discovered: the absence of inertial regimes with negligible gas interaction in fine powders. This far reaching result makes powders qualitatively different from coarse granular materials, and it is the most important single fact to be taken in account when designing industrial devices for handling, transport and mixing of fine powders.

The relationship between attractive interparticle forces and bulk properties has been the motivation for all the research presented here. In trying to clarify this relationship we have learned that these forces affect all powder processes in an essential way. However we have been only able to illustrate this relationship in a qualitative manner, and at most in a semiquantitative way for the simplest situations at hand.

To improve our understanding of fine powders we need to make progress in various directions. We need to improve the contact mechanics theories of two particles including plasticity. We need to develop continuum theories to describe bulk powder behaviour. A deeper understanding of the micromechanics of granular materials is necessary to relate this contact problem to bulk behaviour both in the solid and in the fluidized state. We need to understand the transition from a discrete to a continuous description of the powders and the relation between the average quantities and their fluctuations, in "solid state", in plastic flows and in fluidization. The complexity of these problems needs a concerted effort from the

academy and the industry in order some day to have a predictive theory for powder behaviour.

### Acknowledgements

Many of the experimental results described here are the result of a joint work of two teams (a Xerox team and a University of Seville team) that has lasted for more than a decade. In the Xerox team has participated Keith Watson, Frank Genovese and Mike Morgan from the Wilson Center for Research and Technology based in Webster, NY, US. In the University of Sevilla team have participated Alberto T. Perez, Antonio Ramos, Jose Manuel Valverde, Miguel Angel S. Quintanilla and myself. This work has also greatly benefited from the collaboration with P. Mills an expert in suspensions. I would like to acknowledge the continued financial support of Xerox Foundation, of Xerox Corporation (that has also provided us with model materials), of the regional government of Andalusia and the central government of Spain. Finally I would like to acknowledge the University of Seville that granted me a sabbatical leave during the academic year 2003–2004, and to the Institute of Problems for Mechanical Engineering, of the Russian academy of Sciences in Saint Petersburg, and in particular to his Director D.A. Indeitsev, that has kindly hosted me for the most part of that year. This gave me the opportunity on the one hand to have the time to write this paper, and on the other hand to have carried fruitful discussions with Russian experts in the field of mechanics as I. Goryacheva, P. Zhilin, E. Grekova, A. Krivtsov, and I. Blekhman among others.

### References

- [1] H. Schubert, *Powder Tech.* **37** 105 (1984).
- [2] L. Massimilla and G. Donsi, *Powder Tech.* **15** 253 (1976).
- [3] J.D. Bernal, *Nature* **183** 141 (1959).
- [4] H.A. Makse, D.L. Johnson and L.M. Schwartz, *Phys. Rev. Lett.* **84** 4160 (2000).
- [5] G.D. Scott, *Nature* **188** 908 (1960).
- [6] G.Y. Onoda and E.G. Liniger, *Phys. Rev. Lett.* **64** 2727 (1990).
- [7] H.A. Mizes, *J. Adhesion Sci. Technol.* **8** 937 (1994).
- [8] D. Maugis and H.M. Pollock, *Acta Metall.* **32** 1323 (1984).
- [9] S. Froeschke, S. Kohler, A.P. Weber and G. Kasper, *Aerosol Sc.* **34** 275 (2000).
- [10] M.N.A. Karlsson, K. Deppert, L.S. Karlsson, M.H. Magnusson, J.-O. Malm and N.S. Srinivasan, *J. Nanoparticle Research* **7** 43 (2005).
- [11] L.-O. Heim, J. Blum, M. Preuss and H.-J. Butt, *Phys. Rev. Lett.* **83** 3328 (1999).
- [12] C. Thornton and S.J. Antony, *Powder Tech.* **109** 179 (2000).
- [13] J. Tomas, in *Particles on Surfaces 8: Detection, Adhesion and Removal*, edited by K.L. Mittal (VSP, Utrecht, 2003).
- [14] H. Krupp, *Adv. Colloid Interface Sci.* **1** 111 (1967).
- [15] B. Gady, D. Schleaf, R. Reifenberger, D. Rimai and DeMejo, L. P., *Phy. Rev. B* **53** 8065 (1996).
- [16] S. Herminghaus, *Adv. Phys.* **54** 221 (2005).
- [17] J.P.K. Seville, C.D. Willett and P.C. Knight, *Powder Tech.* **113** 261 (2000).
- [18] M. Kwauk, J. Li and D. Liu, *Powder Tech.* **111** 3 (2000).
- [19] A. Castellanos, J.M. Valverde and M.A.S. Quintanilla, *Phys. Rev. E* **65** 061301 (2002).
- [20] D. Geldart, *Powder Tech.* **7** 285 (1973).

- [21] L. Svarosky, *Powder Testing Guide: Methods of Measuring the Physical Properties of Bulk Powders* (Elsevier Applied Science, Oxford, 1987).
- [22] F.M. Borodich and D.A. Onishchenko, *Int. J. Solids Struct.* **36** 2585 (1999).
- [23] K. Rietema, *The Dynamics of Fine Powders* (Elsevier, UK, 1991).
- [24] J. Israelachvili, *Intermolecular and Surface Forces* (Academic Press, New York, USA, 1992).
- [25] N Yu and A. Polycarpou, *J. Colloid Interface Sci.* **278** 428 (2004).
- [26] E. Barthel, *J. Colloid Interface Sci.* **200** 7 (1998).
- [27] Ross, S. and L.D. Morrison, *Colloidal Systems and Interfaces* (Wiley-Interscience, New York, 1988).
- [28] D. Maugis, *Contact, Adhesion and Rupture of Elastic Solids* (Springer-Verlag, Berlin, 2000).
- [29] K. Kendall, *Molecular Adhesion and its Applications* (Kluwer Academic/Plenum Publishers, New York, 2001).
- [30] K.L. Johnson, *Contact Mechanics* (Cambridge University Press, Cambridge, 1985).
- [31] C. Argento, A. Jagota and W.C. Carter, *J. Mech. Phys. Solids* **45** 1161 (1997).
- [32] S. Eichenlaub, A. Gelb and S. Beaudoin, *JICIS* **280** 289 (2004).
- [33] E.R. Beach, G.W. Tormoen, J. Drelich and R. Han, *JICIS* **247** 84 (2002).
- [34] A.J. Forsyth and M.J. Rhodes, *J. Colloid Interface Sci.* **223** 133 (2000).
- [35] H.B.G. Casimir and D. Polder, *Phys. Rev. D* **73** 150 (1948).
- [36] Th.G.J. Overbeck in *Colloid Science*, Vol. 1, edited by H.R. Kruyt (Amsterdam, Elsevier, 1952), p. 266.
- [37] J. Gregory, *J. Colloid Interface Sci.* **83** 138 (1983).
- [38] B. Derjaguin, *Kolloid-Z* **69** 155 (1934).
- [39] B.V. Derjaguin, V.M. Muller and Toporov, P. Yu., *J. Colloid Interface Sci.* **53** 314 (1975).
- [40] R.S. Bradley, *Phil. Mag.* **13** 853 (1932).
- [41] K.L. Johnson, K. Kendall and A.D. Roberts, *Proc. R. Soc. Lond. A* **324** 301 (1971).
- [42] D. Tabor, *J. Colloid Interface Sci.* **58** 1 (1976).
- [43] V.M. Muller, V.S. Yushchenko and B.V. Derjaguin, *Coll. Surf.* **77** 91 (1983).
- [44] J.A. Greenwood, *Proc. R. Soc. Lond. A* **453** 1277 (1997).
- [45] J.Q. Feng, *Colloids Surf. A* **172** 175 (2000).
- [46] D. Maugis, *J. Colloid Interface Sci.* **150** 243 (1992).
- [47] J.A. Greenwood and K.L. Johnson, *J. Phys. D* **31** 3279 (1998)1998.
- [48] W.R. Chang, I. Etsion and D.B. Bogy, *J. Tribology* **109** 257 (1987).
- [49] W.R. Chang, I. Etsion and D.B. Bogy, *J. Tribology* **110** 57 (1998).
- [50] W.J. Stronge, *Impact Mechanics* (Cambridge University Press, Cambridge, 2000).
- [51] Y. Zhao, D.M. Maietta and L. Chang, *Trans. ASME* **122** 86 (2000).
- [52] Mesarovic, S.Dj. and Fleck, N.A., *Int. J. Solids Struct.* **37** 7071 (2000).
- [53] L. Vu-Quoc, X. Zhang and L. Lesburg, *Int. J. Solids Struct.* **38** 6455 (2001).
- [54] C.-Y. Wu, *Finite Element Analysis of Particle Impact Problems*, PhD thesis Birmingham, Aston University (2001).
- [55] L. Kogut and I. Etsion, *J. Appl. Mech.* **69** 657 (2002).
- [56] C. Thornton and Z. Ning, *Powder Tech.* **99** 154 (1998).
- [57] L.Y. Li, C.Y. Wu and C. Thornton, *Proc. Inst. Mech. Engrs., Part C: J. Mech. Eng. Sci.* **216** 421 (2002).
- [58] M. Barquins and D. Maugis, *J. Mechanique Theorique et Appliquee* **1** 331 (1982).
- [59] S.K. Roy Chowdhury, N.E.W. Hartley, H.M. Pollock and Wilkins M.A., *J. Phys. D, Appl. Phys.* **13** 1761 (1980).
- [60] L. Kogut and I. Etsion, *J. Colloid Interface Sci.* **261** 372 (2003).
- [61] A.J. Ishlinsky, *PMM J. Appl. Math. and Mech.* **8** 170 (1944).
- [62] S.Dj. Mesarovic and Johnson, K.L., *J. Mech. Phys. Solids* **48** 2009 (2000).
- [63] J.Y. Walz, *Adv. Colloids Interfaces* **74** 119 (1998).
- [64] U. Sindel and I. Zimmermann, *Powder Tech.* **117** 247 (2001).
- [65] S.C. Hodges, J.A.S. Cleaver, M. Ghadiri, R. Jones and Pollock, H.M., *Langmuir* **18** 5741 (2002).
- [66] R. Jones, H.M. Pollock, D. Geldart and A. Verlinden, *Powder Tech.* **132** 196 (2003).

- [67] J.A. Greenwood and J.B.P. Williamson, Proc. R. Soc. Lond. A **295** 300 (1996).
- [68] G.G. Adams and M. Nosonovsky, Tribology International **33** 431 (2000).
- [69] I.G. Goryacheva, *Mechanics of Friction Interaction (in Russian)* (Nauka, Moscow, 2001).
- [70] H. Rumpf, *Particle Technology* (Chapman & Hall, London, 1990).
- [71] T.S. Chow, Phys. Rev. Lett. **86** 4592 (2001).
- [72] K. Cooper, N. Ohler, A. Gupta and S. Beaudoin, J. Colloid Interface Sci. **222** 63 (2000).
- [73] Y.A. Rabinovich, J.J. Adler, A. Ata, R.J. Singh and B.M. Moudgil, J. Colloid Interface Sci. **232** 10 (2000).
- [74] Y.A. Rabinovich, J.J. Adler, A. Ata, R.J. Singh and B.M. Moudgil, J. Colloid Interface Sci. **232** 17 (2000).
- [75] G. Binnig, C.F. Quate and C. Gerber, Phys. Rev. Lett. **56** 930 (1986).
- [76] M. Kappl and H.J. Butt, Part. Part. Syst. Charact. **19** 129 (2002).
- [77] B.N.J. Persson, *Sliding Friction* (Springer-Verlag, Berlin, 1998).
- [78] M.A.S. Quintanilla, A. Castellanos and Valverde, J.M., Proc. Appl. Math. Mech. **3** 206 (2003).
- [79] C. Thornton, J. Appl. Mech. **64** 383 (1997).
- [80] N. Maeda, N. Chen, M. Tirrell and Israelachvili, J.N., Science **279** 379 (2002).
- [81] C.A. Coulomb, Académie Royale des Sciences, Paris **7** 343 (1776).
- [82] R. Nedderman, *Statics and Kinematics of Granular Materials* (Cambridge University Press, Cambridge, 1992).
- [83] A.W. Jenike, *Storage and Flow of Solids, Bulletin 123* (Salt Lake City, Engineering Experiment Station, University of Utah, 1964).
- [84] D. Schulze and A. Wittmaier, Chem. Eng. Tech. **26** 133 (2003).
- [85] J. Schwedes, Powder Tech. **11** 59 (1975).
- [86] D. Barletta, G. Donsi, G. Ferrari and M. Poletto, in *Powders and Grains 2005*, edited by R. García-Rojo, H.J. Herrmann and S. McNamara (Balkema publishers, Leiden, Netherland, 2005), p. 1033.
- [87] J. Schwedes, Granular Matter **5** 1 (2003).
- [88] A. Santomaso, P. Lazzaro and P. Canu, Chem. Eng. Technol. **58** 2857 (2003).
- [89] *Book of ASTM Standards, Part 9* (American Society for Testing and Materials, Philadelphia, USA, 1978).
- [90] D.A. Hall and J.G. Cutress, J. Inst. Fuel **33** 63 (1960).
- [91] *Cole-Parmer Catalog, 1997-1998*, p. 541.
- [92] C.M. Iles, I.D. Bateson and J.A. Walker, Rheometer for testing flow characteristics of materials such as powders, liquids and semisolids such as pastes, gels and ointments, Patent no. EP1102053-A2, 23 May, 2001.
- [93] R.L. Carr, Chem. Eng. **18** 163 (1965).
- [94] J.M. Valverde, A. Ramos, A. Castellanos and P.K. Watson, Powder Tech. **97** 237 (1998).
- [95] P.K. Watson, J.M. Valverde and A. Castellanos, Powder Tech. **115** 45 (2001).
- [96] J.M. Valverde, A. Castellanos and P.K. Watson, Powder Tech. **118** 236 (2001).
- [97] F. Da Cruz, F. Chevoir, D. Bonn and P. Coussot, Phys. Rev. E **66** 051305 (2002).
- [98] J. Tomas, Chem. Eng. Tech. **27** 1 (1994).
- [99] R.L. Carr, *Gas-Solids Handling in Process Industries* (Marcel Dekker, New York, 1976), Chapter 2.
- [100] *British Standard 1377: Methods of Tests for Soils for Civil Engineering Purposes* (1975).
- [101] X. Jia, C. Caroli and B. Velicky, Phys. Rev. Lett. **82** 1863 (1999).
- [102] H.H. Hausner, Int. J. Powder Metall. **3** 7 (1967).
- [103] *Classification and Symbolization of Bulk Materials* (1997).
- [104] J.M. Valverde, A. Castellanos, A. Ramos, M.A. Morgan and P.K. Watson, Phys. Rev. E **62** 6851 (2000).
- [105] M.A.S. Quintanilla, J.M. Valverde, A. Castellanos and R.E. Viturro, Phys. Rev. Lett. **87** 194301 (2001).
- [106] B.H. Kaye, Part. Part. Syst. Charact. **14** 53 (1997).
- [107] T.A. Poole, *Apparatus for determining powder flowability* Patent no. WO9738297-A1, 17 October, 1997.

- [108] A. Castellanos, A. Ramos and J.M. Valverde, Device and method for measuring cohesion in fine granular media. Patent no. WO9927345-A, 3 June, 1999.
- [109] J.M. Valverde, A. Castellanos, A. Ramos, M.A. Morgan and P.K. Watson, *Rev. Sci. Instrum.* **71** 2791 (2000).
- [110] J.M. Valverde, A. Castellanos and M.A.S. Quintanilla, *Contemp. Phys.* **44** 389 (2003).
- [111] P.C. Carman, *Trans. Inst. Chem. Eng.* **15** 150 (1937).
- [112] S.C. Tsinontides and R. Jackson, *J. Fluid Mech.* **255** 237 (1993).
- [113] J.F. Richardson and W.N. Zaki, *Trans. Inst. Chem. Engrs* **32** 35 (1954).
- [114] S. Sundaresan, *Ann. Rev. Fluid Mech.* **35** 63 (2003).
- [115] A. Castellanos, J.M. Valverde and P.K. Watson, *Z. Angew. Math. Mech.* **80** S423 (2000).
- [116] M.A.S. Quintanilla, A. Castellanos and J.M. Valverde, *Phys. Rev. E* **64** 031301 (2001).
- [117] A. Castellanos, J.M. Valverde and M.A.S. Quintanilla, *Phys. Rev. E* **64** 041304 (2001).
- [118] J.M. Valverde, M.A.S. Quintanilla, A. Castellanos and Mills P., *Phys. Rev. E* **67** 016303 (2003).
- [119] J.M. Valverde, A. Castellanos, M.A.S. Quintanilla and Mills P., 2003, *Phys. Rev. E* **67** 051305 (2003).
- [120] R. Jackson, *Trans. Inst. Chem. Engrs* **41** 13 (1963).
- [121] T.B. Anderson and R. Jackson, *Ind. Eng. Chem. Fundam.* **7** 12 (1968).
- [122] R. Jackson, *The Dynamics of Fluidized Particles* (Cambridge University Press, Cambridge, 2000).
- [123] G.K. Batchelor, *J. Fluid Mech.* **193** 75 (1988).
- [124] K. Rietema and S.M.P. Mutsers, in *Proc. Int. Symp. Fluidization and its Applications* (Toulouse, France, 1973).
- [125] G.D. Cody, D.J. Goldfarb, G.V. Storch and A.N. Norris, *Powder Tech.* **87** 211 (1996).
- [126] N. Menon and D.J. Durian, *Phys. Rev. Lett.* **79** 3407 (1997).
- [127] J.M. Valverde, A. Castellanos and M.A.S. Quintanilla, *Phys. Rev. E* **64** 021302 (2001).
- [128] E.R. Nowak, J.B. Knight, E. Ben-Naim, H.M. Jaeger and S.R. Nagel, *Phys. Rev. E* **57** 1971 (1998).
- [129] C. Josserand, A.V. Tkachenko, D.M. Mueth and H.M. Jaeger, *Phys. Rev. Lett.* **85** 3632 (2000).
- [130] J.M. Valverde, A. Castellanos and M.A.S. Quintanilla, *Phys. Rev. Lett.* **86** 3020 (2001).
- [131] P. Duru, and E. Guazelli, *J. Fluid Mech.* **470** 359 (2002).
- [132] J. Garside and M.R. Al-Dibouni, *Ind. Eng. Chem. Process Des. Develop.* **16** 206 (1997).
- [133] R. Buscall, J.W. Goodwin, R.H. Ottewill and Th.F. Tadros, *J. Colloid Interface Sci.* **85** 78 (1982).
- [134] P.N. Rowe, *Chem. Eng. Sci.* **42** 2795 (1987).
- [135] G.K. Batchelor, *J. Fluid Mech.* **52** 245 (1972).
- [136] P. Snabre, and P. Mills, *Eur. Phys. J. E* **1** 105 (2000).
- [137] J.M. Valverde, M.A.S. Quintanilla, A. Castellanos and P. Mills, *Europhys. Lett.* **54** 329 (2001).
- [138] T.A. Witten and L.M. Sander, *Phys. Rev. Lett.* **47** 1400 (1981).
- [139] Z.Y. Chen, P. Meakin and J.M. Deutch, *Phys. Rev. Lett.* **59** 2121 (1987).
- [140] Y. Kantor and T.A. Witten, *J. Physique Letters* **45** L675 (1984).
- [141] S. Manley, L. Cipelletti, V. Trappe, A.E. Bailey, R.J. Christianson, U. Gasser, V. Prasad, P.N. Segre, M.P. Doherty, S. Sankaran, A.L. Jankovsky, B. Shiley, J. Bowen, J. Eggers, C. Kurta, T. Lorik and D.A. Weitz, *Phys. Rev. Lett.* **93** 108302 (2004).
- [142] Y. Kantor and I. Webman, *Phys. Rev. Lett.* **52** 1891 (1984).
- [143] M.K. Wu and S.K. Friedlander, *J. Colloid Interface Sci.* **159** 246 (1993).
- [144] C.M. Sorensen and G.C. Roberts, *J. Colloid Interface Sci.* **186** 447 (1997).
- [145] S. Hoge Kamp and M. Pohl, *Powder Tech.* **130** 385 (2003).
- [146] S. Hoge Kamp and M. Pohl, private communication (2004).
- [147] J.M. Valverde, M.A.S. Quintanilla and A. Castellanos, *Phys. Rev. Lett.* **92** 258303 (2004).
- [148] V. Prasad, V. Trappe, A.D. Dinsmore, P.N. Segre, Cipelletti L. and D.A. Weitz, *Faraday Disc.* **123** 1 (2003).
- [149] C.S. O'Hern, S.A. Langer, A.J. Liu and S.R. Nagel, *Phys. Rev. Lett.* **88** 075507 (2002).

- [150] C.S. O'Hern, L.E. Silbert, A.I.J. Liu and S.R. Nagel, *Phys. Rev. E* **68** 011306 (2003).
- [151] R.Y. Yang, R.P. Zou and A.B. Yu, *Phys. Rev. E* **62** 3900 (2000).
- [152] K. Gotoh, and J.L. Finney, *Nature* **252** 202 (1974).
- [153] P.N. Pusey and W. van Meegen, *Phys. Rev. Lett.* **59** 2083 (1987).
- [154] C.M. Kong and J.J. Lannuti, *J. Am. Ceram. Soc.* **83** 2183 (2000).
- [155] A. Castellanos, J.M. Valverde and M.A.S. Quintanilla, *Phys. Rev. Lett.* **94** 075501 (2005).
- [156] E.E. Walker, *Trans. Faraday Soc.* **74** 119 (1923).
- [157] D.M. Wood, *Soil Behaviour and Critical State Soil Mechanics* (Cambridge University Press, Cambridge, 1993).
- [158] J.H. Atkinson, *Introduction to the Mechanics of Soils and Foundations* (McGraw-Hill, New York, 1993).
- [159] J.H. Atkinson and P.L. Bransby, *The Mechanics of Soils* (McGraw-Hill, London, 1997).
- [160] A.J. Sederman, P. Alexander and L.F. Gladden, *Powder Tech.* **117** 255 (2001).
- [161] T. Boutreaux and de P.G. Gennes, *Physica A* **244** 59 (1997).
- [162] P. Richard, P. Philippe, F. Barbe, S. Bourles, X. Thibault and D. Bideau, *Phys. Rev. Lett.* **68** 020301(R) (2003).
- [163] P. Evesque, *Poudres & Grains* **10** 6 (1999).
- [164] D. Poquillon, E. Lemaitre, J.V. Baco-Carles, Ph. Tailhades and J. Lacaze, *Powder Tech.* **126** 65 (2000).
- [165] J.H. Park and T. Koumoto, *J. Geotech. Geoenviron. Eng.* **130** 223 (2004).
- [166] W. Yao, G. Guangsheng, W. Fei and W. Jun, *Powder Tech.* **124** 152 (2002).
- [167] W.C. Yang, *Inst. Chem. Engrs* **36** 1 (2000).
- [168] J.M. Valverde and A. Castellanos, *AIChE J.*, <http://doi.wiley.com/10.1002/aic.10652> (2005).
- [169] H. Rumpf, *Chem. Ing. Tech.* **30** 144 (1958).
- [170] A.S. Helle, K.E. Easterling and M.F. Ashby, *Acta Metall.* **33** 2163 (1985).
- [171] M. Nakagaki, and H. Sunada, *Yakugaku Zasshi* **88** 651 (1968).
- [172] M. Suzuki, K. Makino, M. Yamada and K. Inoya, *Internat. Chem. Eng.* **3** 482 (1981).
- [173] E. Jaraiz, S. Kimura and O. Levenspiel, *Powder Tech.* **72** 23 (1992).
- [174] P.K. Watson, H. Mizes, A. Castellanos and A.T. Perez, in *Powders and Grains 97, Rotterdam*, edited by R. Behringer and J.T. Jenkins (Balkema, Rotterdam, 1997), p. 109.
- [175] F. Emeriault and C.S. Chang, *Comput. Geotechnics* **20** 223 (1997).
- [176] F. Radjai, D.E. Wolf, M. Jean and J.J. Moreau, *Phys. Rev. Lett.* **80** 61 (1998).
- [177] O. Tsoungui, D. Vallet, J.-C. Charmet and S. Roux, *Phys. Rev. E* **57** 4458 (1998).
- [178] J.M. Erikson, N.W. Mueggenburg, H.M. Jaeger and S.R. Nagel, *Phys. Rev. E* **66** 040301(R)-1 (2002).
- [179] A. Castellanos, J.M. Valverde, Pérez, A.T., A. Ramos and P.K. Watson, *Phys. Rev. Lett.* **82** 1156 (1999).
- [180] R.A. Bagnold, *Proc. R. Soc. London A* **295** 219 (1966).
- [181] S.B. Savage and K. Hutter, *J. Fluid Mech.* **199** 177 (1989).